SYNTHESIS AND FUNCTIONAL BEHAVIOR OF NANOCARBON AND HYBRIDS

YANG ZHENGCHUN

(B.Sci., Tianjin University)

A THESIS SUBMITTED

FOR THE DEGREE OF DOCTOR OF PHILOSOPHY

DEPARTMENT OF MATERIALS SCIENCE AND ENGINEERING

NATIONAL UNIVERSITY OF SINGAPORE

2013

DECLARATION

I hereby declare that this thesis is my original work and it has been written by me in its entirety.

I have duly acknowledged all the sources of information which have been used in the thesis.

This thesis has also not been submitted for any degree in any university previously.

Yang Zhengchun

Yang Zhengchun

15 August 2013

Table of Contents

Summary

A systematic study is made into design and synthesis of spherical carbon structures with controlled porosity and surface area, and/or fluorescence behavior in the nano to micrometer range by hydrothermal process, followed by carbonization at high temperature. On the basis of spherical nanocarbon structures, carbon nanohybrids containing manganese dioxide (MnO_2) and cobalt monoxide (CoO) nanoparticles are developed for supercapacitor applications.

Derived from different types of carbon precursors and additives, five types of spherical nanocarbon structures and nanohybrids have been developed and investigated in this thesis. Firstly, fluorescent carbon dots (C-dots) was successfully synthesized by hydrothermal treatment of glucose in the presence of monopotassium phosphate (K_2HPO_4). The size of the C-dots thus obtained could be tuned by changing the concentration of K_2HPO_4 while the resultant C-dots exhibit blue (435 nm) and green (510 nm) fluorescence emission corresponding to different sizes. The C-dots were demonstrated for bioimaging and cell labeling. Secondly, nitrogen-doped carbon nanoparticles were synthesized by using glucosamine hydrochloride (glucosamine-HCl) as the carbon precursor, which gave rise to excellent hydrophilic behavior due to the presence of aromatic amine, hydroxyl and carboxyl functional groups. At the excitation wavelength of 430 to 470 nm, the nitrogen-doped carbon nanoparticles were demonstrated to emit green fluorescence (510 nm) with excitation wavelength-independent behavior. Thirdly, monodispersed hollow nanocarbon spheres with inner macropore and external meso-/micropores in carbon wall have been successfully synthesized by hydrothermal treatment of α-cyclodextrin (α-CD) in the presence of poly (ethylene oxide)$_{106}$-poly (propylene oxide)$_{70}$-poly (ethylene oxide)$_{106}$ (F127) as the soft template. They showed excellent hydrophilic behavior, and their sizes and wall thickness were tunable by varying the concentration of F127 in aqueous solution. Upon removal of F127 by pyrolysis treatment at high temperature, the hollow nanocarbon structure retained the wanted spherical morphology. They were demonstrated for promising capacitance when used in lithium ion battery. Nanohybrids of hollow nanocarbon spheres-nanocrystalline MnO_2 were developed by the redox reaction between permanganate (MnO_4^-) and carbon. MnO_2 double layers, i.e., on both the external and internal surfaces of the hollow nanocarbon spheres could be obtained by controlling the diffusion time (16 h) of MnO_4^- through the porous carbon wall. The MnO_2 double layers showed improvement in specific capacitance when employed as the electrode in supercapacitor. Finally, a novel design of spherical nanocarbon structure, which was denoted as CoO-doped graphitic porous carbon microspheres (Co-GPCMs), was established by hydrothermal treatment of α-CD together with cobalt gluconate (Co-gluconate) in the presence of F127, followed by pyrolysis treatment in argon (Ar). The Co-GPCMs thus derived showed an interesting porous nanocarbon structure consisting of graphitic carbon, nano and micro-pores and CoO nanodots. As such, they demonstrated an overall high operation voltage (1.6 V), high energy density and improved performance when employed as electrode in supercapacitor.

List of Figures

1 Introduction

1.1 Background

Carbon, which is a widely existing and abundant element in the planet earth, has been retaining great interest as materials for various applications over a long period of time [1]. Indeed, for the past several decades, carbon and carbon-based materials are among the most extensively research topics, due to their unique structures, excellent physical, chemical and mechanical properties, such as high electrical conductivity, thermal conductivity and tunable surface functionalities [2-8]. Due to the different hybrid orbital of carbon atoms, including for example sp, sp^2 and sp^3, there are various intriguing structures that can be derived from carbon and carbon-based materials [9-25]. In general, there are four classes of carbon-based materials according to dimensionality, including zero dimension (0D) such as fullerene, nanodiamonds, carbon dots (C-dots), carbon nanoparticles and carbon spheres; one dimension (1D) such as carbon nanotubes, carbon fibers and carbon nanowires; two dimension (2D) such as graphene, graphene oxide, carbon films and carbon membranes; and three dimension (3D) such as carbon monolithic and carbon foam [9-25]. Compared with other types of carbon-based materials, 0D carbon materials of spherical morphology, C-dots, carbon nanoparticles and carbon spheres as example, are of considerable interest, owing to their uniform size ranges, controllable morphology and tunable surface functionality. They promise a wide range of applications in biomedical, energy storage, sensing, adsorption and catalyst supports [26-30]. A precise control in synthetic condition of these 0D carbon materials can lead to a significant change in the chemical and physical behavior. This chapter of review focuses on the development of synthetic strategies for fluorescent carbon nanoparticles, as well as porous spheres of nanocarbon and their nanohybrids [31, 32].

1.2 Fluorescent carbon nanoparticles

For the past two decades, considerable attention has been paid to fluorescent carbon nanoparticles, owing to their interesting optical behavior and for bioimaging applications [31, 33, 34]. The fluorescent carbon nanoparticles with sizes below 10 nm are denoted as C-dots, which are a fascinating class of fluorescent carbon materials [33, 35, 36]. Among the several different types of fluorescent carbon nanomaterials, including carbon nanotubes, nanodiamonds and carbon nanoparticles [37-41], fluorescent carbon nanoparticles are of particular interest owing to their isotropic near-spherical shapes, widely available starting materials and relatively straightforward synthetic strategies [33, 42, 43]. Typically, the fluorescence behavior of carbon nanoparticles is derived from surface passivation [44, 45]. As has been demonstrated recently, surface passivation could produce defect sites on the surface of carbon nanoparticles, which trap excitation energy. Furthermore, the trapped energy on the carbon surface gives rise to the quantum confinement of emissive energy, which leads to a strong fluorescence emission from the radiative recombination by strong excitation energy [26, 34, 46]. Surface passivation can also further introduce hydrophilic functional groups onto the nanoparticles, leading to excellent hydrophilic behavior and potential biomedical applications [47-50]. In general, there are two main types of strategy for synthesis of fluorescent carbon nanoparticles, including the top-down strategy and bottom-up strategy [33].

1.2.1 Top-down synthetic strategies

With the top-down strategy, fluorescent carbon nanoparticles are synthesized by breaking down of bulk graphitic materials into nanoparticles, followed by surface passivation [33, 51-62]. There are three main top-down synthetic techniques, including arc-discharge, laser-ablation and electrochemical synthesis [51-62]. The arc-discharge synthetic technique for producing fluorescent carbon nanoparticles is discovered by purifying single-walled carbon nanotubes derived from the arc-discharge soot [51]. When arc soot is oxidized by nitric acid (HNO_3) and extracted by sodium hydroxide (NaOH) solution, a black suspension is formed together with the purified single-wall carbon nanotubes. After separation by gel electrophoresis with three different electrophoretic bands, green-blue, yellow and orange fluorescent emissions are observed under the excitation of 366 nm ultraviolet (UV) light [51]. The fluorescent carbon species suspended in the solution is further confirmed as a type of fluorescent carbon nanoparticles with carboxyl surface functional groups and passivation [33, 51]. The arc-discharge process is highly commendable for the initial demonstration of fluorescent carbon nanoparticles. Since then, several different synthetic techniques have been further developed to produce fluorescent carbon nanoparticles, one of which is laser-ablation method [52-57]. With this method, carbon nanoparticles are derived from graphite target or powder by Nd: YAG laser (1064 nm, 10 Hz) irradiation in the aqueous environment. The carbon nanoparticles thus derived are then surface passivated in the solution of perchloric acid, HNO_3, poly (propionly-ethylenimine-*co*-ethylenimine) (PPEI-EI), poly (ethylene glycol) (PEG), diamine hydrate or diethanolamine. Alternatively, they can be surface passivated by further surface passivation step. The purified fluorescent carbon nanoparticles are obtained by dialysis of the resultant suspension against deionized (DI) water or centrifugation [52-57]. The laser-ablation process is highly significant as the process successfully produces the fluorescent carbon nanoparticles. However, the requirement of using Nd: YAG laser limits it from the large scale synthesis. The third well documented top-down process for producing fluorescent carbon nanoparticles is the electrochemical reaction, which was first demonstrated when multiwalled carbon nanotubes were used as the working electrode in a three-electrode compartment by employing the tetrabutylammonium perchlorate ($TBA^+ClO_4^-$) as the electrolyte [58-62]. Upon the application of cycling potentials on the working electrode, the electrolyte solution became yellowish to dark brownish in appearance, indicating the breaking of the multiwalled carbon nanotubes and the formation of carbon nanoparticles. The resultant yellow solution was further washed by dialyzing to remove the electrolyte salt. The carbon nanoparticles were then collected from the solution and were shown to exhibit intrinsically fluorescent behavior. This demonstrates that the fluorescent carbon nanoparticles can be produced by applying a cycling potential on the carbon working electrode in the presence of appropriate electrolyte. The fluorescent carbon nanoparticles could also be exfoliated from a column electrode of carbon with surface passivation being taken place simultaneously in the electrochemical environment [58-61]. The electrochemical process is further modified by using ionic liquid as the electrochemical reaction solution to electro-oxidize graphite to generate fluorescent carbon nanoparticles in aqueous solution [62]. There is no doubt that the top-down strategy is successful in the development of fluorescent carbon nanoparticles. It however would be of interest to explore novel synthetic routes thereby widely available carbon precursors can be used as the starting materials.

1.2.2 Bottom-up synthetic strategies

With the bottom-up strategy, fluorescent carbon nanoparticles are synthesized by surface passivation of certain molecular precursors [33, 63-70]. There are five main bottom-up synthetic process have been reported, including combustion, template supported synthesis, thermal decomposition, microwave and chemical routes [63-70]. In the combustion approach, soot, which is derived from natural gas or candle burning and collected on aluminum foil or glass plate, is unitized as the carbon precursor. Collected soot is surfaced passivated by HNO_3 refluxing and the resultant fluorescent carbon nanoparticles are collected by dialysis or centrifugation. Similarly, the carbon nanoparticles formed in the template supported synthetic route is also surfaced passivated by HNO_3 refluxing to generate the intrinsically fluorescent behavior

[63-65]. In the template supported synthetic route, however, organic carbon precursors, such as phenol/formaldedyde and 2, 4-Diaminophenol dihydrochloride, are first grown on the surface functionalized inorganic support materials, such as silicon dioxide (SiO_2) or NaY zeolites. The carbon nanoparticles/support composites are then formed by thermal oxidation under high temperature. Finally the carbon nanoparticles are obtained by etching off the inorganic support in hydrofluoric acid (HF) or NaOH solution [66, 67]. Thermal decomposition is a highly attractive one step route for producing fluorescent carbon nanoparticles, where certain low melting point molecular carbon precursors, such as ammonium citrate salt, octadecylammonium, diethylene glycolammonium citrate, 4-aminoantipyrine and sodium 11-aminoundecanoate, are thermally treated under high temperature, e. g., at 300 ^{o}C, to directly yield the surface passivated fluorescent carbon nanoparticles [68]. A further bottom-up synthetic strategy is the microwave process, in which the carbohydrates, such as glucose and fructose, are treated in the presence of PEG in an aqueous solution by microwave for a short period of time, e. g., 10 min. The microwave synthetic route is facile, when one considers the short reaction time and environmental friendliness [69]. A further simple bottom-up process is the direct treatment of carbohydrates with the concentrated sulphuric acid (H_2SO_4) or HNO_3, which is denoted as the chemical reaction for producing fluorescent carbon nanoparticles [70].

Undoubtedly the previously reported synthetic approaches, which are catalogued in either the top-down strategy or bottom-up strategy, respectively, are able to generate fluorescent carbon nanoparticles. Comparing the two strategies, on one hand, the bottom-up approach is more attractive due to the availability of numerous carbon precursors, relatively low cost and being able to be potentially adopted for large scale synthesis. On the other hand, it would be of considerable interest to further develop the bottom-up synthetic strategy, whereby some of the complicated processing steps or strict reaction conditions can be skipped.

1.3 Porous carbon spheres and hybrids

For the past two decades, various porous carbon materials have been developed, which can be classified as microporous (pore size < 2 nm), mesoporous (2 nm < pore size < 50 nm) and macroporous (pore size > 50 nm). They exhibit excellent mechanical, chemical and physical behavior, such as chemical stability, strong mechanical integrity, high electric conductivity and thermal conductivity, which are inevitably required by a number of technologically valuable applications [71-75]. Among these porous carbon materials, porous carbon spheres have been recently received considerable attentions for applications in energy storage, water treatment and biomedicine, owing to their unique structure and functional behavior, such as a very high specific surface area, low specific density, largely controllable inner pore volume and mechanical strength [76-82]. In particular, they have been considered as an essential class of candidate materials for energy storage devices, such as in supercapacitors, lithium (Li) ion batteries, fuel cells, and hydrogen storage devices [83-92]. Since their surface characteristics, dispersibility, average size and porous structure strongly affect their chemical and physical behavior, there have been several approaches developed for synthesis of these porous carbon spheres [93-95]. In general, there are two main types of strategy for porous carbon spheres, including the hard-template and soft-template approaches.

1.3.1 Hard-template synthetic strategy

The hard-template strategy has been demonstrated to produce monodispersed porous carbon spheres with controllable morphology and inner pore structure in micrometer, mesometer and macrometer ranges [71, 96]. Typically, there are four synthetic steps for the hard-template technique. The initial step is the synthesis of inorganic solid templates, common example of which include porous silica (Si), SiO_2, zinc oxide (ZnO), tin dioxide (SnO_2), aluminosilicates and zeolites of designed structures and surface functionalities [97-108]. The advantages of using these inorganic hard templates include the facile synthesis, controllable size distribution, devisable pore structure as well as the efficient surface functionality of the resultant porous carbon spheres [109]. With the hard template, certain organic carbon precursors, example of which are glucose, sucrose, furfuryl alcohol, resorcinol formaldehyde and dopamine, are assembled on the surface of the hard template by either physical adsorption or chemical impregnation [110-118]. The resultant carbon precursor/hard template hybrids are then thermally treated at a high enough temperature under an inert gas atmosphere to convert the precursor into the designed porous carbon structures [97-118]. The hard template is finally removed by chemical etching, for example by

HF or NaOH [119, 120]. Undoubtedly, the hard template approach is a successful strategy in producing porous carbon spheres with designed size and pore structures for exploring interesting chemical and physical behaviors. The procedure involved is however a typical multiple step process, as it inevitably requires the use and subsequent removal of the hard template, often by a rather aggressive process, such as chemical etching. To avoid the multiple and complicated synthetic steps of hard template method, there has been considerable efforts in developing various soft template techniques.

1.3.2 Soft-template synthetic strategy

The soft-template synthetic strategy has been recently developed as an effective approach for producing porous carbon spheres, where significant progress has been made [71, 121]. It typically involves three synthetic steps [122]. Initially, amphiphilic molecules, such as block copolymers or organic surfactants, are employed as the soft-template, which are self-assembled into the desired structures [123-130]. Typical soft-templates are the common surfactants and copolymers, such as cetyltrimethylammonium bromide (CTAB), polyoxyethylene glycol alkyl ethers (Brij), polystyrene-poly (4-vivnylpyridine) (PS-P4VP), polystyrene-poly (2-vivnylpyridine) (PS-P2VP), polystyrene-poly (ethylene oxide) (PS-PEO), poly (ethylene oxide)-poly (propylene oxide)-poly (ethylene oxide) (PEO-PPO-PEO) and poly (ethylene oxide)-poly (methyl methacrylate)-polystyrene (PEO-PMMA-PS) [123-130]. The carbon precursors required are able to interact with the soft-templates, by certain linkages, for example, as a result of the chemical driving force arising from the hydroxyl groups (-OH) [131, 132]. The typical carbon precursors are resol, phenolic resin, resorcinol-formaldehyde, phenol-formaldehyde resin, phloroglucinol-formaldehyde resin, resorcinol-furfural oligomers, carbohydrates and solubilised pitch material [133-140]. The carbon precursor/soft-template binary molecular hybrid is then converted to the wanted porous carbon spheres by pyrolysis at high temperature under an inert gas [141, 142]. The soft-template can be successfully removed by a pyrolysis treatment at high temperatures [141, 142]. To successfully develop porous carbon spheres by the soft-template strategy, there are four considerations for templates and carbon precursors [71, 143]. Firstly, there should be at least one pore-constructing constituent as the soft-template and at least one carbon-yielding chemical as the carbon precursor. The carbon precursor should be able to conjugate into the self-assembled soft-template and to cross linked with each other. The porous structure derived from the soft-template shall be able to sustain at the high reaction temperature, where the carbon precursor yields a cross linked structure and therefore the template can be removed by decomposition under the pyrolysis temperature. The fourth consideration is that the carbon precursors assembled on the soft template should be able to retain their structures during the carbonization process, where the soft templates would be eliminated [71, 121, 143].

Apart from the two main types of template synthetic strategies mentioned above, the template-free approach has also been explored for producing porous carbon spheres [144-154]. Without any template, small organic molecules, such as resorcinol, formaldehyde, styrene, are used as the carbon precursors. The carbon precursors are first formed via sol-gel chemistry synthetic routes [148-154]. The as-formed porous architecture structures are then directly pyrolyzed at high temperature to produce the porous carbon spheres. Although this one-step approach is more facile than the template strategies, the particle and pore structures of the resultant porous carbon spheres are however difficult to control under the conventional pyrolysis condition, thus restraining their applications.

Compared to other synthetic approaches, the soft-template strategy has been demonstrated to be a facile and more controllable approach for producing porous carbon spheres, as it can overcome some of the intrinsic limitations imposed by other synthetic strategies. It would thus be of considerable interest to further develop the soft-template approach for well monodispersed porous carbon spheres with controllable size and pore structure.

1.3.3 Spherical porous carbon nanohybrids

As mentioned above, investigation into porous carbon spheres is one of the extensively on-going topics for carbon-based materials. In addition to porous carbon spheres, there has been considerable interest in carbon-based nanohybrids. For applications in catalysis, energy storage and biomedicine, a fascinating class of materials is those consisting of certain inorganic nanophase on the external or inner surface of porous carbon spheres [155-161]. In general, porous carbon spheres are a common matrix for composite materials, owing to their stable structure and functional behavior, such as an highly ordered pore structure, high specific surface area, controllable pore size distribution, chemical stability, mechanical strength and generally high electric conductivity [71]. Therefore, by combining the porous carbon spheres with certain metallic and oxide materials, such as gold (Au), silver (Ag), lead (Pb), platinum (Pt), ruthenium (Ru), manganese (Mn), tin (Sn), iron (Fe), nickel (Ni), cobalt (Co), copper (Cu) and metal oxides, new physical and chemical behaviors have been developed [162-176]. There are two general approaches for synthesis of these porous hybrid materials with spherical morphology. One is to impregnate the metal salt solution into the porous structures of carbon spheres, leading to the wanted metal or metal oxide/porous carbon nanocomposites [177, 178]. The other one is to grow the metal or metal oxide on the surface of the pre-made porous carbon spheres involving certain redox reactions to yield the porous carbon/metal or metal oxide nanocomposites [179, 180]. Nevertheless, a great challenge remains for high quality porous carbon nanohybrids with truly controllable size and structures, which are required for several demanding applications.

1.4 Spherical carbon structures via hydrothermal routes

For the past few years, hydrothermal routes have been widely explored for producing several different types of inorganic materials with controlled morphologies and dimensions [181]. In general, rather different phases and structures are obtained by hydrothermal process, as compared to those obtained under normal pressure and temperature conditions [182]. Hydrothermal process has been adopted extensively in synthesis of solid-state functional materials, such as zeolites, oxides, sulphides, halides and more recently those with nanostructure [182-184]. Hydrothermal carbonization provides an alternative chemical pathway to yield different types of carbon structures and nanohybrids from precursors, such as glucose, glucosamine, sucrose, cellulose, chitosan, starch, cyclodextrin, fructose, xylose, maltoxe and amylopectin, although there remains considerable debate on the exact carbonization mechanism [185-191]. For example, monodispersed spherical carbon particles were formed from some of these precursors in DI water at mild temperatures (< 200 ^{o}C) and self-generated pressure [192, 193]. In general, hydrothermal process is an interest one step process for carbon and carbon-based materials [181, 191].

A recent understanding with the hydrothermal carbonization is the monosaccharide model, which suggests that it involves dehydration, polymerization, aromatization and carbonization [194]. Typically, it is believed that there are four important steps taking place during the hydrothermal process of monosaccharide compounds for spherical carbon structures. At the beginning, no carbon is formed during the hydrothermal treatment. However, the reaction solution turns to viscous and orange or red in appearance, due to the fragmentation and dehydration of carbohydrates to furfural-like compounds (5-hydroxymethylfurfural, furfural, 5-methylfurfural), the hydroxymethylfurfural-related 1,2,4-benzenetriol, aldehydes (acetaldehyde, acetonylacetone), organic acids (acetic, propenoic, levulinic, lactic and formic acids) and phenols [194-198]. As the reaction proceeds, the polymerization and condensation take place, giving rise to the formation of polyfurans by intermolecular dehydration and aldol condensation [186]. The aromatization of the soluble polymers leads to the generation of aromatic clusters by intermolecular dehydration and decomposition. Following that, there is a short single burst of nucleation when the concentration of the aromatic clusters reaches a critical supersaturation in the aqueous solution, which is called carbonization step and gives rise to the cross-linking of the as-formed nuclei together with the chemical species by the intermolecular dehydration [199, 200]. Finally, the nuclei clusters grow and isotropically assemble together to attain the final spherical morphology with certain surface functionalities, such as hydroxyl, carbonyl and carboxylic groups [194-200].

According to the reaction process proposed for hydrothermal carbonization of carbohydrates, the carbon structure thus formed exhibits spherically shaped particle morphology, which contains the sp^2 hybridized backbone decorated with polar oxygenated functional fragments, such as ether, pyrone, hydroxyl, phenolic, carbonyl and carboxylic chemical structures, originating from the starting carbohydrates [181, 191, 194-200]. The size and structure of the resultant carbon spheres are dependent on and effectively controlled by the types and concentration of precursors and additives as well as the hydrothermal condition [181, 191]. The presence of intrinsic functional fragments render them hydrophilic and create opportunity for further surface functionalization [201]. Therefore, the hydrothermal routes yield not only the carbon spheres at comparatively mild conditions, but also offer charring process by controllable treatment for tailoring both the carbon structure and surface characteristics. Compared with other synthetic routes, it also has several other advantages, such as use of the low toxicological starting materials, the facile instrument setup and low production cost.

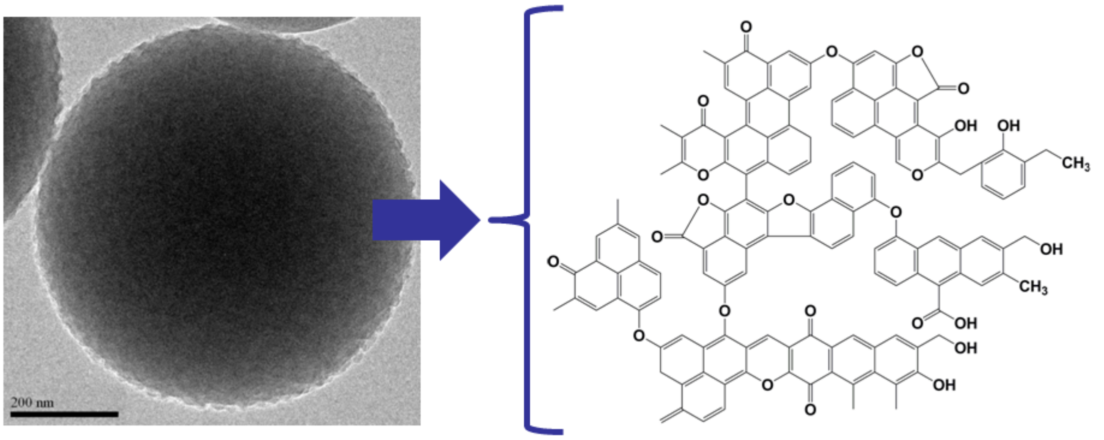

Figure 1.1 Schematic illustration of the chemical structure of the spherical carbon structures resulting from hydrothermal treatment of carbohydrates [194].

1.5 Objectives and scope

As mentioned above, hydrothermal process can lead to several different types of carbon structures with tunable chemical and physical behavior, including fluorescent carbon nanoparticles, porous carbon spheres and their nanohybrids. Alternatively, they can be synthesized by some multiple step processes, which often lack of the effective control in the carbon structures and their functional behavior. It therefore remains considerable challenging to develop these fluorescent carbon nanoparticles, porous carbon spheres and their nanohybrids by a facile and scalable process.

The main objective of this project is to establish a facile hydrothermal process for spherical carbon structures ranging from nanometers to micrometers in dimensions with the desired fluorescent behavior or level of porosity and specific surface area by controlling the carbon precursors, additives and hydrothermal conditions. The specific objectives of the present project are divided in two aspects. Firstly, a one-step hydrothermal synthetic approach is developed to produce C-dots and nitrogen-doped carbon nanoparticles with intrinsic fluorescence behavior, where their optical and potential bioimaging behavior is shown. An approach is then established to synthesize monodispersed porous carbon spheres with controllable pore framework via hydrothermal route, where the porous spheres are studied for energy storage and as the hybrid templates for development of carbon-transitional metal oxide nanohybrids.

The carbon precursors used in this project are carbohydrates, which include glucose, glucosamine and α-cyclodextrin (α-CD), by considering their wide availability and environmentally friendliness.

In accordance with the above objectives and scope, the outline of this thesis is as follows.

Chapter 2 presents a study on the intrinsically fluorescent C-dots with tunable emission derived from hydrothermal treatment of glucose in the presence of monopotassium phosphate (KH_2PO_4). The fluorescence emission of the C-dots thus produced is tunable by adjusting the concentration of KH_2PO_4. The as-synthesized C-dots are shown to exhibit a low cytotoxicity and excellent photostability. The structure and the resultant functional behavior of these C-dots are discussed.

Chapter 3 presents an investigation into a one-step hydrothermal synthetic strategy for producing nitrogen-doped carbon nanoparticles from glucosamine hydrochloride (glucosamine-HCl). The carbon nanoparticles thus produced demonstrate excitation wavelength-independent photoluminescence behavior, when the excitation wavelength is changed from 430 to 470 nm. On the basis of their structures, a formation mechanism is proposed for these nitrogen-doped carbon nanoparticles.

Chapter 4 details a one-step synthesis of hollow carbon spheres with inner macropore and meso-/microporous external carbon wall. The approach is based on the strategy of forming supermolecular structure between α-CD and poly (ethylene oxide) (PEO). Hollow carbon spheres with controllable size and morphology are made by hydrothermal treatment of α-CD in the presence of PEO_{106}-PPO_{70}-PEO_{106} (F127) as the soft template. The hollow carbon spheres thus derived are demonstrated to exhibit excellent hydrophilic behavior. Their sizes and wall thicknesses are shown tunable by adjusting the ratio of α-CD to F127. Upon pyrolysis at 900 ^{o}C in argon (Ar), the hollow carbon spheres exhibit a meso-/microporous carbon wall, which are demonstrated to be a promising candidate for anode in Li ion battery.

Chapter 5 presents an investigation into hollow carbon nanohybrid spheres with manganese dioxide (MnO_2). Given the micro- and meso-pores in the carbon wall of hollow carbon spheres, incorporation of permanganate (MnO_4^-) gives rise to the formation of nanocrystalline MnO_2 on the carbon surface, where the redox reaction between carbon and MnO_4^- takes place. An appropriate control in the diffusion of MnO_4^- into the hollow core, nanocrystalline MnO_2 can be successfully grown on both the external and internal surfaces of the hollow carbon structure. The carbon-MnO_2 nanohybrid spheres are demonstrated as a promising candidate material for supercapacitors.

Chapter 6 describes a novel design and facile synthetic process for a new carbon-based nanohybrid, denoted as cobalt monoxide (CoO)-doped graphitic porous carbon microspheres (Co-GPCMs). With the hydrothermal strategy and following pyrolysis process, where cobalt gluconate (Co-gluconate), α-CD and F127 are used as the starting materials, the resultant Co-GPCMs exhibits a porous carbon matrix with CoO nanodots being embedded in the localized graphitic structure. The Co-GPCMs effectively combines the electric double-layer capacitance and pseudo-capacitance when used as the electrode in supercapacitors, which lead to a high operation voltage (1.6 V) and give rise to a high energy density.

Chapter 7 is a conclusion of this project, together with some suggestions for future work.

Chapter 8 is the list of references quoted in this thesis.

2 Intrinsically fluorescent carbon dots (C-dots) with tunable emission behavior

2.1 Background

For the past two decades, considerable attention has been paid to fluorescent nanocrystals for biomedical applications due to their high quantum yield, tunable fluorescence spectrum and photostability [202-205]. However, use of heavy metal fluorescent nanocrystals, such as cadmium selenide (CdSe), cadmium telluride (CdTe) and lead telluride (PbTe), is hampered by their long term toxicity and environmental hazardness [205]. Recently, carbon nanomaterials are shown to be as a class of potentially valuable fluorescent materials due to their low toxicity and environmental friendliness [33]. Indeed, fluorescent carbon dots (C-dots), with diameter less than 10 nm, are considerably attractive for bioimaging and biosensor applications, because of their small sizes, near isotropic shape and abundant hydrophilic functional groups on their surface [33]. As mentioned in chapter 1, there are numerous synthetic methods of producing fluorescent C-dots, either top-down or bottom-up strategies. However, for potential biomedical applications, little progress is made due to the lack of high quality C-dots and available large scale synthetic methods [41]. Although previously reported techniques could produce C-dots with high quantum yield, they required rather sophisticated synthetic steps, especially with surface functionalization [206]. Some other synthetic routes could give rise to multicolor emission fluorescent C-dots, they however involve additional size separation processes, which not only make them complex, but also decrease production yield [45, 207]. Therefore, it would be of considerable interest to develop a facile processing approach for fluorescent C-dots, whereby some of the complicated processing steps or reaction conditions are skipped. In this chapter, a facile and effective synthetic approach is described for producing fluorescent C-dots by hydrothermal treatment of glucose in the presence of monopotassium phosphate (KH_2PO_4). With this new approach, the formation and the surface passivation of C-dots are carried out simultaneously, resulting in intrinsic fluorescence emission. Furthermore, the C-dots exhibit variable fluorescence emissions, which can be developed by simply adjusting the concentration of KH_2PO_4. The first discovery of the C-dots within this project is hydrothermal treatment of glucose solution in the presence of phosphate buffer solution, which contains NaCl, KCl, Na_2HPO_4 and KH_2PO_4. Although C-dots can be synthesized by hydrothermal treatment of glucose in the presence of each salt, KH_2PO_4 gives rise to a better size controlling of the as-synthesized C-dots. Therefore, KH_2PO_4 is used in this project.

2.2 Experimental details

2.2.1 Materials

Glucose (99.5%) is purchased from Sigma-Aldrich Company. KH_2PO_4 (99.5%) and Ethanol (99.9%) are purchased from Merck Company.

2.2.2 Synthetic procedure of C-dots

In a typical example of synthetic procedure, 40 mg of glucose and 1090 mg of KH_2PO_4 with the molar ratio of glucose/KH_2PO_4 of 1/36 were dissolved in 40 mL deionized (DI) water. The solution was then placed in a Teflon-lined autoclave chamber and nitrogen (N_2) gas was blown into it for 1 h to remove oxygen (O_2) dissolved in the solution. After that, the chamber was sealed and put into an oven. Upon completion of the hydrothermal reaction in an oven at 200 ^oC for 12 h, the reaction product was centrifuged at 9,000 rpm for 15 min to remove the black precipitates. The yellow supernatant was collected and freeze dried. The powder thus obtained was re-dispersed in ethanol to yield yellow suspension through vortexing, and the dispersion was allowed to stand for 2 h to allow the free salt to precipitate from ethanol. The yellow ethanol solution was then filtered through a poly (1, 1, 2, 2-tetrafluoroethylene) (PTFE) syringe filter with pore size of 1.0 μm and ethanol was gently evaporated off through rotary evaporating. The C-dots thus obtained were further purified by dialyzing against DI water using Spectra/Por dialysis membrane with molecular weight cut-off of 100 $gmol^{-1}$. The reason of using dialysis membrane with lower molecular weight cut-off is to avoid the loss of C-dots during dialysis. The C-dots are denoted as C-Blue. The other C-dots that were synthesized from 40 mg glucose in the presence of 773 mg of KH_2PO_4 with the molar ratio of glucose/KH_2PO_4 of 1/26 by following the same approach as that of C-Blue were purified by using dialysis membrane with molecular weight cut-off of 1,000 $gmol^{-1}$, and denoted as

C-Green. 40 mg glucose was hydrothermally treated in 40 mL DI water at 200 ^{o}C for 12 h as the control experiment.

2.2.3 Characterization

Ultraviolet-visible (UV-Vis) and photoluminescence (PL) spectra of the solution of C-dots were measured by Shimadzu UV 3101 PC and Perkin Elmer LS55 Fluorescence Spectrometer at room temperature, respectively. Quartz cells with 10 mm path length were used for all spectra testing. Life time of C-dots was measured by the 405 nm line of a picosecond pulsed laser diode head (PicoQuant PDL 800-B). For life time test, PL of the as-synthesized C-dots was first measured by using a monochromator (Acton SpectroPro 2300i) and being detected with a liquid N_2 cooled CCD camera (Princeton, Spec-10:100). The lifetime results were recorded with Time-correlated Single Photon Counting (TCSPC) Module and Picosecond Event Timer (PicoHarp 300). The particle morphology of C-dots was studied by using transmission electron microscope (TEM) at an accelerating voltage of 300 kV (TEM, CM 300 FEG-Philips). Dry C-dots powder was obtained by freeze drying. The carbon structure of the C-dots was determined by RENISHAW Raman Microscope with 514 nm laser radiation source. Their chemical structures were examined by using Fourier transform infrared (FTIR) spectroscopy (Perkin Elmer FT-IR 2000), where the FTIR sample was prepared by pressing the mixture of C-dots and potassium bromide (KBr) into a thin pellet. The surface structure of C-dots was investigated using X-ray photoelectron spectroscopy (XPS) (ESCALAB 200i-XL, Thermo Scientific). The confocal images of HepG2 cells cultured in the presence of C-Green were recorded by using Olympus Fluoview 1000 confocal laser scanning microscope.

2.2.4 Cell culture condition

HepG2 cells (American Type Culture Collection) were used for the cell study of fluorescent C-dots. The culture medium consisted of the Dulbecco's Modification of Eagle's Medium (DMEM) with glucose (4.5 gg^{-1}), sodium pyruvate and l-glutamin, 10% Fetal Bovine Serum (FBS), Penicillin (100 units) and Streptomycin (100 mgmL^{-1}). For the cell viability study, the HepG2 cells cultured in the presence of C-Green was studied by MTS (3-(4, 5-dimethylthiazol-2-yl)-5-(3-carboxymethoxyphenyl)-2-(4-sulfophenyl)-2H-tetrazolium) assay. The HepG2 cells were first grown by using 96 well plates (4,000 cells/well) and then cultured in culture media of different concentrations (0, 0.05, 0.125, 0.25, 0.5 and 0.625 mgmL^{-1}) of C-Green at 37 ^{o}C in 5% CO_2. After culturing for 72 h, MTS/phenazine methosulfate solution was used to replace the growth medium and then the HepG2 cells were incubated for another 3 hours. The Benchmark Plus microplate spectrophotometer (Bio-RAD) was used to measure the optical absorbance of each cell growth well (λ = 490 nm). The cell viability at each C-Green concentration was averaged from three repeated testing. For confocal images of HepG2 cells, the cells (15,000 cells/well) were seeded in an 8 well chamber (LAB-TEK, Chambered Coverglass System). The culture medium and the growth environment is the same as that for cell viability test. After 24 h, fresh DMEM containing 0.5 mgmL^{-1} C-Green was used to replace the culture medium.

2.3 Results and discussion

2.3.1 Structure and PL behavior of C-dots

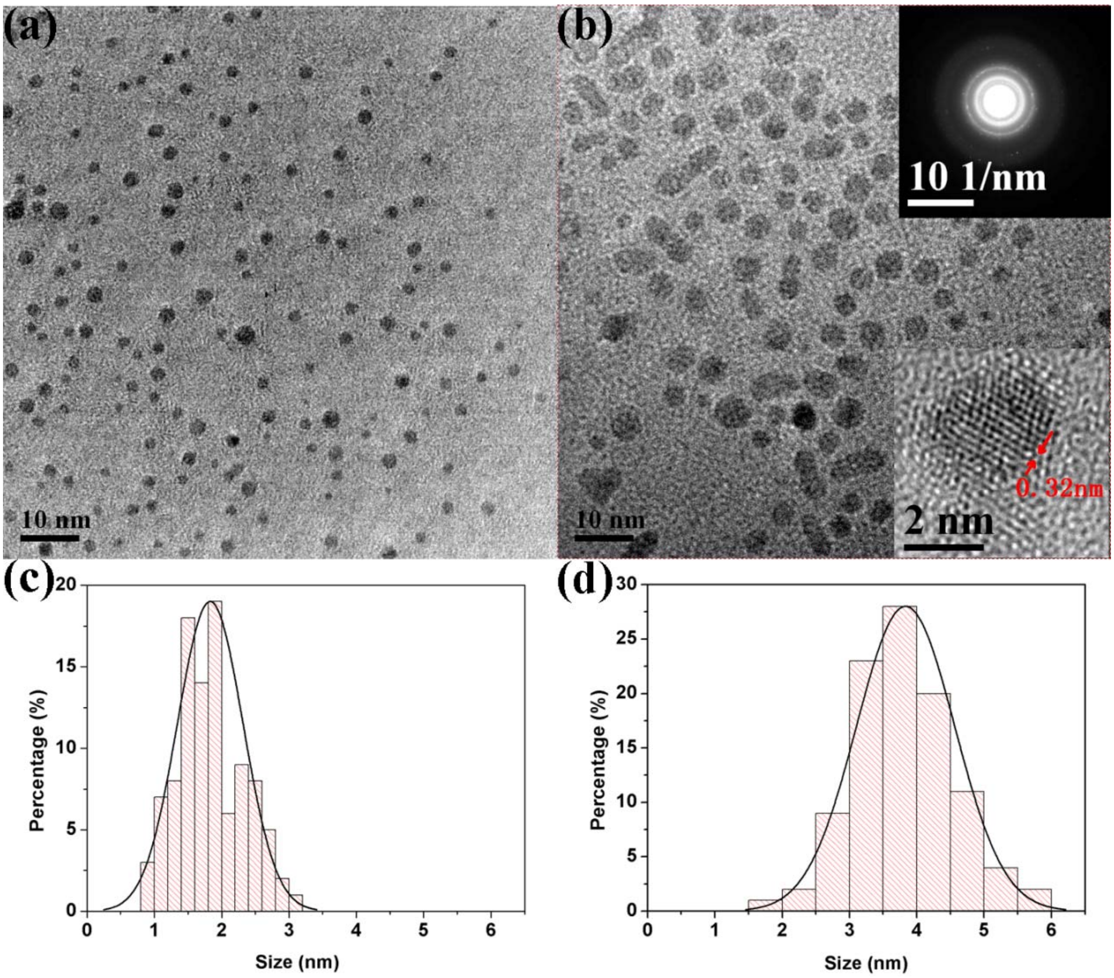

Figure 2.1 TEM images of C-Blue (a) and C-Green (b), and the size distribution of C-Blue (c) and C-Green (d) 1measured by TEM studies. Inset: the SAED pattern (upper inset) and high resolution TEM image of individual C-Green (lower inset).

The C-dots are near spherical in morphology as shown by their TEM images in Figure 2.1. Their size distribution histograms (Figure 2.1 c and d) indicate that the size of these C-dots is largely determined by the concentration of KH_2PO_4. While the average size of C-Blue synthesized at high concentration of KH_2PO_4 with the molar ratio of glucose/KH_2PO_4 of 1/36 is 1.83 nm, the average size of C-Green is 3.83 nm at low concentration of KH_2PO_4 with the molar ratio of glucose/KH_2PO_4 of 1/26. In the absence of KH_2PO_4, black suspension of carbon aggregates with average size of 15.7 nm in irregular shape was obtained following the same sample procedure (Figure 2.2 b and 2.3). In contrast, in the presence of KH_2PO_4, a yellowish suspension was obtained (Figure 2.2 a). This is because from the monosaccharide model of hydrothermal carbonization of glucose which is introduced in chapter 1, there are four typical steps taking place during the hydrothermal process of glucose for producing carbon particles, which are dehydration, polymerization, aromatization and carbonization. Especially, between the aromatization and carbonization steps, the carbon nuclei is generated when the concentration of the aromatic clusters reach a critical supersaturation in the aqueous solution. The KH_2PO_4 plays an important role within this period, when the nuclei clusters isotropically assemble together and grow to the carbon particles. In the reaction system, the KH_2PO_4 plays as the stabilizer to prevent the carbon nuclei from assembling and growing. In addition, the higher concentration of KH_2PO_4 in the solution, the bigger of the separation effect of the carbon nuclei. Therefore, the size of the as-synthesized C-dots is lower than 10 nm and the smaller size C-dots can be produced from the higher concentration of KH_2PO_4. [67, 208]. Study of using high-resolution TEM images of C-Green (lower inset in Figure 2.1 b) shows that the individual C-dots possess a crystalline structure with lattice spacing of 0.32 nm, which is in close match with the (002) lattice spacing of disordered graphite [67, 208]. The crystalline structure is further confirmed by the selected-area electron diffraction (SAED) pattern of C-Green (upper inset in Figure 2.1 b).

Figure 2.2 Digital photo of the supernatant derived from hydrothermal treatment of glucose in the presence of KH_2PO_4 (a) and in the absence of KH_2PO_4 (b).

Under irradiation of UV lamp (λ = 365 nm), there is blue emission (inset digital photo in Figure 2.4 a) for C-Blue while green emission (inset digital photo in Figure 2.4 b) for C-Green. The UV-Vis absorption spectra of C-Blue and C-Green and their PL emission spectra excited by various incident lights are shown in Figure 2.4 a and b, respectively. At the excitation wavelength of 350 nm, a strong emission peak at 435 nm is observed in the PL emission spectrum of C-Blue, indicating a blue light emission (Figure 2.4 a).

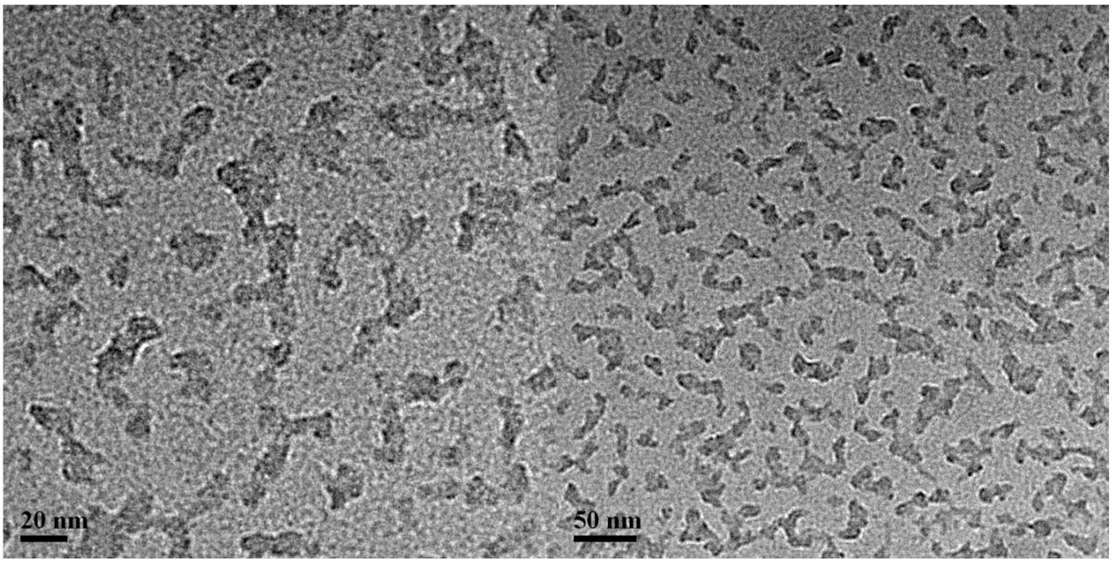

Figure 2.3 TEM images of the carbon aggregations synthesized by hydrothermal treatment of glucose (1 mgmL^{-1}) at 200 ^{o}C for 12 h in the absence of KH_2PO_4.

When the excitation wavelength is increased from 350 to 390 nm, the emission peak does not shift much with a maxima red shift of ~10 nm. The C-Green exhibits an emission peak at 510 nm at 440 nm excitation (Figure 2.4 b), with a maxima emission wavelength shift of ~20 nm when the excitation wavelength increases from 440 to 490 nm. The size-dependence of PL emission is a common behavior with non-carbon quantum dots (QDs) [209]. When the average size of C-dots increases from 1.83 nm to 3.83 nm, the fluorescence emission shifts from 435 nm to 510 nm. Therefore, the fluorescence emission of C-dots can be tuned due to the size dependent quantum effect, by simply adjusting the concentration of KH_2PO_4 as the particle size of C-dots is determined by the concentration of KH_2PO_4 as discussed above.

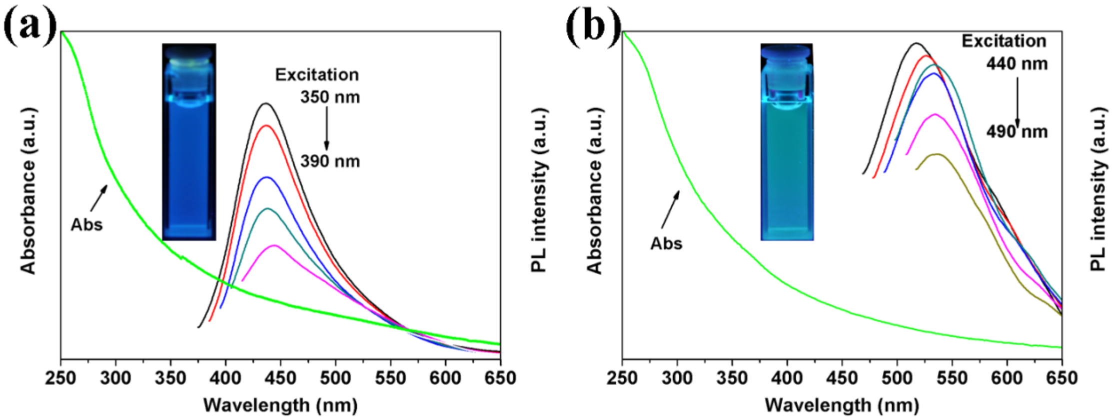

Figure 2.4 UV-Vis absorption (Abs) and PL emission spectra of C-Blue (a) and C-Green (b), respectively. The PL emission of C-Blue was recorded progressively from 350 to 390 nm excitation wavelengths at 10 nm increment while the PL emission of C-Green was recorded progressively from 440 to 490 nm excitation wavelengths at 10 nm increment. Inset: digital optical photo of C-Blue and C-Green under UV lamp excitation of 365 nm.

The quantum yield of C-Blue and C-Green is measured to be 0.024 and 0.011, under the excitation length of 350 and 440 nm, respectively. Under the laser excitation of 405 nm, the life time of C-Blue and C-Green is determined to be 2.0 and 1.8 ns, respectively (Figure 2.5), which are comparable to those of C-dots reported previously and however are prepared via different routes [33]. Both C-Blue and C-Green exhibit excellent photostability, which is demonstrated by only 12% decay on the PL emission peak intensity even after 7 h continuous excitation using a xenon (Xe) lamp (Figure 2.6). Furthermore, the PL emission of both C-Blue and C-Green is pH independent in the pH range of 3 to 12 (Figure 2.7).

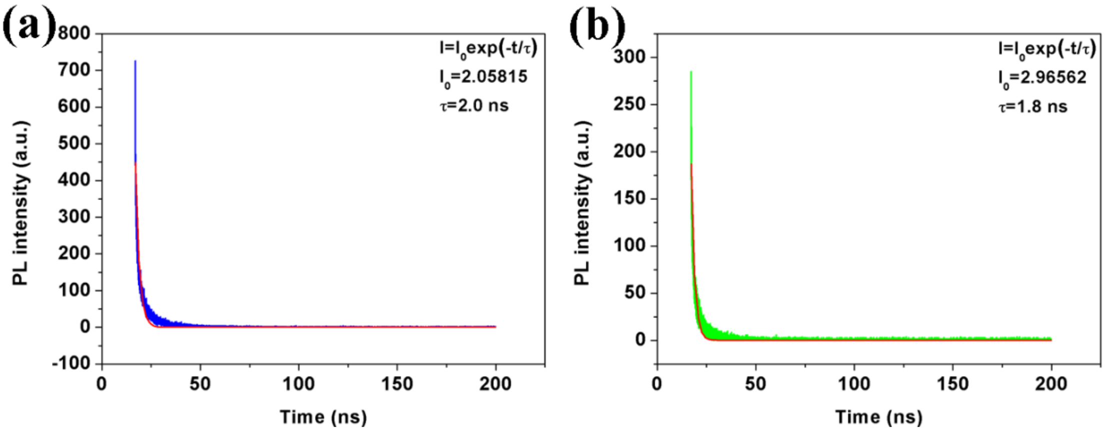

Figure 2.5 Lifetime determination of C-Blue (a) and C-Green (b).

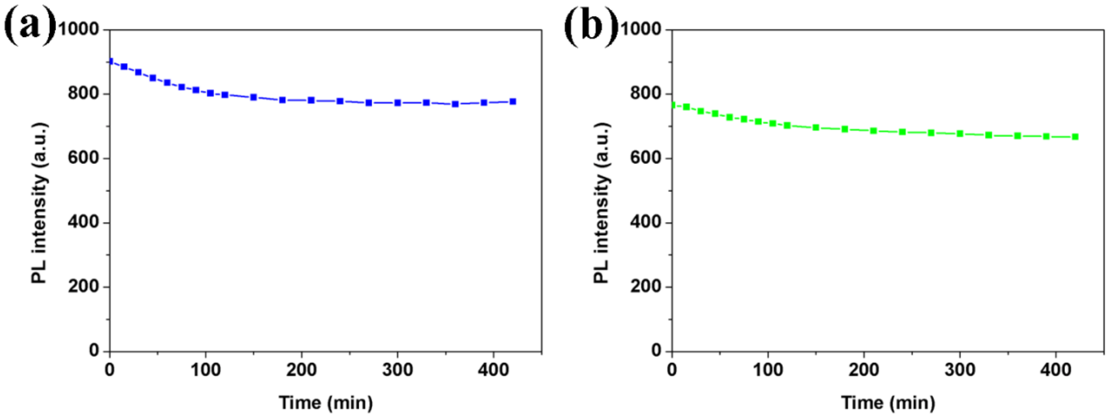

Figure 2.6 Photostability of C-Blue (a) and C-Green (b). Dependence of PL emission intensity on excitation time for C-Blue and C-Green in DI water. The suspension of C-Blue is continuously excited at 350 nm by Xe lamp while the suspension of C-Green is continuously excited at 440 nm by Xe lamp. The time for the continuous excitation is 7 h.

The carbon structures of C-Blue and C-Green were confirmed by their respective Raman spectra (Figure 2.8). The broad peak at 1363 cm^{-1} is assigned to D band, which corresponds to the *sp*^{3} defects in C-dots [11]. The peak at 1602 cm^{-1} matches well with the 1st order G band, which is a band related to the in-plane bond-stretching motion of C *sp*^{2} atoms, indicating that there are aromatic and olefinic groups inside C-dots [194].

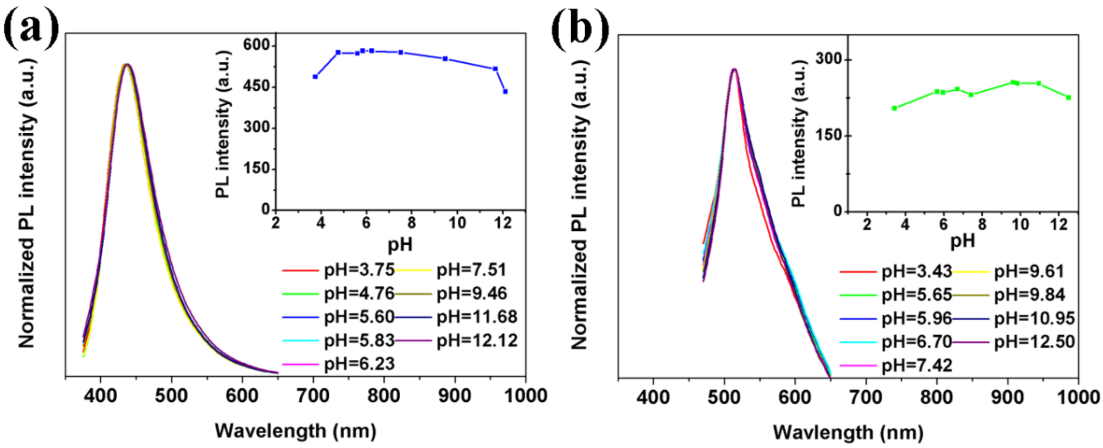

Figure 2.7 Normalized PL emission spectra of C-Blue at 350 nm excitation (a) and C-Green at 440 nm excitation (b) in aqueous solution with different pH value. Dependence of PL emission intensity on the solution pH value for C-Blue (inset in (a)) and C-Green (inset in (b)).

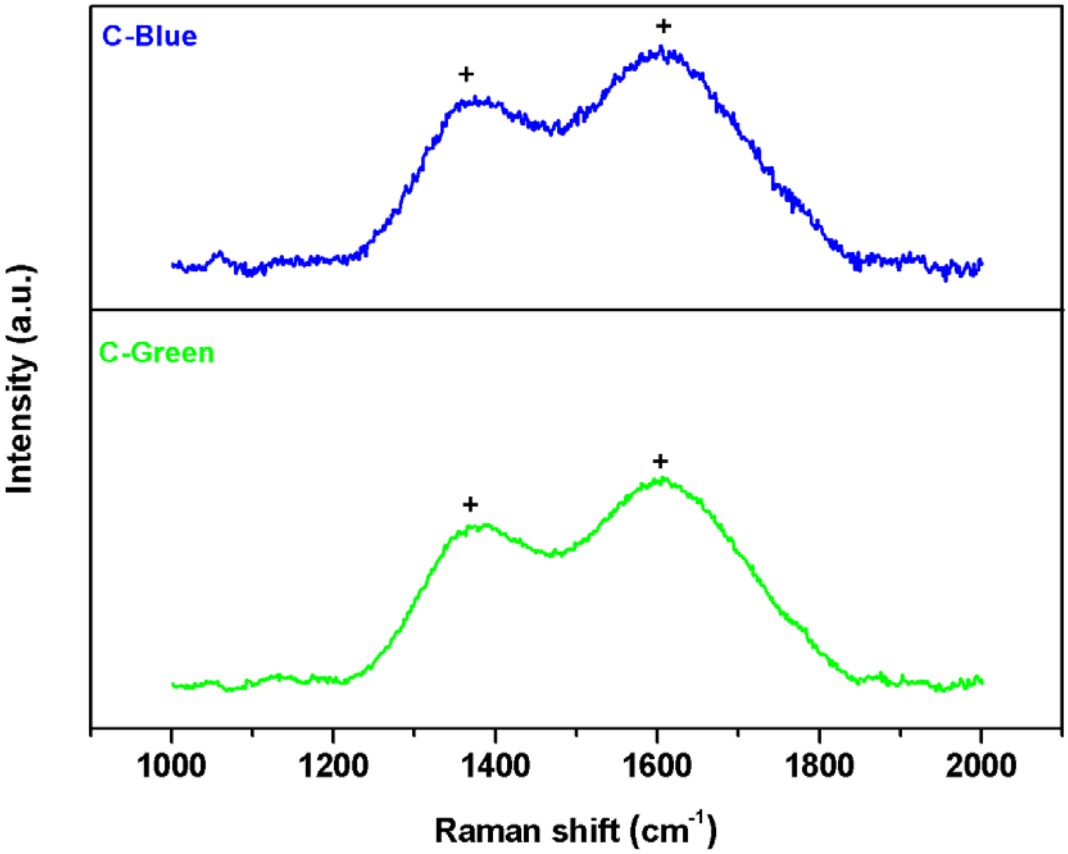

Figure 2.8 Raman Spectra of C-Blue (a) and C-Green (b).

The chemical structure of C-dots is characterized using FTIR spectroscopy. As shown in Figure 2.9, the absence of characteristic peaks (1462, 1151, 1102, 1027, 919 and

841 cm^{-1}) of glucose in the FTIR spectra of C-dots confirm the carbonization of glucose under the hydrothermal condition [210]. This is further confirmed by the observation of vibration band of C=C in both C-Blue (1639 cm^{-1}) and C-Green (1586 cm^{-1}) [194].

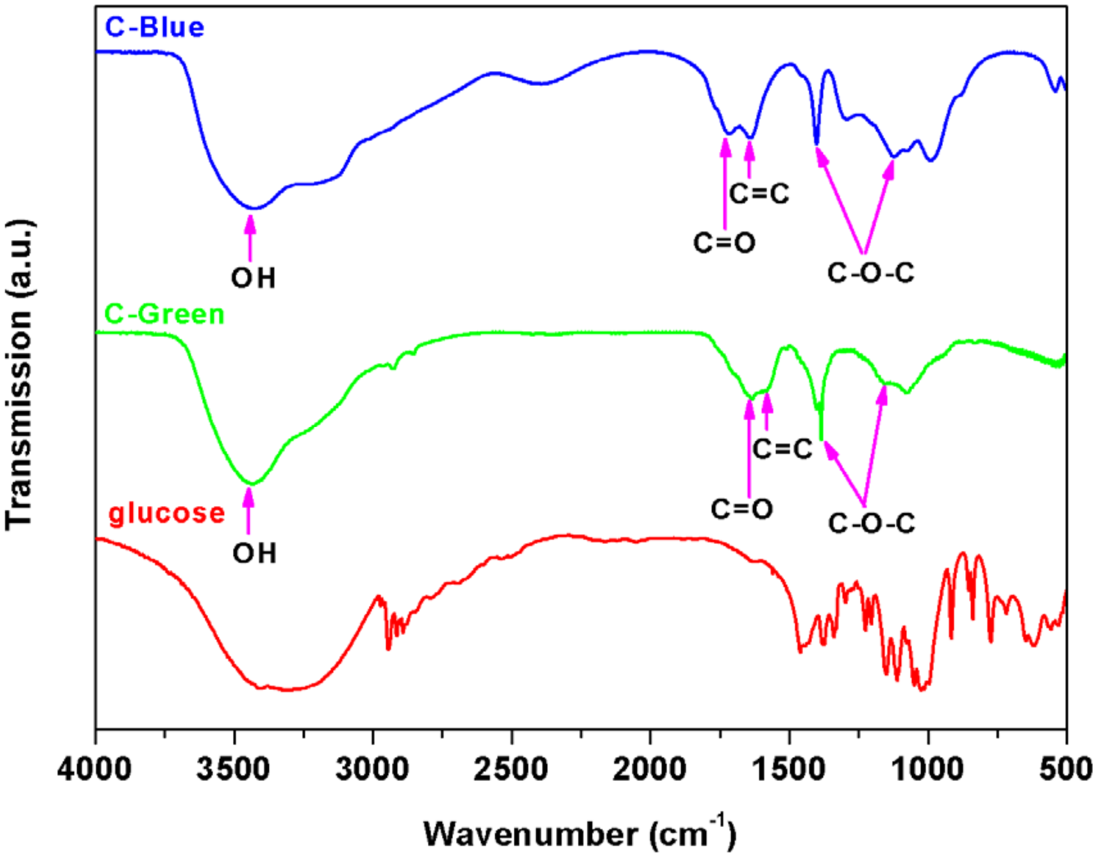

Figure 2.9 FTIR spectra of C-Blue, C-Green and glucose.

In addition, there are apparent hydrophilic functional groups on the surface of C-dots, as shown by the vibration bands of -OH (3440 cm^{-1}) and C-O-C (1350 and 1200 cm^{-1}) groups [69, 211, 212]. Moreover, besides the vibration band of C=O, the asymmetric and symmetric stretching vibration bands of C-O-C also indicate that the surface of C-dots is partially oxidized during the hydrothermal process [69, 211, 212]. The surface functionalization and partial oxidation is due to the oxidation of -OH groups in glucose under the hydrothermal condition.

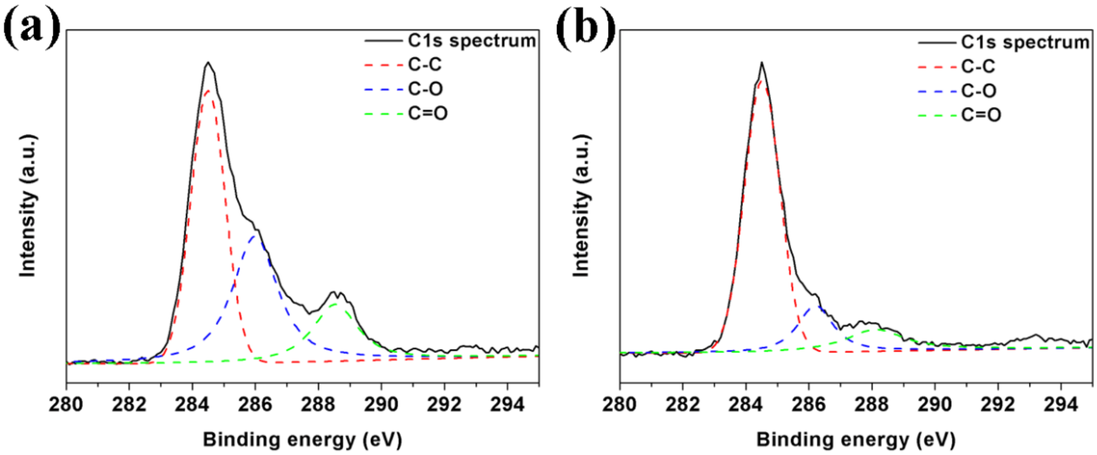

Figure 2.10 C1s XPS Spectra of C-Blue (a) and C-Green (b).

As reported previously, there exist certain aromatic moieties in the carbon matrix of C-dots derived from glucose by hydrothermal treatment, which is also confirmed by the Raman spectra in the present work [194]. The aromatic molecules lead to *sp*^{2} carbon conjugation fragments within C-dots [194]. The overall structure of the as-prepared C-dots can be proposed as an assembling of *sp*^{2} carbon conjugation fragments. The O atoms in association with the surface conjugation of C-dots, which are normally noted as surface passivation, make them fluorescence emissive by creating HOMO/LUMO energy gaps. In addition, comparing the FTIR spectra of C-Blue and C-Green (Figure 2.9), the vibration bands of C=C and C=O shift towards shorter wavenumber when the size of the C-dots increases, indicating that there is a increase in the degree of passived *sp*^{2} carbon conjugation fragments [58]. Although the exact origin of luminescence for the size dependent fluorescence C-dots is subject to further study, the phenomenon observed so far suggests that an incensement in the degree of *sp*^{2} carbon conjugation fragments gives rise to a higher energy gap. As the size of C-dots increase, the specific amount of *sp*^{2} bonding fractions on the surface of C-dots decrease, which leads a lower energy gap to generate radiative recombination of excitons. Therefore, there is a red shift in emission when the size of C-dots is increased [58].

The chemical structure of C-dots is further characterized using XPS (Figure 2.10). The appearance of a peak at the binding energy of 284.5 eV indicates the presence of graphitic *sp*^{2} carbon structure in both C-Blue and C-Green [213]. The peaks centered at the binding energies of 286.2 and 288.3 eV correspond to C-O and C=O, respectively, which agree well with the FTIR result showing that there are surface passivation and hydrophilic functional groups on the surface of the as-synthesized C-dots [213].

2.3.2 C-dots for bioimaging

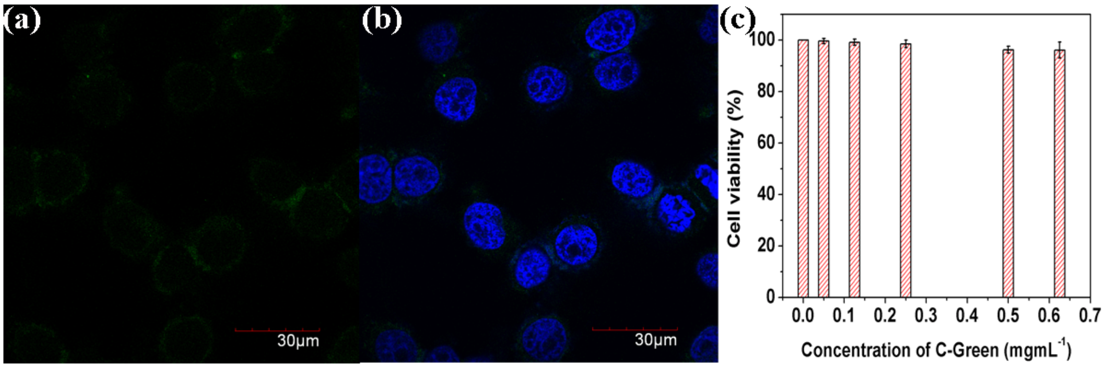

Figure 2.11 Confocal images of HepG2 cells cultured in the presence of C-Green (0.5 mgml^{-1}) for 24 h (λ = 488 nm) (a and b), where (a) is fluorescence image of C-Green and (b) is fluorescence image of C-Green and DAPI, and Cell viability of HepG2 cells cultured at different concentrations of C-Green by using MTS assay.

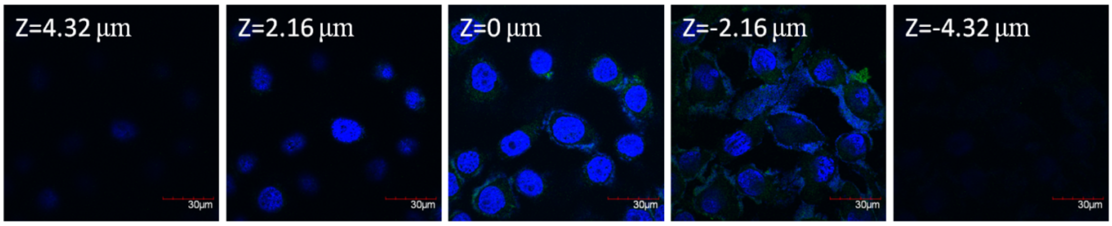

Figure 2.12 Z-axis scannings of confocal images of HepG2 cells cultured in the presence of C-Green (0.5 mgml^{-1}) for 24 h (λ = 488 nm).

The potential application of the fluorescent C-dots derived from hydrothermal process in the present work as a bioimaging agent is demonstrated by labeling HepG2 cells using C-Green. The cellular uptake of C-Green by HepG2 cells is observed using confocal laser scanning microscopy. In order to study the location of the C-dots inside the cells, the nuclei of HepG2 cells were stained by 4',6-diamidino-2-phenylindole (DAPI), which produces blue fluorescence nucleus images. As shown in Figure 2.11 a and b, green fluorescence in the cytoplasm region surrounding the nuclei of HepG2 cells is observed while the blue color in the cell is generated from DAPI, demonstrating that the C-Green was successfully internalized by HepG2 cells. The internalization of C-Green is further verified by Z-axis scanning confocal microscopy images of HepG2 cells (Figure 2.12). The appearance of both a strong green fluorescence of C-Green and blue fluorescence of DAPI at the middle height of the HepG2 cells confirms the internalization of C-Green. In addition, the cytotoxicity result (Figure 2.11 c) shows that, after 72 h, there is still no appreciable cytotoxicity for HepG2 cells cultured in the presence of up to 0.625 mgmL^{-1} of C-Green. The cell imaging and viability result therefore suggest that the as-synthesized C-dots could be used as cell imaging agent.

2.4 Summary

In conclusion, a one-step method of synthesizing intrinsic fluorescence C-dots has been demonstrated, whereby monodispersed and photostable fluorescent C-dots are produced through hydrothermal treatment of glucose in the presence of KH_2PO_4. The KH_2PO_4 plays an important role in controlling the size of the C-dots thus produced. The fluorescence emission of the C-dots thus produced is tunable by adjusting the concentration of KH_2PO_4. The cellular uptake demonstrates that the fluorescent and hydrophilic C-dots are promising candidate for fluorescent cellular imaging.

3 Nitrogen-doped carbon nanoparticles of intrinsic fluorescence behavior

3.1 Background

As mentioned in the preceding two chapters, fluorescent carbon nanoparticles have attracted tremendous interest for potential applications, such as in optoelectronic devices, biosensing and bioimaging, owing to their chemical inertness, facile functionalization, high solubility in aqueous environments, high resistance to photobleaching and good biocompatibility [33, 34, 59]. Recently, there has been considerable interest in improving the fluorescent behavior and understanding the photoluminescence (PL) mechanism. Heteroatom doped carbon nanoparticles, such as those doped by nitrogen and sulfur, have been prepared and pursued due to their excellent intrinsic behavior [67, 68, 214-217]. Particularly, nitrogen-doped carbon nanoparticles are of considerable value. One well known production technique is to create nitrogen vacancy (N-V) centers in nanodiamonds [38]. There are several chemical and physical methods to introduce this defect into nanodiamonds. Nevertheless, most of these techniques are not feasible for creating a large number of N-V centers in ultra-fine nanodiamonds [218-220]. Surface passivation of carbon nanoparticles by using nitrogen-containing reagents, such as amino-terminated polyethylene (PEG_{1500N}), polyetherimide (PEI) and ethylenediamine has also been reported [214, 217]. Nevertheless, they suffer from rather complex processing parameters required, time-consuming and high synthesis cost. Therefore, there is need to explore alternative synthetic routes for nitrogen-doped carbon nanoparticles. Glucosamine is an amino sugar and motif of chitosan, which is an efficient monomer for DNA binding and therefore offers the desired biocompatibility, environment friendliness and low cost [221, 222].

In this chapter, a one-step hydrothermal process is developed for synthesizing nitrogen-doped carbon nanoparticles with intrinsically fluorescent behavior by using glucosamine hydrochloride (glucosamine-HCl) as the starting material. During the hydrothermal process, the formation of NCNPs and their surface passivation take place simultaneously, giving rise to the intrinsically fluorescent behavior. The functional groups such as carboxyl acids and aromatic amines are also developed on the surface of these carbon nanoparticles.

3.2 Experimental details

3.2.1 Materials

Glucosamine-HCl (99.5%) is purchased from Sigma-Aldrich Company.

3.2.2 Synthetic procedure of nitrogen-doped carbon nanoparticles

The nitrogen-doped carbon nanoparticles prepared in this chapter are denoted as NCNPs. In a typical synthetic procedure, 40 mg glucosamine-HCl was dissolved in 40 mL deionized (DI) water, and then transferred into a Teflon-sealed autoclave tube.

Upon heat treatment at 140 ^{o}C for 12 h, the clear solution turned into black in appearance. The black solution was then dialyzed against DI water using Spectra/Por dialysis membrane with different molecular weight cut-off of 2,000 gmol^{-1} for two days to remove the unreacted glucosamine-HCl as well as low molecular weight by-products. Dry powder of NCNPs was obtained by freeze drying the dialyzed dispersion for two days and then vacuum drying at 60 ^{o}C.

3.2.3 Characterization

Transmission electron microscopy (TEM), Fourier transform infrared (FTIR) and X-ray photo-electron spectroscopy (XPS) measurements of NCNPs were conducted by following the same process mentioned in chapter 2. Hydrodynamic size and size distribution of the NCNPs in water were measured by using dynamic light scattering (DLS) (Malvern Zetasizer Nano-sizer with a 633 nm HeNe laser). All measurements were conducted by using DI water as the dispersant in disposable DTS 1060 C-Clear disposable zeta cell. The carbon structure of the NCNPs was studied using Witec confocal Raman Microscope with LGR 7801 M4 (488 nm) radiation source and Bruker D8 X-ray Diffraction (XRD) equipped with Cu Kα radiation (λ = 0.15418 nm). Photoluminescence (PL) and photoluminescence excitation (PLE) spectra of the NCNPs were measured using a Shimadzu RF-5301 PC at room temperature. Prior to each measurement, 1 mL of the dispersion of the dialyzed NCNPs was diluted with 3 mL DI water.

3.3 Results and discussion

3.3.1 Structure and fluorescent behavior of NCNPs

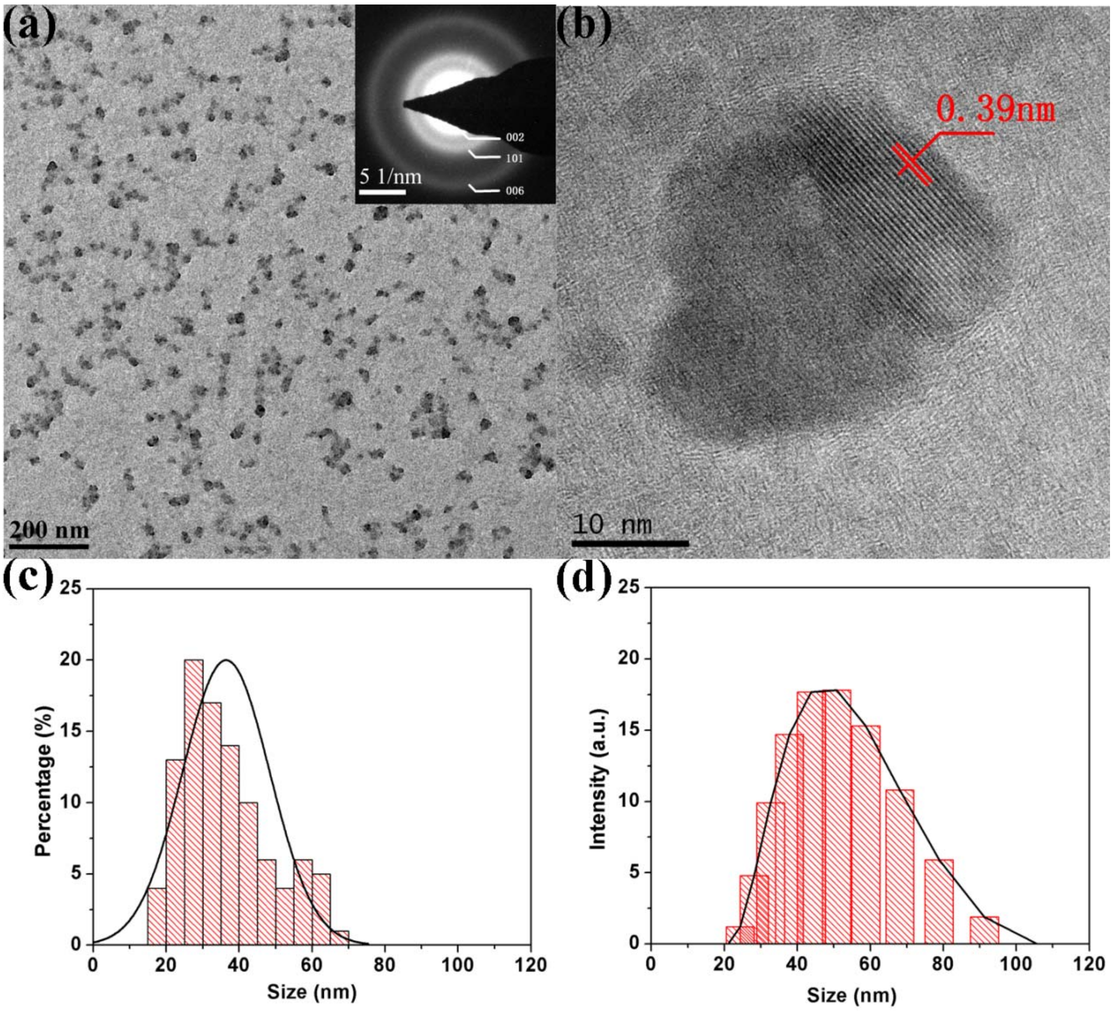

Figure 3.1 (a) TEM image of NCNPs; (b) High-resolution TEM image of NCNPs; (c) Size distribution of NCNPs measured by TEM; (d) DLS size distribution of NCNPs in DI water.

Well dispersed NCNPs were obtained by hydrothermal treatment of 40 mg glucosamine-HCl in 40 ml solution at 140 °C (Figure 3.1). In contrast, there are no CNPs formed when glucose was employed at such low temperature, instead of glucosamine-HCL with the equal concentration and following the same hydrothermal treating procedure. From the results of TEM study and the size distribution histograms shown in Figures 3.1 a-d, the NCNPs appear to be near spherical in morphology and well dispersed. Calculation from the TEM image gave a particle size range of 15 to 70 nm with an average size of ~35 nm. The larger size of the as-prepared NCNPs is due to the lace of KH_2PO_4. If there is no KH_2PO_4 in the reaction system, the carbon nuclei clusters can grow and isotropically assemble together to attain the large carbon particles. As shown in Figure 3.1 b, a partially nanocrystalline structure is observed for individual NCNPs by high-resolution TEM. The lattice spacing of 0.39 nm measured from high-resolution TEM closely matches with the (002) lattice spacing of disordered carbon materials [44, 67]. The nanocrystalline domains of the NCNPs were also verified by the selected-area electron diffraction (SAED) pattern (inset in Figure 3.1 a). Some amorphous domains were also observed in the NCNPs as shown in Figure 3.1 b. The co-existence of the nanocrystalline and amorphous domains in the NCNPs was also confirmed by the XRD study (Figure 3.2), which shows a weak and broad reflection center. (+ labeled in Figure 3.2). The as-synthesized NCNPs without any further surface modification could be easily dispersed in DI water with an average size of 47 nm being measured by DLS as shown in Figure 3.1 d. The discrepancy of ~12 nm in average size measured between the DLS and TEM results suggests the existence of certain hydrophilic functional groups on the surface of the NCNPs, which make the hydrodynamic diameter larger. When the NCNPs were dispersed in DI water, their hydrophilic functional groups extended in water and were counted by the DLS.

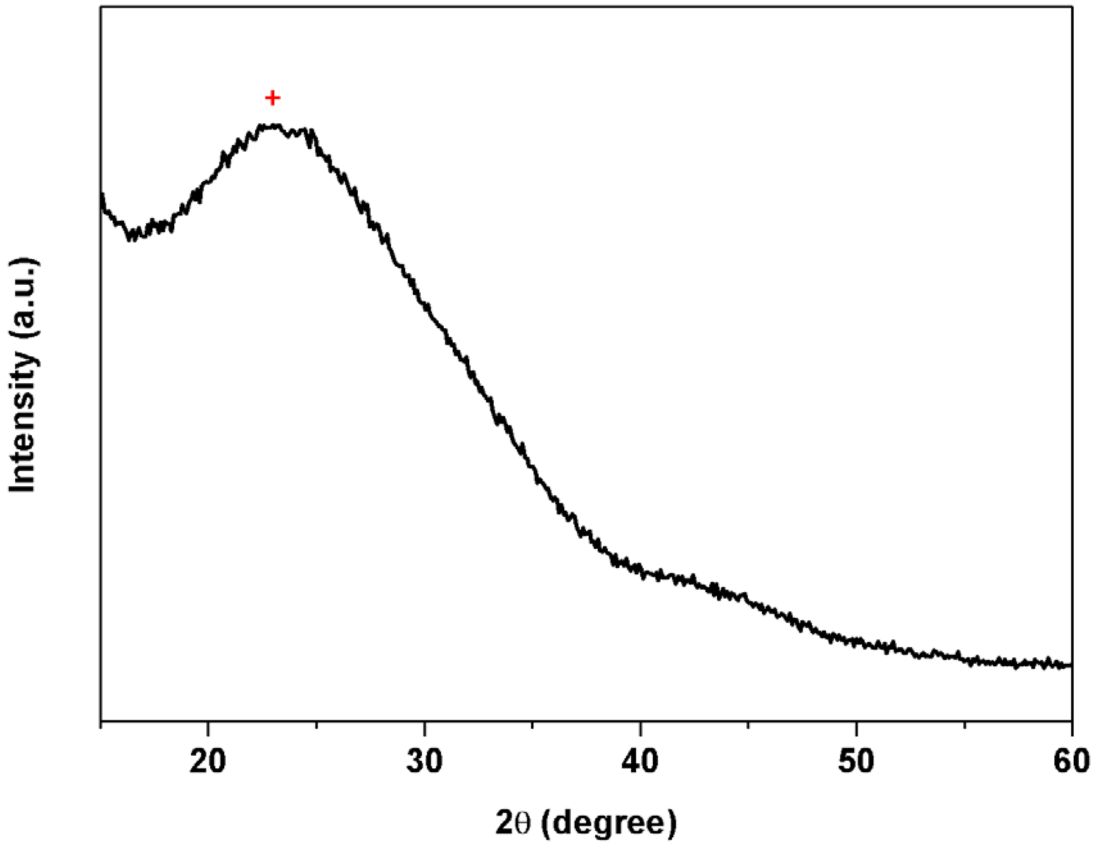

Figure 3.2 XRD pattern of the as-synthesized nitrogen-containing carbon nanoparticles.

Figure 3.3 shows the Raman spectrum of the NCNPs. The spectrum recorded between 1000 and 1900 cm^{-1} is typical for carbonized materials [194]. The broad peak at 1346 cm^{-1} is associated with benzene ring-breathing vibrations and assigned to D band, corresponding to the amorphous structure of carbon in the particles [11, 194]. The peak at 1556 cm^{-1} matches well with the 1st order G band [11, 223, 224]. In addition, this peak is broader than the common 1st order G band, which demonstrates that the NCNPs contain aromatic and olefinic molecule pieces inside the particle giving rise to in-plane bond-stretching motion of the C sp^2 atoms pairs, confirming intramolecular dehydration of the glucosamine molecule [194, 224]. As shown in Figure 3.3, the band overlapping at 2155 cm^{-1} indicates the presence of nitrogen in the NCNPs, as has been observed in the Raman spectra of nitrogen doped diamond [225-228].

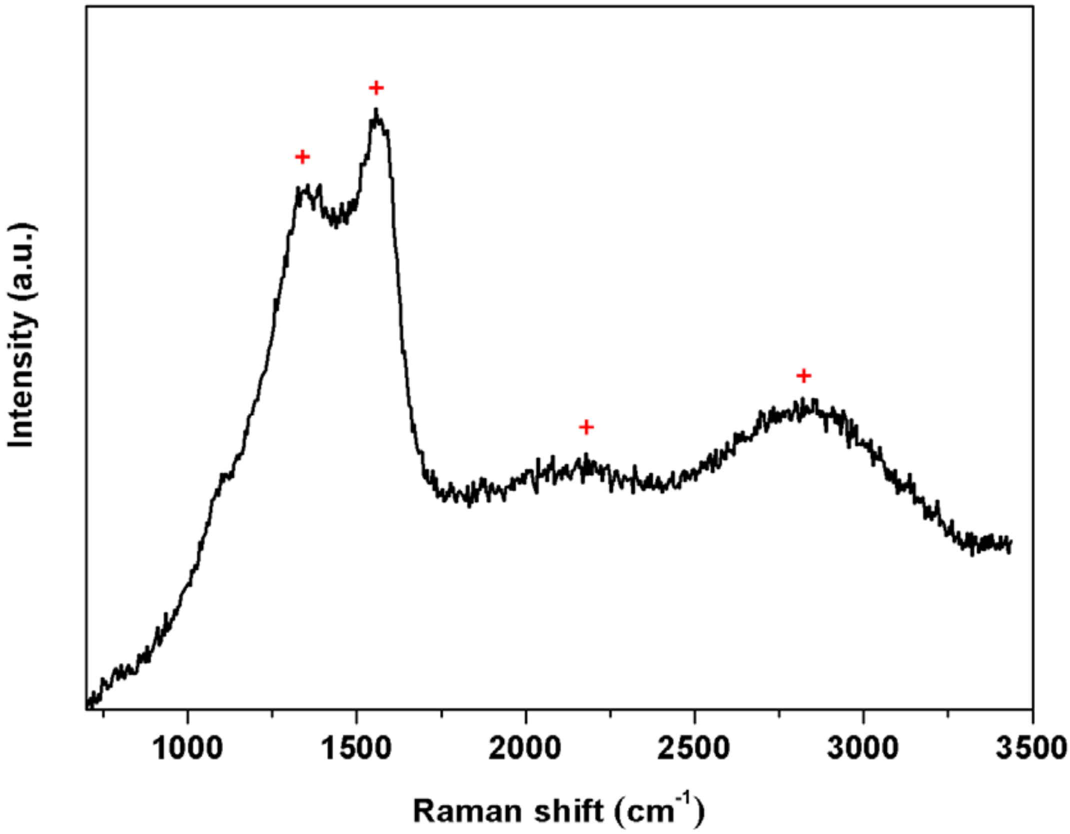

Figure 3.3 Raman spectrum of the NCNPs formed by hydrothermal process at 140 ^{o}C.

This is obviously related to the different chemical structures between glucose and glucosamine-HCl. There is one -NH_2 group in each glucosamine molecule, and the -NH_2 group provides the nitrogen doping during carbonization. The band overlapping at 2818 cm^{-1} is assigned to graphite impurity, which consists of 2nd order band of graphite and sp^3 C-H_x groups [194, 224]. Therefore the Raman spectroscopic study confirms the carbonization of glucosamine-HCl by hydrothermal treatment at 140 ^{o}C, giving rise to the formation of the NCNPs consisting of both nanocrystalline and amorphous domains. It agrees well with the TEM studies.

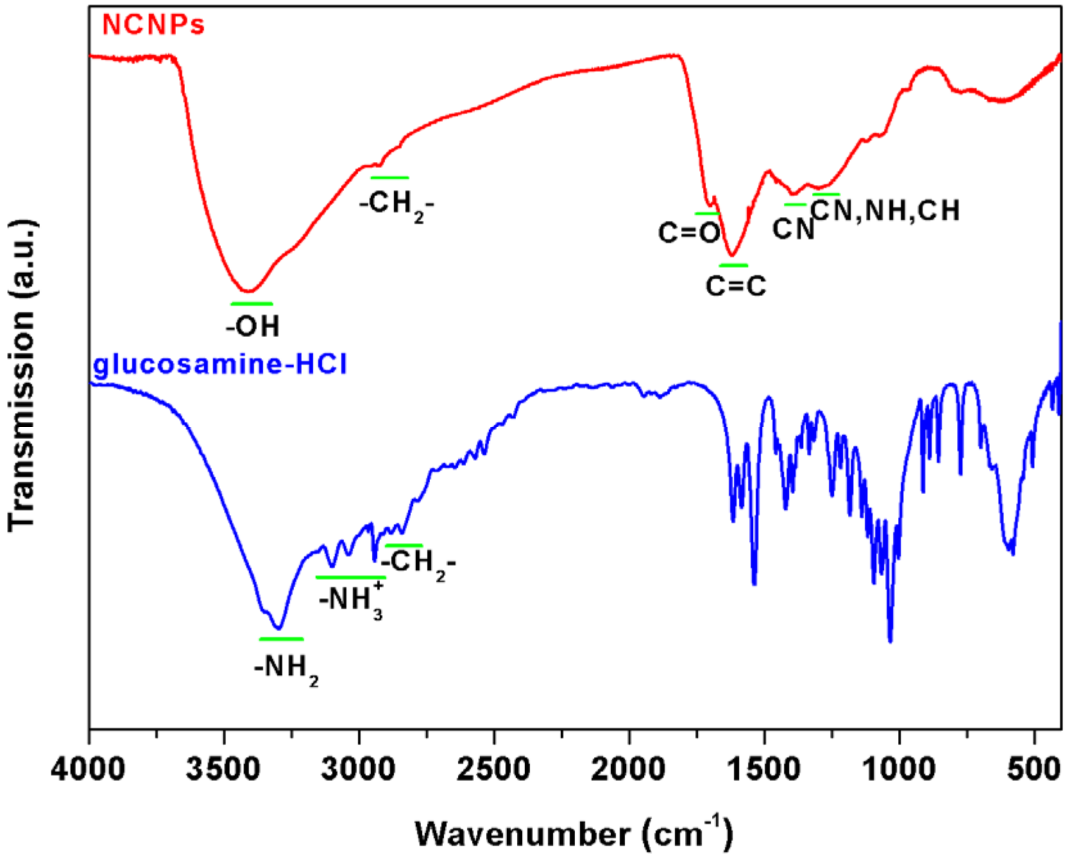

Figure 3.4 FTIR spectra of the as-synthesized NCNPs and glucosamine-HCl.

FTIR spectra were acquired in order to understand the chemical structure of the NCNPs derived from glucosamine-HCl. Comparing between the FTIR spectrum of glucosamine-HCl and that of NCNPs (Figure 3.4), the dehydration and aromatization during the hydrothermal process are verified, where the carbonization is demonstrated by the decreasing intensities of -CH_2- vibration bands (2924 and 2851 cm^{-1}) and at the same time the increasing intensities of C=C vibration bands (1620 cm^{-1}) [44, 194]. Since glucosamine-HCl is a hydrochloride, the -NH_2 group (3292 cm^{-1}) is expressed as -NH_3^+ in the chemical structure, as demonstrated by the -NH_3^+ vibration band in the FTIR spectrum of glucosamine-HCl in Figure 3.4 [229]. In contrast, upon hydrothermal treatment, there is no such vibration band in the FTIR spectrum of the NCNPs, which confirms that the -NH_2 group was involved in the hydrothermal reaction to form a type of nitrogen-doping in NCNPs. The vibration bands at 1396, 1276 and 3404, 1706 cm^{-1} demonstrate the presence of the respective aromatic amine, hydroxyl and carboxyl groups in the NCNPs [44, 194, 230, 231]. In addition, the vibration bands at 1396 and 1276 cm^{-1} also confirm that carbonization occurred during the hydrothermal treatment and the aromatic amine group formed on the surface of NCNPs, because the vibration band at 3292 cm^{-1} for aliphatic amine group (FTIR spectrum of glucosamine-HCl) has been transformed to the aromatic amine group (FTIR spectrum of NCNPs). These functional groups render the NCNPs hydrophilic as demonstrated by their long term stability in aqueous solution. There is no precipitation observed when the sample was stored in DI water for one year.

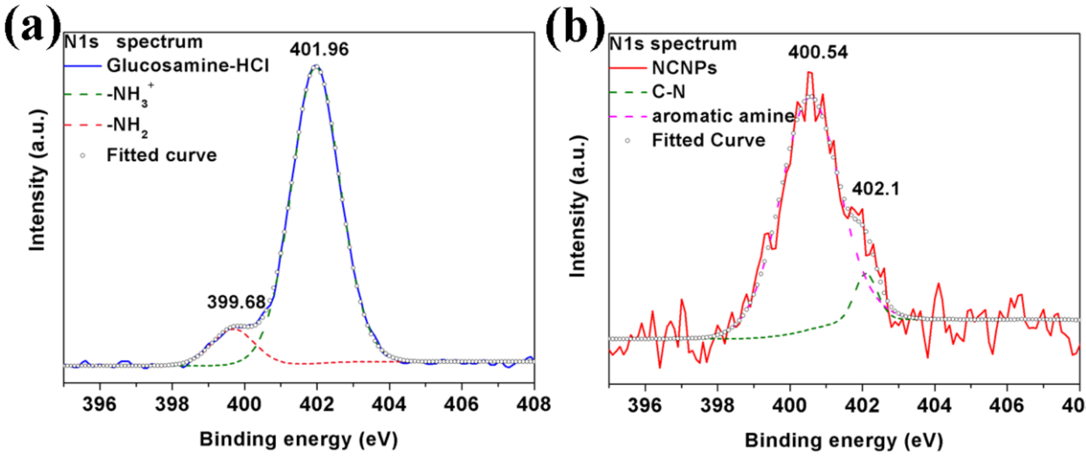

Figure 3.5 N 1s XPS spectra and peak determination of glucosamine-HCl (a) and the as-synthesized NCNPs (b).

To further investigate the types of nitrogen doped in the frame of NCNPs, XPS study was conducted for both glucosamine-HCl and NCNPs. Concerning the N 1s spectra, there are two peaks of N 1s for pure glucosamine-HCl, 399.68 eV corresponding to $-NH_2$ group and 401.96 eV corresponding to $-NH_3^+$ group. On the basis of the comparison between N 1s spectrum of the NCNPs and that of glucosamine-HCl, the binding energy of N 1s is changed upon the hydrothermal treatment. The 400.54 eV corresponds to aromatic amine group [232]. 402.1 eV is the C-N bond when nitrogen atom is inside the carbon matrix [230, 232]. The XPS study thus suggests that not only the aromatic amine group is on the surface of the NCNPs, but also nitrogen atom is also present inside the carbon matrix of the NCNPs with a rough amount of 2.24 At. %. In addition, the XPS spectrum of the NCNPs agrees well with the respective results of Raman and FTIR spectra, which indicate the presence of nitrogen doping in the NCNPs.

As demonstrated by the results of Raman, FTIR and XPS discussed above, the NCNPs exhibit surface functional groups, such as aromatic amine, hydroxyl and carboxyl groups. Both oxygen and nitrogen are present in the chemical structure of glucosamine-HCl. During the hydrothermal process, these two types of elements could provide oxygen and nitrogen for the defects formed within the sp^2 carbon fragment of NCNPs. They then lead to a passivated carbon surface for the NCNPs, making the NCNPs emissive. Although such large size carbon materials can influence the fluorescent emission because of the light absorption of black carbon, the green light florescence emission of the as-prepared NCNPs can still obtained if the testing solution is diluted 3 times.

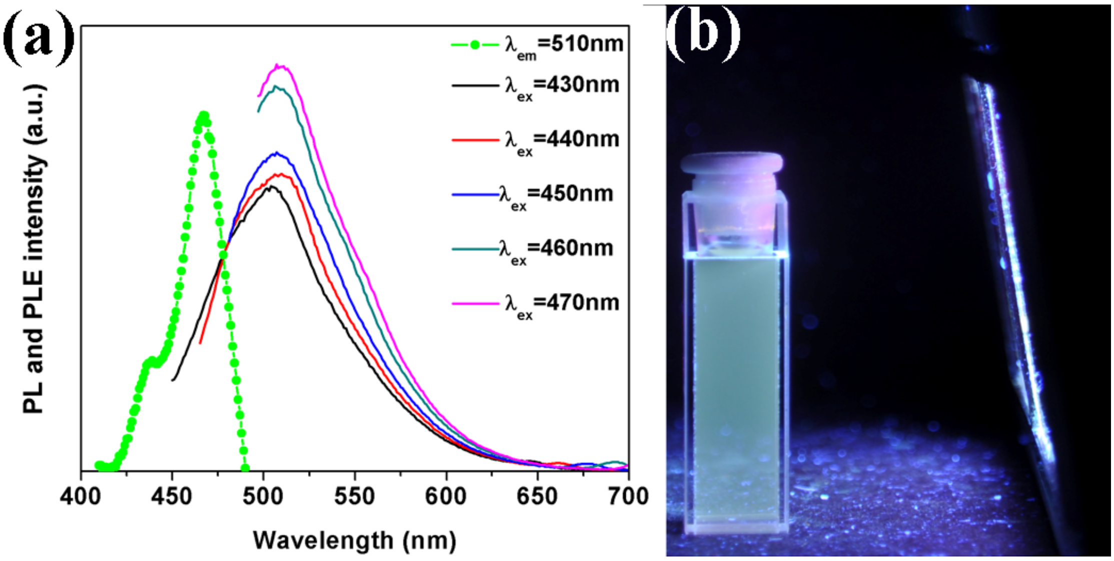

Figure 3.6 (a) PL and PLE spectra of NCNPs, where the PL spectra were recorded under 430 to 470 nm excitation wavelength (λ_{ex} = 430-470 nm) with 10 nm increase interval, and the PLE spectrum was recorded under 510 nm emission wavelength (λ_{em} = 510 nm). (b) Emission from the dispersion of NCNPs when irradiated by a 365 nm UV lamp.

As shown in Figure 3.6 b, when the aqueous dispersion of NCNPs is directly irradiated by a 365 nm ultraviolet (UV) lamp, it emits green colored fluorescence without any relationship with the nitrogen amount. When the NCNPs are excited by 430 nm incident light, there is a strong emission peak at around 510 nm, indicating a green light emission (Figure 3.6 a). When the excitation wavelength (λ_{ex}) is increased from 430 to 470 nm, the emission wavelength (λ_{em}) does not shift much. This phenomenon is different from what has been observed for the C-dots derived from glucose in chapter 2. When glucose is used as the starting material to synthesize fluorescent carbon nanoparticles, the PL emission is shifted towards longer wavelengths by increasing λ_{ex}. The phenomenon is due to the different distribution of emissive trap sites on the surface of carbon nanoparticles [69]. However, when glucosamine-HCl is used as the starting material for NCNPs, the λ_{ex}-independent λ_{em} is similar to the fluorescent carbon nanoparticles treated with nitric acid and the carbon materials containing nitrogen on the surface [37, 70, 206]. The λ_{ex}-independent emission arises from the effect of different surface passivation atoms. Such λ_{ex}-independent fluorescence behavior would make the NCNPs useful for reliable bioimaging and cell labelling, where the unwanted autofluorescence can be avoided. When glucose is carbonized, only oxygen is expected on the surface of carbon nanoparticles, which exhibit defect sites to trap the excitation energy. However, glucosamine-HCl contains both oxygen and nitrogen atoms. When glucosamine-HCl is carbonized to the NCNPs, the surface will be passivated by the functional groups containing both oxygen and nitrogen atoms. These functional groups will create additional types of defect sites to trap the excitation energy. As has been reported, when glucose is treated with nitric acid in the synthesis of luminescent C-dots, the PL shift in association with increasing λ_{ex} is reduced [70]. This supports the discussion that the surface functional groups containing both oxygen and nitrogen decrease the red shift of PL caused by increasing λ_{ex}. In addition, when the λ_{em} is set at 510 nm, there are two peaks in the PLE spectrum (Figure 3.6 a), centered at 430 and 470 nm, respectively. This behavior also indicates that there are at least two types of excitation energy trapped on the surface of NCNPs.

3.3.2 Formation mechanism of NCNPs

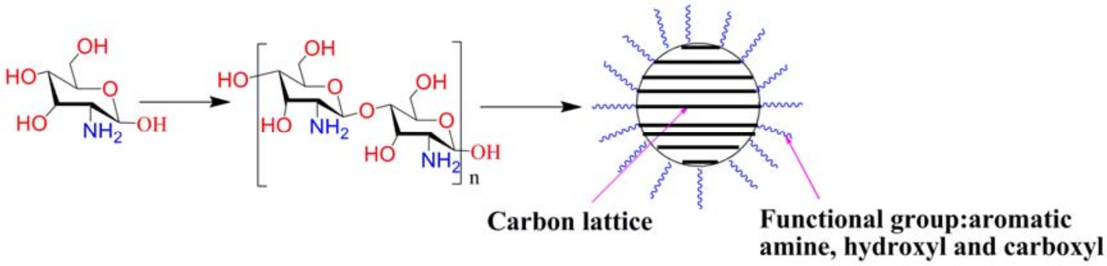

Figure 3.7 Schematic illustration of the formation of NCNPs from glucosamine-HCl in hydrothermal process.

There are several schemes that have been proposed for the formation of carbon nanoparticles from saccharides through hydrothermal process in the temperature range from 150 to 350 ^{o}C [11, 188, 190, 194]. Based on the experimental results, we propose a formation scheme for the NCNPs from glucosamine-HCl, which is shown in Figure 3.7. To start with, glucosamine molecules are connected via an intermolecular dehydration, which is similar to what is involved in the formation of carbon nanoparticles from glucose at temperatures above 150 ^{o}C [11, 188]. With the increase in hydrothermal reaction time, a “polymerization” process takes place, where glucosamine molecules are aromatized by intramolecular dehydration [233]. At the local critical aromatic cluster supersaturation condition, a burst of nucleation is resulted. The carbon nuclei then grow to partially nanocrystalline NCNPs with certain hydrophilic functional groups, such as aromatic amine, hydroxyl and carboxyl groups. During the process, intramolecular dehydration is an important step for the nuclei formation. The intramolecular dehydration is verified by the aromatic amine group observed on the surface of the NCNPs and the nitrogen inside the carbon matrix, which is demonstrated by the Raman, FTIR and XPS studies. The intramolecular dehydration temperature of carbohydrates, such as glucose or sucrose, is above 150 ^{o}C [188, 194]. The dehydration temperature of glucosamine-HCl is however lower, and therefore the NCNPs are developed at 140 ^{o}C [233].

3.4 Summary

A one-step hydrothermal synthetic process has been developed for forming nitrogen-doped carbon nanoparticles with intrinsically fluorescent behavior. The nitrogen-doped carbon nanoparticles derived from glucosamine-HCl exhibit hydrophilic functional groups, making them stable in aqueous environment. Under the λ_{ex} of 430 to 470 nm, they are demonstrated to emit green fluorescence (510 nm). Typically, the nitrogen-doped carbon nanoparticles show a λ_{ex}-independent emission behavior under this excitation range. On the basis of the experimental observation in the present work, a formation scheme is proposed for the nitrogen-doped carbon nanoparticles from glucosamine-HCl. In principle, the hydrothermal synthetic process could be easily adopted for a large scale synthesis of the nitrogen-doped carbon nanoparticles. The functional groups, such as aromatic amine, hydroxyl and carboxyl groups are present in the nitrogen-doped carbon nanoparticles, which can be further functionalized for specific applications in biomedical, catalysis and chromatography.

4 Hollow carbon spheres with tunable size and wall thickness

4.1 Background

As mentioned in chapter 1, monodispersed porous carbon spheres with controllable size promise for a number of technologically applications. Especially, for the application of Li ion battery, hollow carbon structure not only improves the rapid charge-transfer reactions, but also provides relatively large electrode/electrolyte interfaces. During the cycling process, the internal carbon wall can facilitate the transportation and collection of electrons. Amphiphilic molecules, such as block copolymers and surfactants, could form various vesicle structures through self-assembling by hydrogen bonding and hydrophobic/hydrophilic interactions in aqueous environments [143]. These vesicles could be used as soft templates for synthesizing hollow carbon spheres with an inner macropore and meso-/microporous external carbon wall. Based on this strategy, Vesicle structures formed by block copolymer poly (ethylene oxide)-poly (propylene oxide)-poly (ethylene oxide) (PEO-PPO-PEO) are used as soft template, and α-cyclodextrin (α-CD) as the carbon precursor, which can be threaded onto PEO chains dangling on the vesicle surface. This unique approach is on the understanding that PEO chains in PEO-PPO-PEO can penetrate into the inner cavity of α-CD, which is a series of cyclic oligosaccharides, forming an inclusion type of supermolecular complexes [234, 235]. An important consideration is the strong hydrogen bonding between α-CD molecules, when they are threaded onto the PEO chains. It has been demonstrated that a stronger bonding between the carbon precursors would lead to a more orderly structure [71, 143]. Moreover, the commercially available block copolymer PEO_{106}-PPO_{70}-PEO_{106} (F127) is a desirable choice of the soft template. Indeed, it has been widely used as template for synthesizing mesoporous carbon materials, due to its well established chemical behavior [71]. Upon establishing the vesicle structure, where α-CD is threaded on the PEO chains, α-CD will then be converted to carbon structure by hydrothermal treatment [187, 194]. The F127 as soft template is then removed by pyrolysis under argon (Ar) gas protection to yield the meso-/microporous carbon wall. As detailed in the result and discussion below, the uniquely new approach leads to monodispersed hollow carbon spheres of controllable size and morphology.

4.2 Experimental details

4.2.1 Materials

F127 is purchased from Sigma-Aldrich Company. α-CD is purchased from Tokyo Chemical Industry Company.

4.2.2 Synthetic procedure of hollow carbon spheres

Various amounts of F127, namely 7.5, 15 and 30 mg, respectively, were dissolved in 20 mL deionized (DI) water and stirred at room temperature overnight. 60 mg of α-CD in 20 mL DI water was injected into the solution of F127 under stirring at 700 rpm. The mixed solution was stirred overnight and then transferred into a Teflon sealed autoclave chamber. Upon hydrothermal treatment at 200 ^{o}C for 6 h, the as-prepared hollow carbon spheres was collected and washed by DI water three times by centrifuging at 9000 rpm for 30 min. After washing, the black precipitates were re-dispersed in DI water and centrifuged at 500 rpm for 30 min to remove the large agglomerated particles. Finally, the suspension was collected and freeze dried for two days to obtain the monodispersed hollow carbon spheres for further study. The as-prepared and dried hollow carbon spheres were pyrolyzed in a tube furnace at 900 ^{o}C for 6 h under Ar gas protection.

4.2.3 Characterization

The size, morphology and microstructure of the hollow carbon spheres were studied by using Scanning electron microscope (SEM) (XL 30 FEG-SEM Philips) and transmission electron microscopy (TEM) (CM 300 FEG-Philips). Raman and Fourier transform infrared (FTIR) measurements were conducted by following the same procedure mentioned in chapter 2. Dynamic light scattering (DLS) and X-ray diffraction (XRD) measurements were detailed in chapter 3. The amount of oxygen (O) on the surface of the hollow carbon spheres was investigated using X-ray photo-electron spectroscopy (XPS) (AXIS Ultra). The surface areas of the hollow carbon spheres were measured by using nitrogen (N_2) and carbon dioxide (CO_2) on a Micromeritics ASAP 2020 system. Their surface areas were evaluated by Brunauer-Emmett-Teller (BET) method according to N_2 adsorption data in the relative pressure (P/P_0) range of 0.06-0.2. The nonlocal density functional theory (NLDFT) and Dubinin-Astakhov pore size distributions were calculated by analyzing the adsorption branch of the N_2 isotherms and the CO_2 adsorption isotherms, respectively.

4.2.4 Electrochemical performance

Electrochemical behavior of the hollow carbon spheres as the anode in lithium (Li) ion batteries was investigated. The working electrode was fabricated by coating the slurry of hollow carbon spheres (80 wt. %), carbon black (10 wt. %), and polyvinylidene fluoride (PVDF) (10 wt. %) in *n*-methyl pyrrolidinone (NMP) onto a copper (Cu) foil. The coated Cu foil was then dried in a vacuum oven at 120 ^{o}C for 12 h. Furthermore, Li foil with thickness and diameter of 0.4 and 14 mm, respectively, was used as the counter electrode, while Celgard 2325 membrane was utilized as the separator, and 1 M lithium hexafluorophosphate ($LiPF_6$) in ethylene carbonate (EC) and dimethyl carbonate (DMC) (1:1 by volume) was used as electrolyte. They were assembled into a 2032 button cell in argon-filled glove box, in which both the moisture and oxygen (O_2) level were controlled to be less than 1 ppm. The cells were charged and discharged on MACCOR 4200 battery & cell test equipment within the voltage range of 3~0.005 V (vs. Li/Li^+) at a current density of 50 mAg^{-1} at room temperature.

4.3 Results and discussion

4.3.1 Structure of hollow carbon spheres

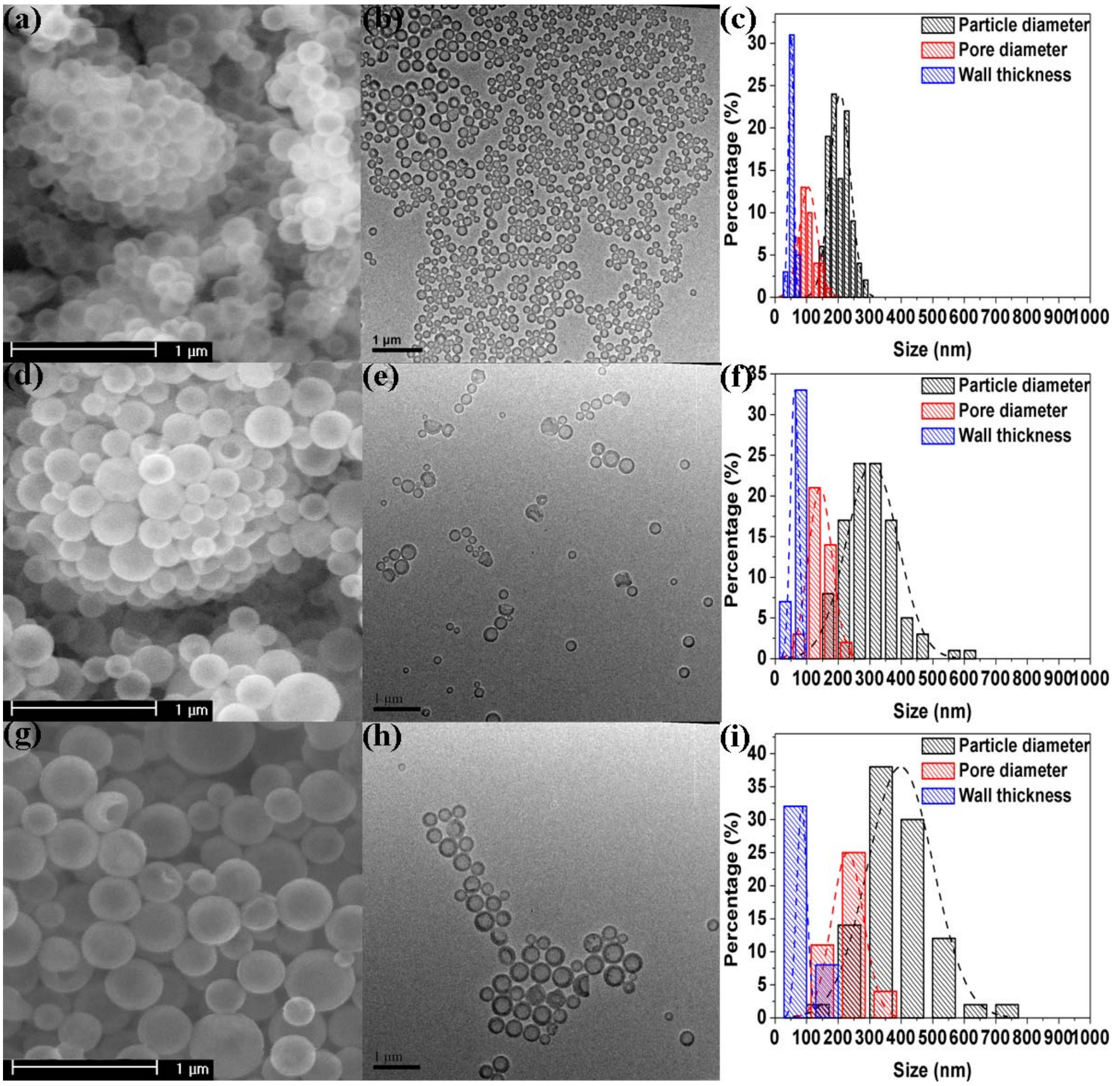

Figure 4.1 SEM and TEM images of the as-synthesized hollow carbon spheres by after hydrothermal treatment. (a), (b) and (c) are SEM image, TEM image and size distribution histograms of HCS-1, respectively. (d), (e) and (f) are SEM image, TEM image and size distribution histograms of HCS-2, respectively. (g), (h) and (i) are SEM image, TEM image and size distribution histograms of HCS-3, respectively.

SEM and TEM were employed to study the size, morphology and texture of the as-synthesized hollow carbon spheres. Figure 4.1 a, d and g show the SEM images of hollow carbon spheres derived from 40 ml aqueous solution of 60 mg α-CD in the presence of 7.5, 15 and 30 mg F127 by hydrothermal treatment, which are denoted as HCS-1, HCS-2 and HCS-3, respectively. From these SEM images, the as-synthesized particles are seen to exhibit a spherical morphology.

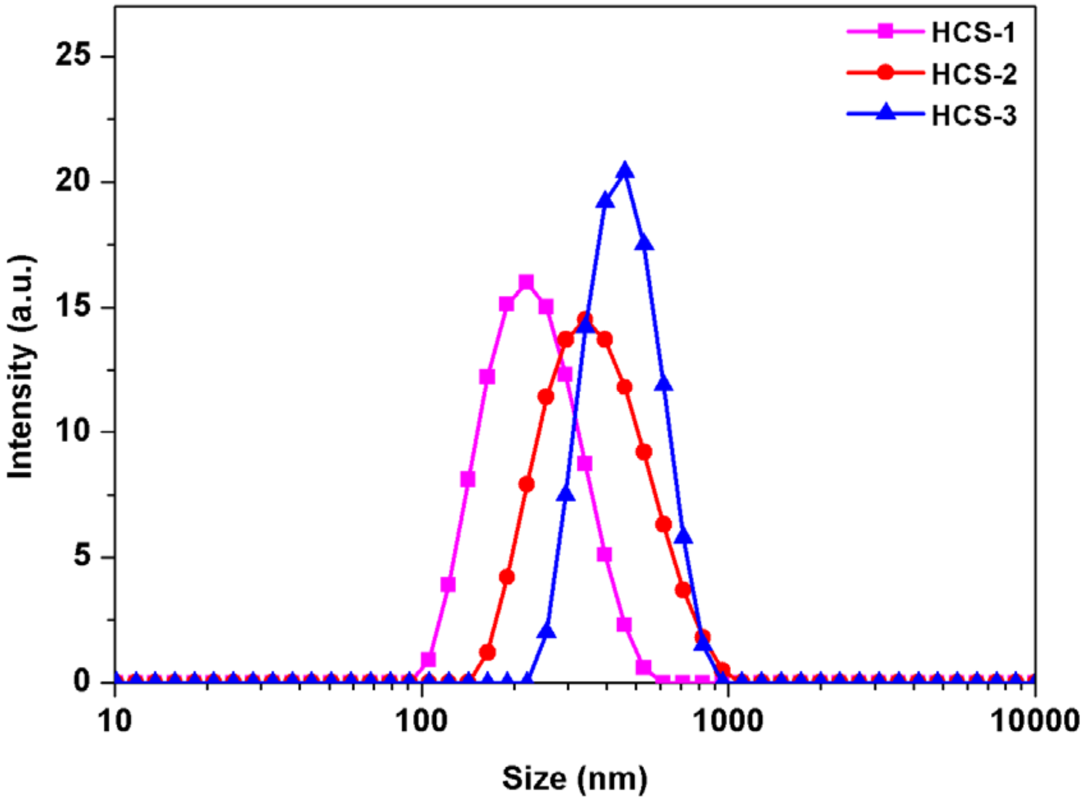

Figure 4.2 DLS size distribution of the hollow carbon spheres in DI water formed from hydrothermal treatment of α-CD in the presence of various amount of F127.

In addition, as shown in Figure 4.1 b, e and h, which are the respective TEM images of HCS-1, HCS-2 and HCS-3, these hollow carbon spheres exhibit well established hollow structure. Moreover, the average size of hollow carbon spheres measured by TEM and SEM increases when the amount of F127 in the solution is increased. The increase in the average size of HCS-1, HCS-2 and HCS-3 is shown in the distribution histograms in Figure 4.1 c, f and i, respectively. As shown in the size distribution histograms, the averaged particle diameter of HCS-1, HCS-2 and HCS-3 is 200, 300 and 400 nm, respectively. In addition, the averaged inner pore diameter of hollow carbon spheres also increases with increasing concentration of F127 in the solution. For HCS-1, HCS-2 and HCS-3, the average pore diameter is 100, 140 and 220 nm, respectively. The average wall thickness of HCS-1, HCS-2 and HCS-3 is measured to be 50, 60 and 80 nm, respectively. These particle and pore size distribution results show that the particle diameter, size of inner pore and wall thickness of hollow carbon spheres are tunable by just varying the concentration of F127. Since the as-synthesized hollow carbon spheres by hydrothermal treatment are well dispersed in DI water without any further surface modification, their hydrodynamic size and size distribution in water were measured by using DLS. As shown in Figure 4.2, the hydrodynamic size of HCS-1, HCS-2 and HCS-3 increases as the amount of F127 increases, which agrees well with which is observed in SEM and TEM. The average hydrodynamic size measured by using DLS for HCS-1, HCS-2 and HCS-3 is 214, 341 and 441 nm with the polydispersity index (PDI) of 0.107, 0.125 and 0.068, respectively, which is larger than the average size measured by SEM and TEM. This indicates the existence of certain hydrophilic functional groups on the surface of the as-synthesized hollow carbon spheres, which make the hydrodynamic diameter larger. When the as-synthesized hollow carbon spheres were dispersed in DI water, these hydrophilic functional groups on surface extended and were counted by the DLS measurement.

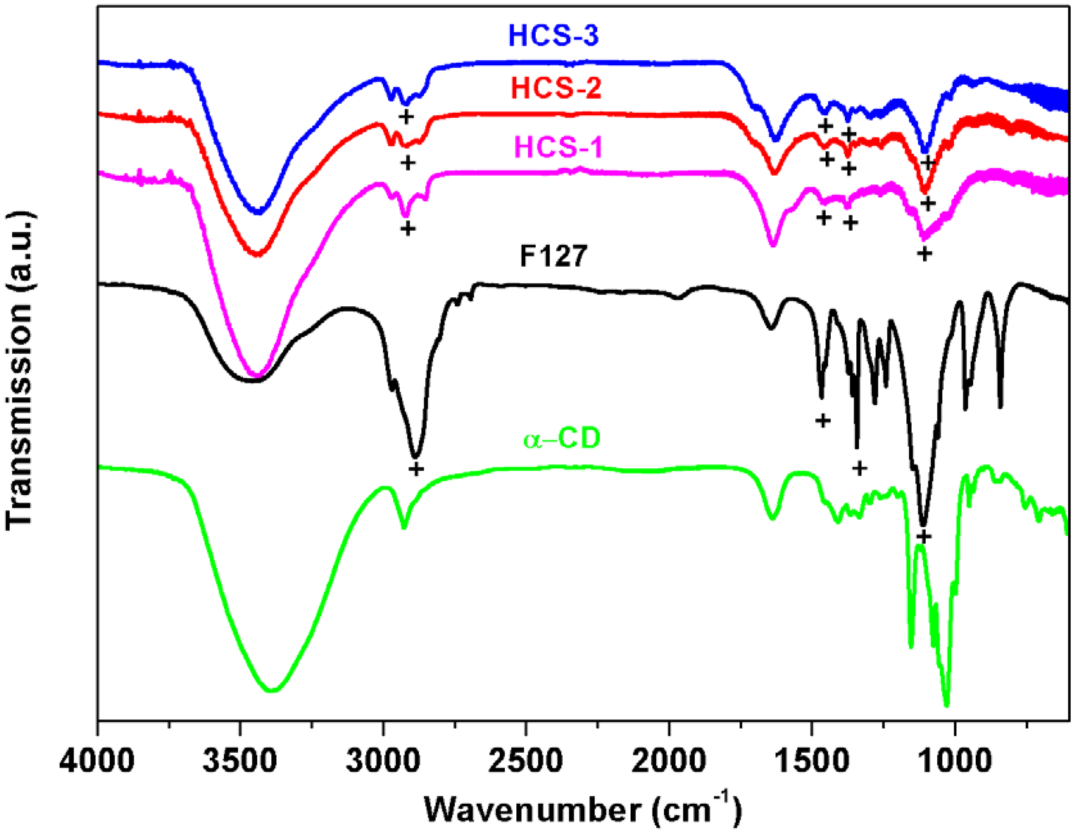

Figure 4.3 FTIR spectra of α-CD, F127 and hollow carbon spheres formed in the presence of various amounts of F127.

To study the chemical structure of hollow carbon spheres derived from hydrothermal treatment, FTIR spectroscopy was used to exam the functional groups. As shown by the similar FTIR spectra in Figure 4.3, HCS-1, HCS-2 and HCS-3 demonstrate similar chemical structure. By comparing the FTIR spectra of the as-synthesized hollow carbon spheres with α-CD, the carbonization of α-CD during the hydrothermal process is verified by the appearance of C=C vibration bands at 1635 cm^{-1} [44, 194]. In addition, after hydrothermal treatment, the hollow carbon spheres exhibit hydroxyl and carboxyl functional groups, which are demonstrated by the vibration bands at 3440 and 1704 cm^{-1}, respectively [44, 69, 211, 212]. Interestingly, by comparing between the FTIR spectra of the as-prepared hollow carbon spheres and F127 in

Figure 4.3, the molecular structure of F127 is largely retained under the hydrothermal condition, as demonstrated by the observation of the characteristic bands (2890, 1465, 1343 and 1109 cm^{-1}) of F127 block copolymer in the FTIR spectra of hollow carbon spheres, which are marked by + in Figure 4.3[236].

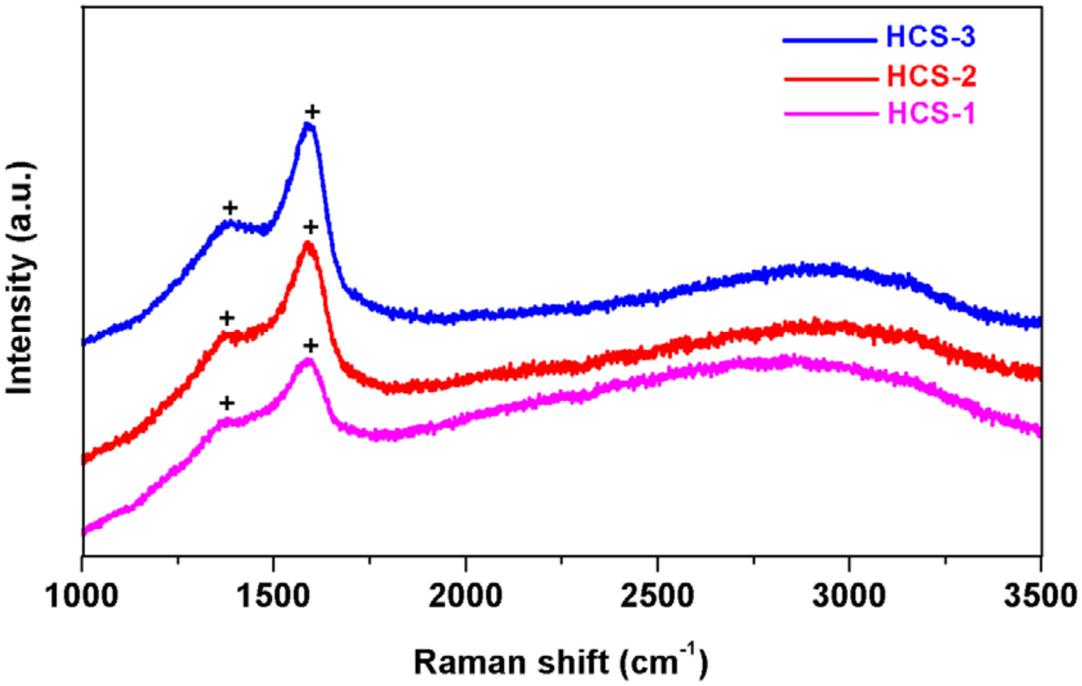

Figure 4.4 Raman spectra of the hollow carbon spheres derived from hydrothermal process.

To further confirm the structure of the as-synthesized hollow carbon spheres, Raman spectrometer was used to study the carbon structure. The Raman spectra of HCS-1, HCS-2 and HCS-3 as shown in Figure 4.4 all demonstrate a typical spectrum of carbonized materials, which is characterized by the peak at 1346 (D band) and 1556 cm^{-1} (G band) and labelled by + in Figure 4.4 [194, 224]. In addition, the G band in Figure 4.4 is broader than the normal G band of typical disordered graphite, indicating that there are aromatic and olefinic molecules co-existed in hollow carbon spheres because of the in-plane bond-stretching motion of the C *sp*^{2} atoms pairs [194, 224]. Moreover, there is a broad band in the range of 2500-3000 cm^{-1}, which could be assigned to the stretching mode of *sp*^{3} C-H$_x$ groups [194]. The Raman results agree well with the FTIR results, which demonstrate not only carbonization, happened but also the appearance of surface functionalization.

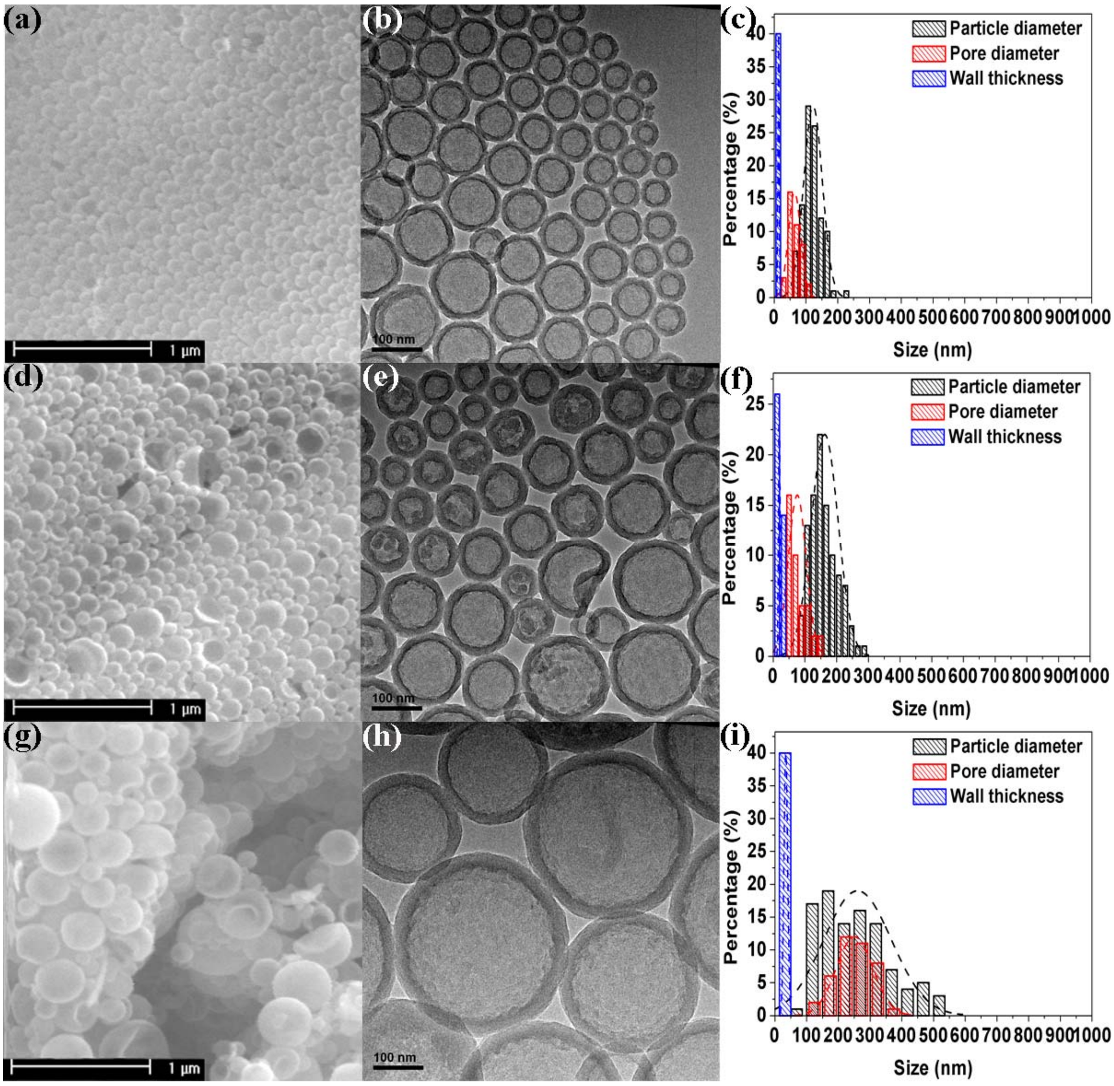

Figure 4.5 SEM and TEM images of the hollow carbon spheres after pyrolysis at 900 °C in Ar. (a), (b) and (c) are SEM image, TEM image and size distribution histograms of HCS-1a, respectively. (d), (e) and (f) are SEM image, TEM image and size distribution histograms of HCS-2a, respectively. (g), (h) and (i) are SEM image, TEM image and size distribution histograms of HCS-3a, respectively.

As discussed above, the monodispersed hollow carbon spheres exhibit a hybrid structure, where the carbon hollow spheres are surface-decorated by PEO chains. F127 molecules are expected to disintegrate upon an appropriate pyrolysis in an inert atmosphere. In our study, the as-prepared hollow carbon spheres were pyrolyzed at 900 °C for 6 h in Ar gas. SEM and TEM images of HCS-1, -2 and -3 after pyrolysis, which are coded as HCS-1a, HCS-2a and HCS-3a, are shown in Figure 4.5.

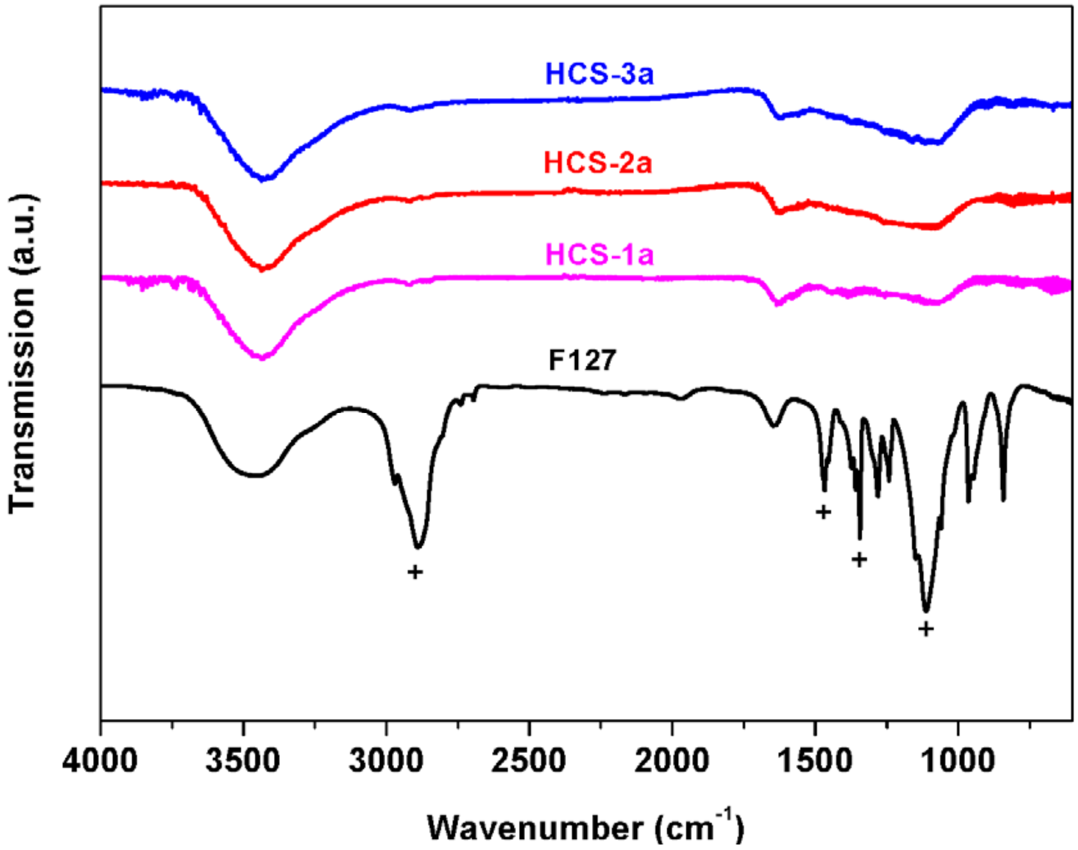

Figure 4.6 FTIR spectra of the hollow carbon spheres pyrolyzed at 900 °C in Ar and that of F127.

It is seen that the hollow spherical structure of HCS is well retained after the pyrolysis. The average particle diameter of the HCS-1a, HCS-2a and HCS-3a are measured as 122, 162 and 260 nm, respectively. In addition, the wall thickness of HCS-1a, HCS-2a and HCS-3a is measured to be 14, 19 and 34 nm, respectively. Both of the average diameter and wall thickness increase with the increase in the concentration of F127. Comparing the dimension of hollow carbon spheres before and after pyrolysis, it is noted that the overall carbon particle size and the average wall thickness are expectedly decreased after pyrolysis. Such decrease is apparently due to the decomposition of F127 and the functional groups in hollow carbon spheres, which leads to a shrinkage in the carbon particle size and wall thickness.

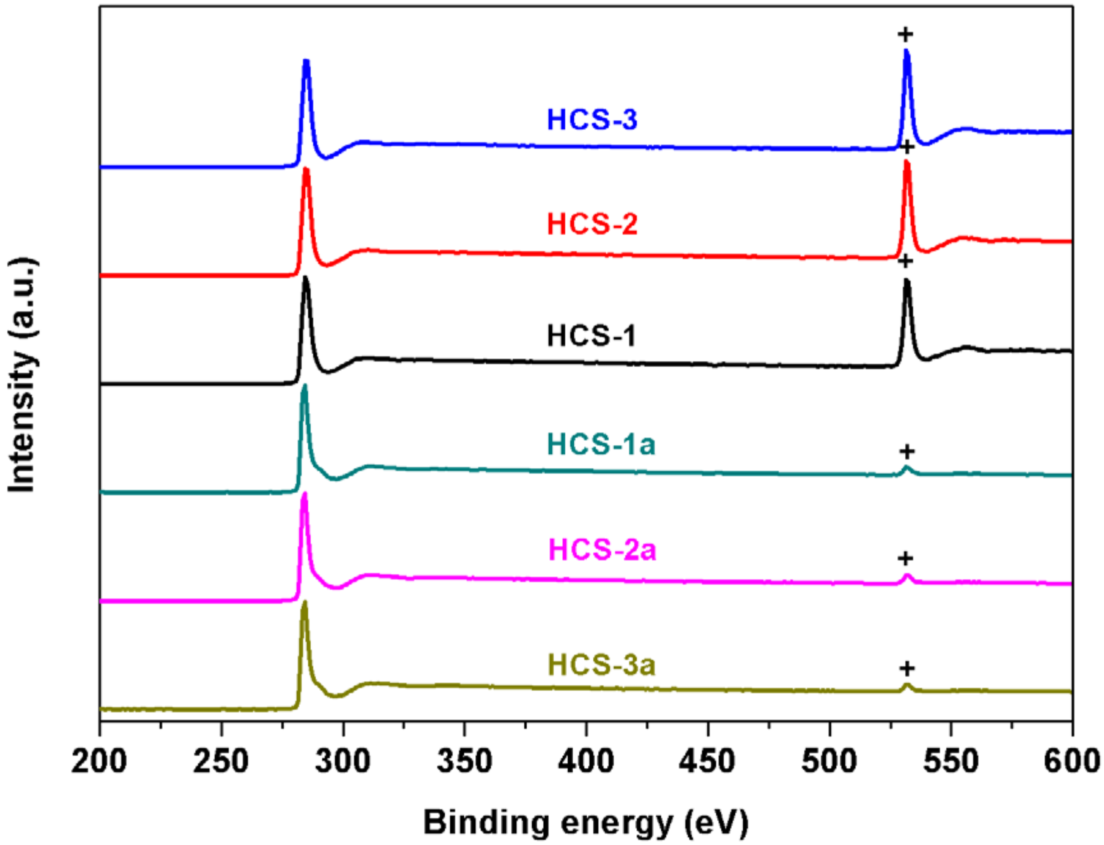

Figure 4.7 XPS spectra of the hollow carbon spheres before and after pyrolysis at 900 ^{o}C in Ar.

The decomposition of F127 through pyrolysis is confirmed by the studies of FTIR and XPS, which are shown in Figure 4.6 and Figure 4.7, respectively. As shown in Figure

4.6, similar FTIR spectra are observed with HCS-1a, HCS-2a and HCS-3a, which suggests that the pyrolyzed hollow carbon spheres exhibit similar chemical structure. By comparing the FTIR spectrum of the pyrolyzed hollow carbon spheres with that of F127 in Figure 4.6, the characteristic bands of F127 block copolymers, which are 2890, 1465, 1343 and 1109 cm^{-1}, are not present in the FTIR spectra of hollow carbon spheres after pyrolysis [237]. Furthermore, the decreases in intensity of oxygen peak (+ labeled in Figure 4.7) in the XPS spectra of the pyrolyzed hollow carbon spheres also demonstrates the decomposition of F127 and surface functional groups of hollow carbon spheres.

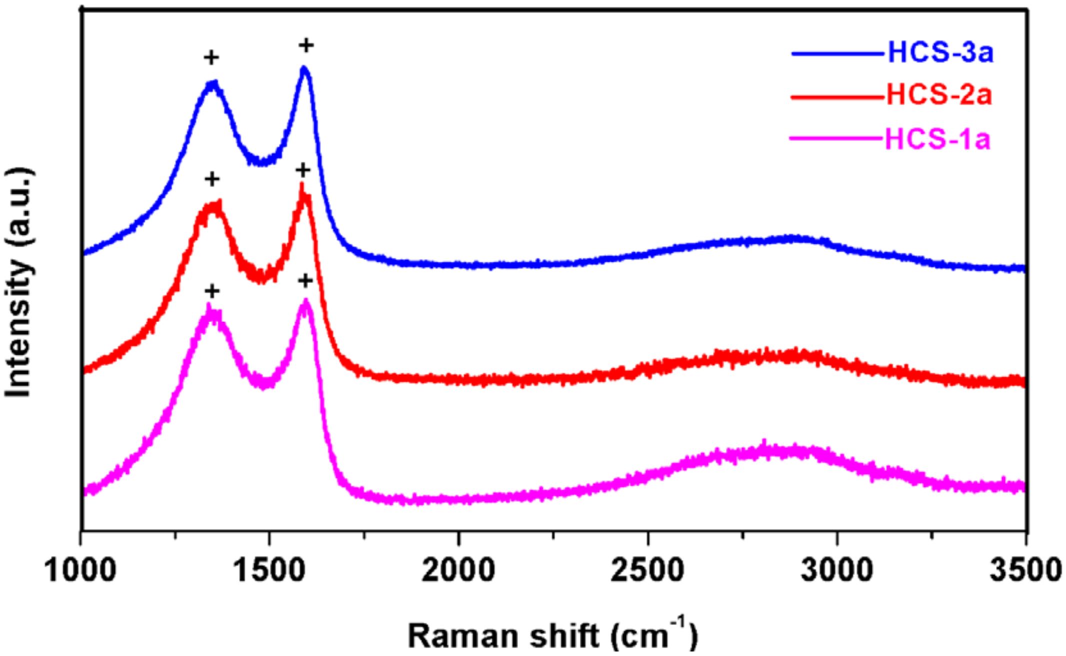

Figure 4.8 Raman spectra of the hollow carbon spheres pyrolyzed at 900 °C in Ar.

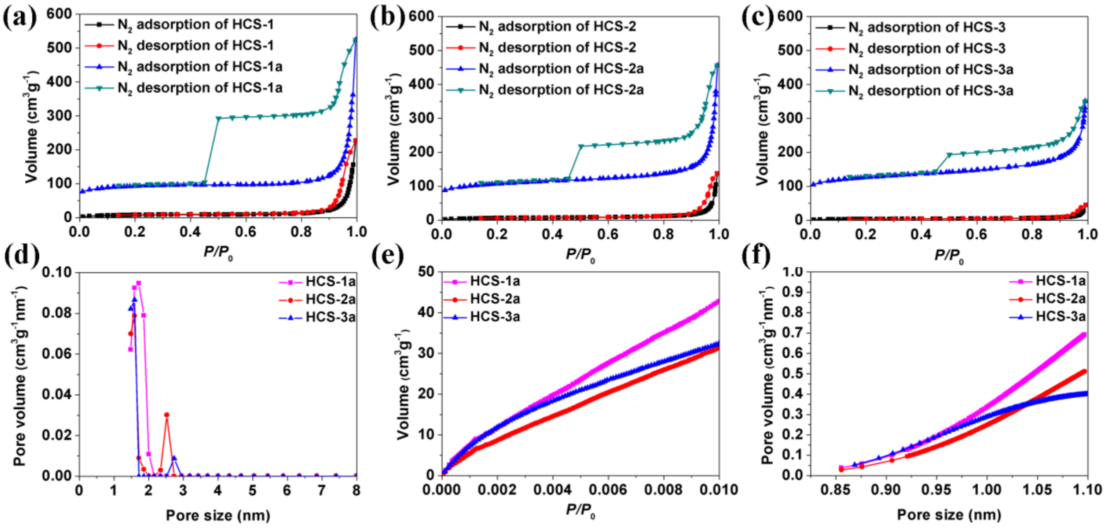

Figure 4.9 (a) N_2 adsorption/desorption isotherm curves of HCS-1 and HCS-1a; (b) N_2 adsorption/desorption isotherm curves of HCS-2 and HCS-2a; (c) N_2 adsorption/desorption isotherm curves of HCS-3 and HCS-3a; (d) NLDFT pore size distribution of the pyrolyzed hollow carbon spheres detected by N_2; (e) CO_2 adsorption isotherm curves of HCS-1a, HCS-2a and HCS-3a; (f) Dubinin-Astakhov pore size distribution of the pyrolyzed hollow carbon spheres detected by CO_2.

Both the 1346 (D band) and 1556 cm^{-1} (G band) in the Raman spectra of HCS-1a, HCS-2a and HCS-3a (Figure 4.8) are narrower than those in Figure 4.4, indicating the decomposition of F127 and further condensation of carbon shell under the high temperature treating in Ar, which agrees well with the TEM, FTIR and XPS results [194, 224].

The N_2 adsorption/desorption isotherms of the hollow carbon spheres are shown in Figure 4.9. For the as-synthesized hollow carbon spheres from hydrothermal treatment, negligible N_2 adsorption occurs in a range of relative pressure (P/P_0) of 0-0.9 indicating nonporous character of the wall before pyrolysis. A sharp increase in N_2 uptake at P/P_0 = 0.9-1.0 corresponds to the inter-particle voids, which becomes less significant as the particle size increases for the samples from HCS-1, HCS-2 to

HCS-3. The specific surface area of HCS-1, HCS-2 and HCS-3 calculated with the BET method is thus quite small with the values of 30.5, 22.7 and 12.9 m^2g^{-1}, respectively. For the isotherm of the pyrolyzed sample of HCS-1a (Figure 4.9 a), a specific BET surface area of 317.5 m^2g^{-1} was calculated from the isotherm in the range of low P/P_0 = 0.05-0.25. The NLDFT pore size distribution (Figure 4.9 d) shows there are pores (< 2 nm) spanning from micropores to mesopores in the wall, although detailed information on micropores is not provided by TEM image due to the lack of ordered microporous structure in the carbon walls. Because of the small sizes of such meso-/microporous, a long plateau is followed at higher pressures (0.25-0.9) indicating the full filling of the meso-/microporous. A sharp increase in N_2 uptake at P/P_0 = 0.9-1.0 corresponds to both the inter-particle voids and the hollow cavity. The desorption branch exhibits a large hysteresis loop in the range of P/P_0 = 0.4-1.0 with a sudden closure at P/P_0 = ~0.4. It represents ink-bottle type pores and is quite typical for hollow mesoporous spheres due to the delay of N_2 evaporation from the hollow voids blocked by the surrounding meso-/microporous carbon wall during the N_2 desorption process. From HCS-1a, HCS-2a to HCS-3a upon pyrolysis, the specific BET surface areas increases from 317.5, 374.2 to 431.3 m^2g^{-1}, respectively. A close examination shows that N_2 adsorption in the range of P/P_0 = 0.25-0.9 also increases for the samples from HCS-1a, HCS-2a to HCS-3a, indicating that more mesopores with a broad size distribution are created in the walls as the amount of F127 increases. This is confirmed by Figure 4.9 d showing an extension of the NLDFT pore size distributions to > 2 nm. It implies that F127 molecules act as the porogen in the wall of hollow carbon spheres. As more F127 is introduced into the walls with the increasing F127 amount, a large quantity of large pores is generated and randomly dispersed in the wall after decomposition of F127 at 900 °C. As a result, the breadth of the hysteresis loops decreases for the samples from HCS-1a, HCS-2a to HCS-3a, due to fewer blockages of N_2 evaporation from the hollow voids as the walls become more porous. In order to better understand the micropore feature of the carbon walls, CO_2 adsorption isotherms are measured and the Dubinin-Astakhov pore size distributions are calculated for the pyrolyzed samples (Figure 4.9 e and f). Clearly, micropores (0.85-1.1 nm) are present in the pyrolyzed hollow carbon spheres (Figure 4.9 f). Figure 4.9 f shows that the HCS-1a has the highest microporosity as compared to HCS-2a and HCS-3a.

From the experimental results discussed above, it could be concluded that, by hydrothermal treatment of α-CD in the presence of various concentrations of F127, hydrophilic and monodispersed hollow carbon spheres could be generated with tunable size and morphology.

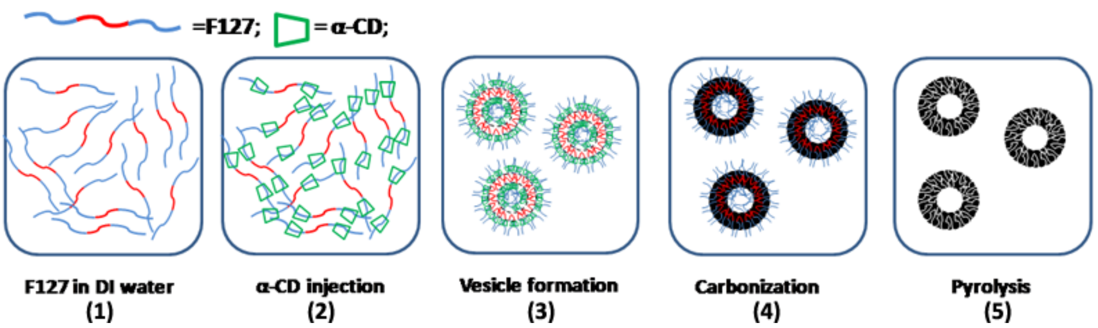

Figure 4.10 Schematic illustration of formation for monodispersed hollow carbon spheres, where the large vesicle structures were formed by block copolymer F127 when used as soft templates, and α-CD threaded on the PEO chains dangling on the surface of PEO-PPO-PEO vesicles.

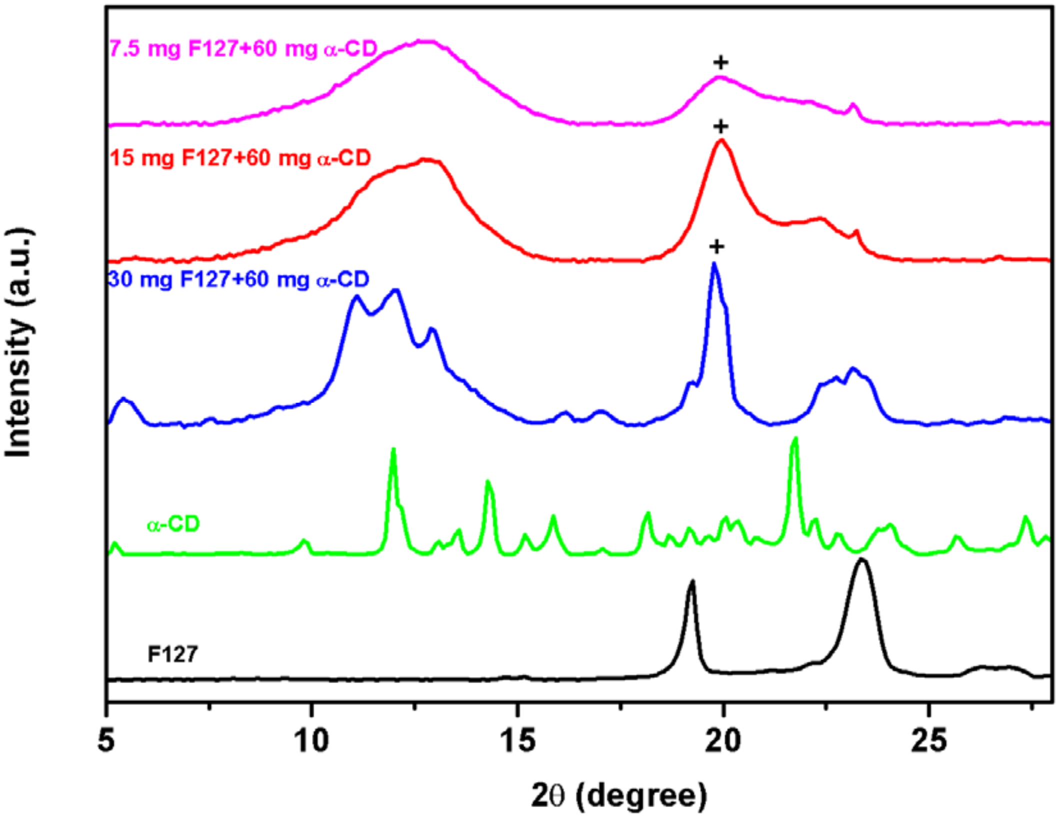

Figure 4.11 XRD results of pure F127, α-CD and the supermolecular inclusion complexes formed from α-CD (60 mg) and F127 at various content (7.5, 15, 30 mg) before hydrothermal treatment.

As detailed in Figure 4.10, F127 plays as the soft template while α-CD is the carbon precursor. According to the phase diagram of F127 shown in Figure 4.12, F127 dissolved in DI water at the designed mass concentration, which is 0.019, 0.037 and 0.075 wt. %, respectively, adapts single macromolecule [236].

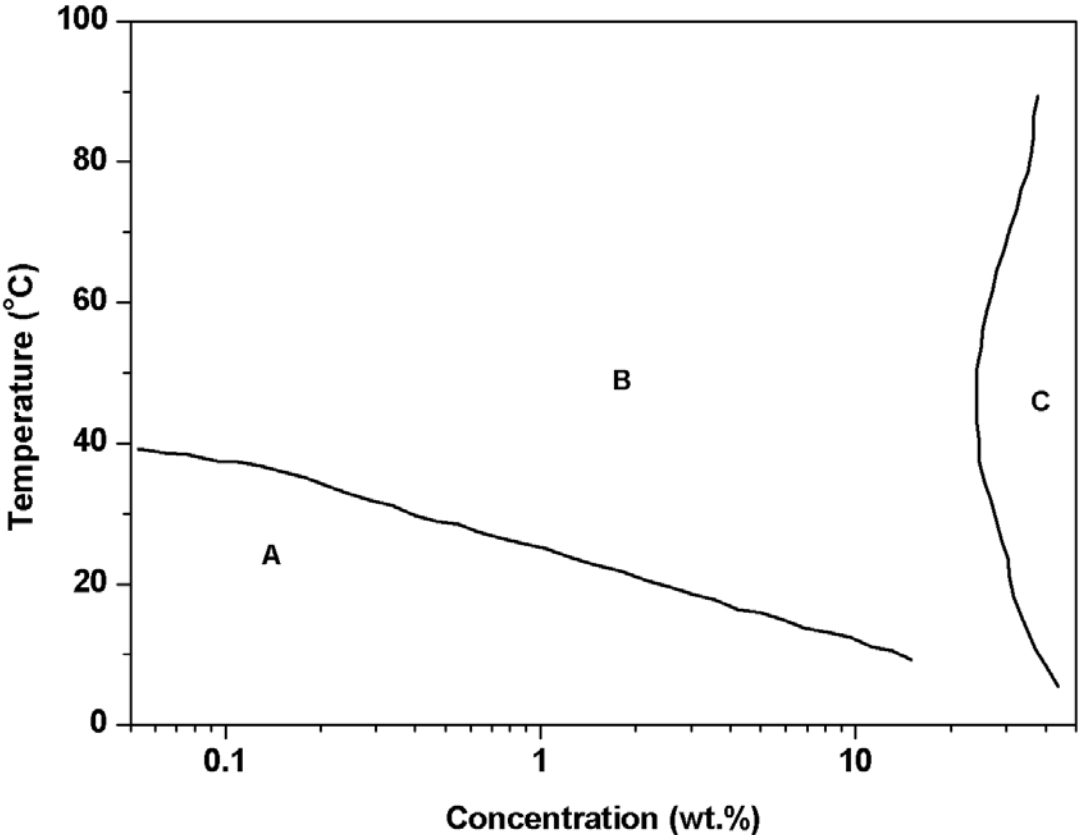

Figure 4.12 Illustration of the phase diagram of F127, where A, B and C denoted the single macromolecules, micelles and physical gel region, respectively. This phase diagram is adapted from [236].

Upon the injection of α-CD solution, the PEO block chain of F127 could penetrate into the inner cavity of α-CD molecules to form an inclusion type of supermolecular complexes [234, 235]. To demonstrate the expected supermolecular complexes, XRD studies are made on the freeze dried starting materials before hydrothermal treatment. As shown in Figure 4.11, the inclusion supermolecular complexes formed by threading α-CD onto the PEO blocks of F127 are confirmed by the appearance of the characteristic XRD peak of the channel type crystal structure of the α-CD, which is observed at 19.4° with F127/α-CD complexes (+ labeled in Figure 4.11) [234, 235]. This channel type ordered structure represents a kind of necklace-like supermolecular complex of α-CD and PEO, which comes from the penetration of F127 into the inner cavity of α-CD [238]. As compared in Figure 4.11, there is no such peak observed in the XRD results of pure F127 and α-CD, which further suggests the threading of PEO into the inner cavity of α-CD. Indeed, α-CD would exhibit a less symmetrical conformation, if there is no insertion in the cavity [239]. Under the hydrothermal condition, the F127/α-CD supermolecular complexes will be self assembled into a vesicle-type structure due to the hydrophobic/hydrophilic balances between PPO block in F127 and PEO/α-CD segment [240, 241]. The chemical structure of α-CD is a supermolecular containing 6 glucose unites. Therefore, the chemistry of α-CD under hydrothermal condition is similar with glucose, which contains dehydration, polymerization, aromatization and carbonization steps to form carbon materials at such temperature and pressure, simultaneously [187]. However, F127 is retained under the hydrothermal condition, as demonstrated by the FTIR result. As a result, the PEO block chains are present within the carbon wall of the as-synthesized hollow carbon spheres, giving rise to a hybrid structure which exhibits hydrophilic stability. Since the vesicle size of F127 could be varied by tuning the concentration of F127, the corresponding size of the hollow carbon spheres is tunable [240]. Finally, it is at the pyrolysis temperature of 900 ^{o}C that F127 is decomposed generating the observed meso-/microporous structure in the carbon wall.

4.3.2 Hollow carbon spheres as anode in Li ion battery

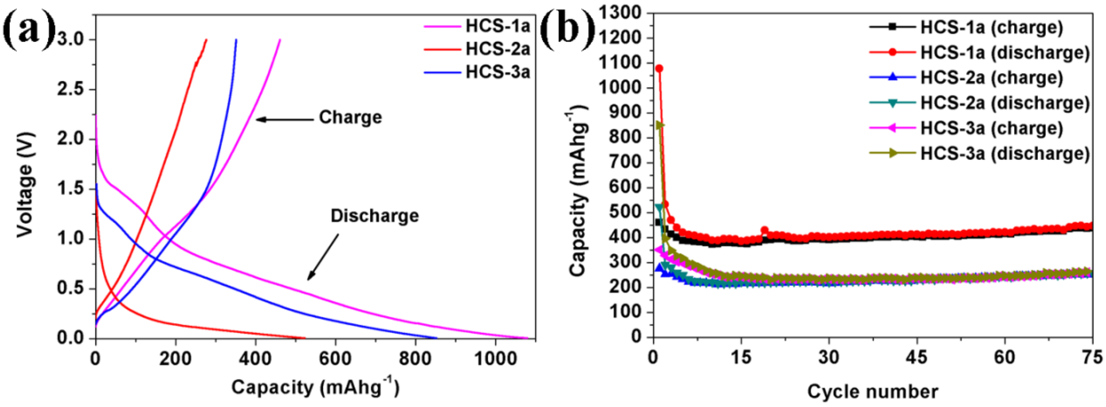

Figure 4.13 Li discharge/charge (Li insertion/extraction) curves (a) and Li ion battery cycling performance (b) of HCS-1a, HCS-2a and HCS-3a.

The electrochemical behavior of the pyrolyzed hollow carbon spheres when employed as an anode in Li ion battery is shown in Figure 4.13. The Li discharge/charge (Li insertion/extraction) curves are characteristic nano-carbon material [86]. From the discharge/charge (Li insertion/extraction) curves (Figure 4.13 a), the first reversible capacity of HCS-1a, HCS-2a and HCS-3a is calculated to be 462, 276 and 351 mAhg^{-1} at a rate of 50 mAg^{-1}, respectively. Figure 4.13 b shows the cycling performance of the hollow carbon spheres electrode measured under long-term cycling up to 75 cycles at the rate of 50 mAg^{-1}, revealing a good reversibility and cyclic performance. Even after 75 cycles, the specific capacity of the hollow carbon spheres electrode maintains a value of 443, 266 and 265 mAhg^{-1} for HCS-1a, HCS-2a and HCS-3a, respectively. Such electrochemical performance could well be attributed to the porous structure of the pyrolyzed hollow carbon spheres. As shown from Figure 4.5, HCS-1a has the thinner carbon wall, which enables an effective utilization of both of the external and internal surface of the hollow carbon structure for Li-storage.

Furthermore, the micropore structure of carbon materials can influence the thermodynamic factor of the Li ion adsorption [242, 243]. According to the analysis of the micropore structure in Figure 4.9, HCS-1a has the highest micropore volume, which leads to the highest Li ion adsorption energy. As a result, the capacity of HCS-1a is higher than the other two samples. The first reversible capacity of HCS-1a is higher than the theoretical capacity calculated for graphite, which is 372 $mAhg^{-1}$ [86, 87]. This indicates that the hollow carbon spheres prepared in the present work could be promising candidates for Li battery applications.

4.4 Summary

A synthetic strategy has been successfully developed for preparing hollow carbon spheres, by hydrothermal treatment of α-CD in the presence of F127 as template and followed by pyrolysis. This new strategy makes use of the vesicle structures formed by block copolymer of PEO-PPO-PEO, threaded with α-CD onto PEO chains, dangling on the vesicle surface. The as-prepared hollow carbon spheres derived via the hydrothermal route are monodispersed and hydrophilically stable in aqueous environment, due to the surface decoration by PEO chain and other hydrophilic functional groups, such as carboxyl and hydroxyl groups. Upon pyrolysis at 900 ^{o}C in Ar, an all-carbon hollow spherical structure is developed. The size and carbon wall thickness of the hollow carbon spheres thus derived could well be controlled by adjusting the initial concentration of F127 in the aqueous phase. The meso-/microporous wall structure of the pyrolyzed hollow carbon spheres were demonstrated by their N_2 adsorption/desorption and CO_2 adsorption isotherms. The hollow carbon spheres exhibit a specific surface area of >300 m^2g^{-1} and they demonstrate a high specific charge capacity of >400 $mAhg^{-1}$ when employed as the anode in Li ion battery.

5 Hollow carbon spheres/manganese dioxide (MnO_2) nanohybrids

5.1 Background

For the past two decades, supercapacitors have received considerable attention, owing to their high power density, extremely long cycle life and fast charging-discharging rates, which are required by a wide spectrum of applications in load-leveling power sources, premium power systems, fast switches, consumer electronics, battery-power operations and military devices [244-246]. They are broadly grouped into two types, depending on the charge storage mechanisms, i.e., charge storage by electrical double layers and pseudocapacitance making use of the surface redox reaction of certain transitional metal oxides such as manganese dioxide (MnO_2) [247-249]. For both types of supercapacitors, various carbon-based materials have been used as electrodes, including for example active carbons, carbon aerogels, nanofoams, carbon nanotubes and more recently graphene [144-147, 246, 250-252]. Porous carbon-based materials are particularly interesting due to their relatively stable pore structure, high specific surface area, controllable pore size distribution, chemical stability and high electrical conductivity [253].

To improve the overall performance of supercapacitors, considerable efforts have been made with the development of carbon-transitional metal oxide nanocomposites, where the storage by electrical double layers is combined with the pseudocapacitance.

For this purpose, several transitional metal oxides that can undergo surface redox reactions, such as ruthenium oxide (RuO_2) and MnO_2, have been studied [254, 255]. Although the combination of non-Faradaic and Faradaic charge storages can in principle lead to much improved performance, the capacitance values reported so far for the carbon-transitional metal oxide nanocomposites is well below the theoretical prediction. It would therefore be of considerable interest to further investigate the nanohybrid structure consisting of porous carbon and transitional metal oxide spheres, by devising new synthetic process for them and understand their performance in supercapacitors.

In this chapter, a facile process is described for hollow carbon spheres containing MnO_2 nanocrystalline, which are investigated or supercapactance behavior. Indeed, MnO_2 is chosen for development of the wanted pseudocapacitance, by considering its high theoretical specific capacitance (1370 Fg^{-1}) and environmental friendliness [244]. MnO_2 nanocrystals are incorporated into the micro- and meso-carbon structures, which are similarly prepared in chapter 4, by the redox reaction between potassium permanganate ($KMnO_4$) and carbon surface in aqueous solution. By carefully controlling the processing parameters involved, the MnO_2 nanocrystals can be grown on both the external and internal surfaces of hollow carbon spheres, leading to a more electrochemically active electrode surface.

5.2 Experimental details

5.2.1 Materials

F127 is purchased from Sigma-Aldrich Company. α-CD is purchased from Tokyo Chemical Industry Company. $KMnO_4$ is purchased from Alfa Aesar Company.

5.2.2 Synthetic procedure of hollow carbon spheres /MnO_2 hybrids

The hollow carbon spheres were prepared according to the process described in chapter 4 with slight modifications. Firstly, 30 mg F127 was first dissolved in 20 mL deionized (DI) water. 60 mg of α-CD was then dissolved in 20 mL DI water. Upon complete dissolution of F127 and α-CD forming respective clear solutions, the α-CD solution was injected into the solution of F127 under stirring at 700 rpm. The mixed solution was stirred overnight and then transferred into a Teflon sealed autoclave tube. Upon the completion of hydrothermal treatment at 200 ^{o}C for 6 h, the clear solution turned into black in appearance. The black solution was then washed by DI water three times by centrifugation at 9000 rpm for 30 min. After washing, the black precipitates were re-dispersed in DI water and freeze dried for two days to obtain the carbon powder for further study. Finally, the dry powder of the as-prepared sample was further pyrolyzed in a tube furnace at 500 ^{o}C for 30 min under argon (Ar) gas protection, which was denoted as HCSA.

For incorporation of nanocrystalline MnO_2 into the hollow carbon spheres, i.e., on the surface of HCSA, the direct redox reaction of $KMnO_4$ on carbon surface was employed. Typically, 30 mg of HCSA was ultrasonically dispersed in 50 mL DI water. 90 mg $KMnO_4$ was then added into the HCSA dispersion. After stirring for an appropriate period of time, e.g., 5 min and 16 h, the mixed solution was heated to 70 ^{o}C. After refluxing at 70 ^{o}C for 180 min, the black precipitates were washed three times by centrifugation at 9000 rpm for 10 min. Finally, the product was collected after drying in vacuum oven at 60 ^{o}C for 48 h. The hybrid materials thus obtained were denoted as HCSA/MnO_2-5min and HCSA/MnO_2-16h to differentiate the difference in stirring time, i.e., 5 min and 16 h, respectively.

5.2.3 Characterization

Procedures for scanning electron microscopy (SEM), transmission electron microscopy (TEM), Raman, X-Ray diffraction (XRD) and X-ray photoelectron spectroscopy (XPS) were detailed in chapter 4. The elemental distribution in the sample was studied using a scanning TEM-energy dispersive X-ray spectroscopy (STEM-EDX; JEOL 2100). The loading of MnO_2 in hollow carbon spheres was determined by Inductively Coupled Plasma (ICP) Analysis using Perkin Elmer Dual-view Optima 5300 DV ICP-OES system.

5.2.4 Electrochemical performance

Electrochemical performance of the HCSA/MnO_2-5min and HCSA/MnO_2-16h as working electrodes in supercapacitor were investigated. The working electrode was fabricated by coating the viscous slurry of active materials (80 wt. %), carbon black (10 wt. %), and polytetrafluoroethylene (10 wt. %) in ethanol onto a nickel (Ni) foam of 4 cm^2 in area and 1 mm in thickness. After drying in a vacuum oven at 120 ^oC for 12 h, the coated Ni foam was uniaxially pressed under a pressure of 49 MPa to enhance the adhesion between the active materials and the Ni foam. The loading of active material on the Ni foam was determined to be 8.9 mg and 8.0 mg for HCSA/MnO_2-5min and HCSA/MnO_2-16h, respectively. A series of electrochemical parameters of the as-fabricated working electrode were tested, including the cyclic voltammetry (CV) and galvanostatic charge-discharge, using a three-electrode compartment on a Solartron Electrochemical System SI 1287. In the three-electrode system, aqueous sodium sulfate (Na_2SO_4) solution of 1.0 M in concentration, platinum (Pt) foil and silver/silver chloride (Ag/AgCl) electrode were used as the electrolyte, counter electrode and reference electrode, respectively. The electrolyte was purged with nitrogen (N_2) to remove oxygen (O_2).

5.3 Results and discussion

5.3.1 Structure of hollow carbon spheres/MnO_2 hybrids

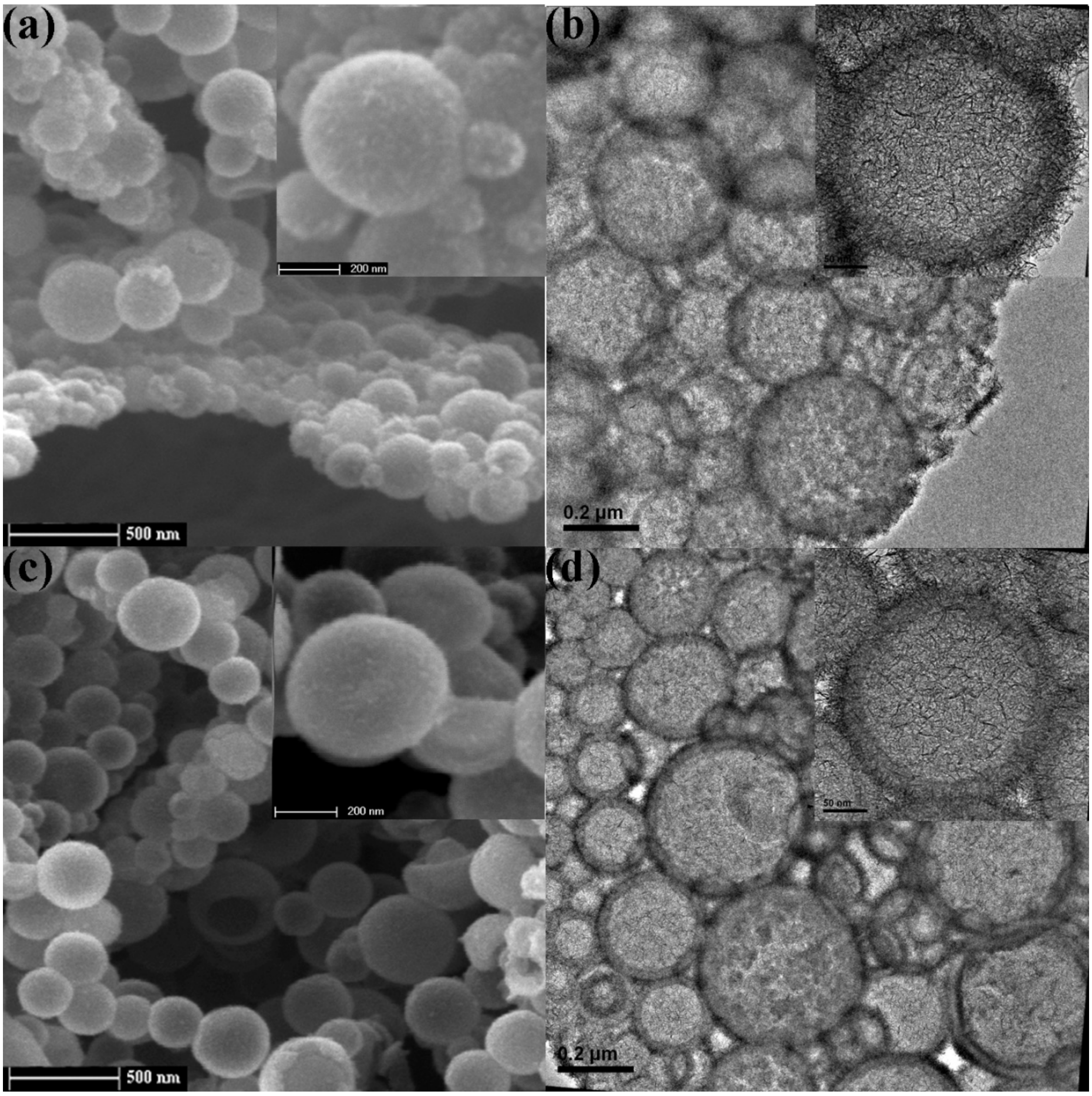

Figure 5.1 SEM and TEM images of HCSA/MnO_2-5min (a and b), and HCSA/MnO_2-16h (c and d), showing the hollow carbon spheres/MnO_2 hybrid structure.

By the direct redox reaction, nanocrystalline MnO_2 is grown on the surface of HCSA. In the reaction of $4MnO_4^{-}+3C+H_2O \rightarrow 4MnO_2+CO_3^{2-}+2HCO^{3-}$, HCSA acts as both a reduction agent and substrate to support MnO_2 nanocrystallites [256]. As shown by the SEM and TEM images (Figure 5.1) for HCSA/MnO_2 nanohybrids, nanocrystalline MnO_2 is formed and is distributed rather uniformly on the surface of the hollow carbon structure. The hollow carbon morphology is well retained, which indicates that the formation and growth of MnO_2 nanocrystallites have not destroyed the hollow carbon structure. The hollow sphere structure of carbon is further confirmed by the results of STEM-EDX element mapping, which are shown in Figure 5.2 and 5.3.

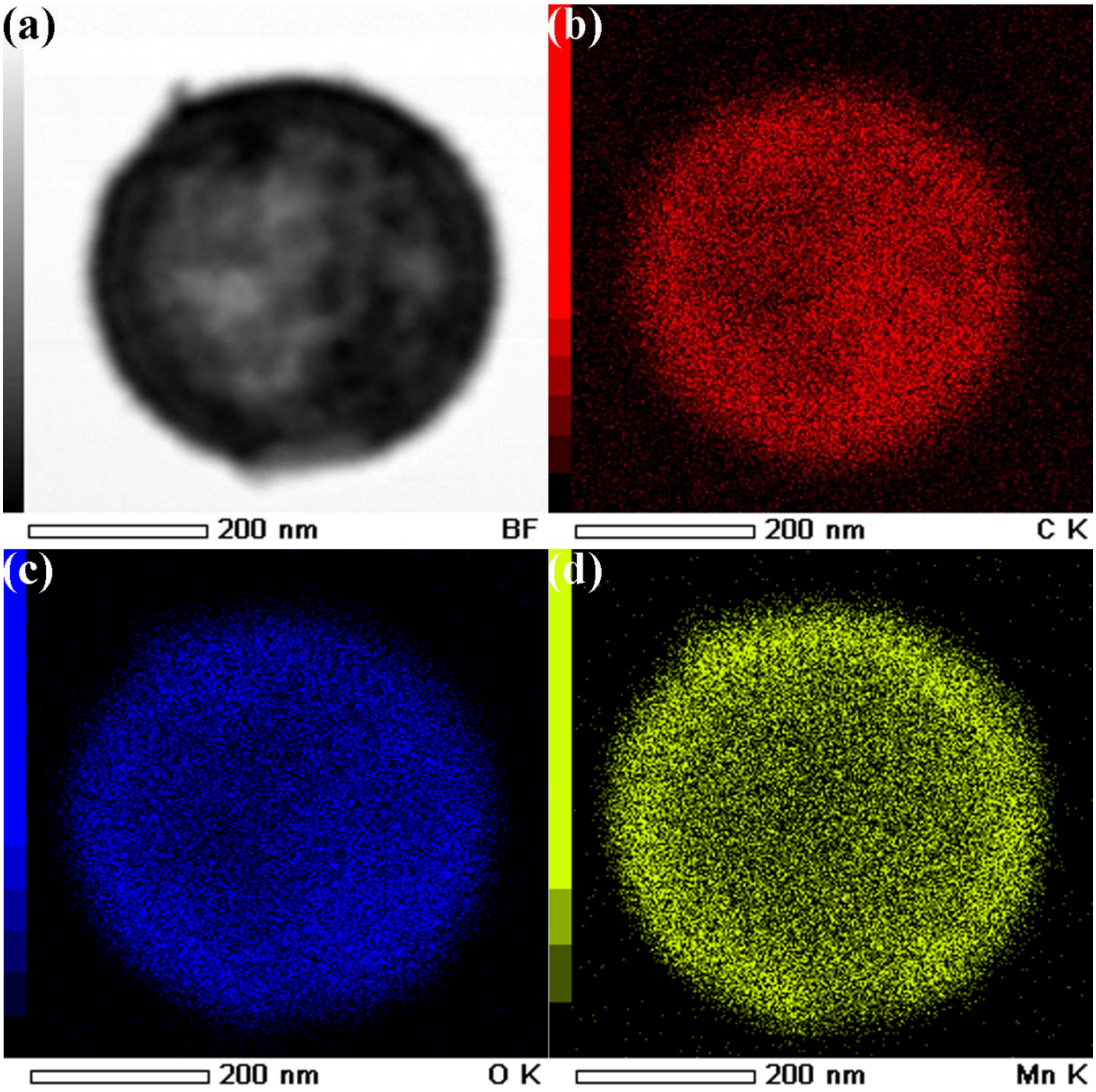

Figure 5.2 STEM-EDX element mapping result of HCSA/MnO_2-5min. The red, blue and yellow color represents C, O and Mn element, respectively.

It is clearly shown by the comparison between the bright field images, Figure 5.2 a and Figure 5.3 a, and the carbon element mapping images, Figure 5.2 b and Figure 5.3 b. Furthermore, there is also a visible difference between the two HCSA/MnO_2 samples derived from different treatment durations, denoted as HCSA/MnO_2-5min and HCSA/MnO_2-16h respectively.

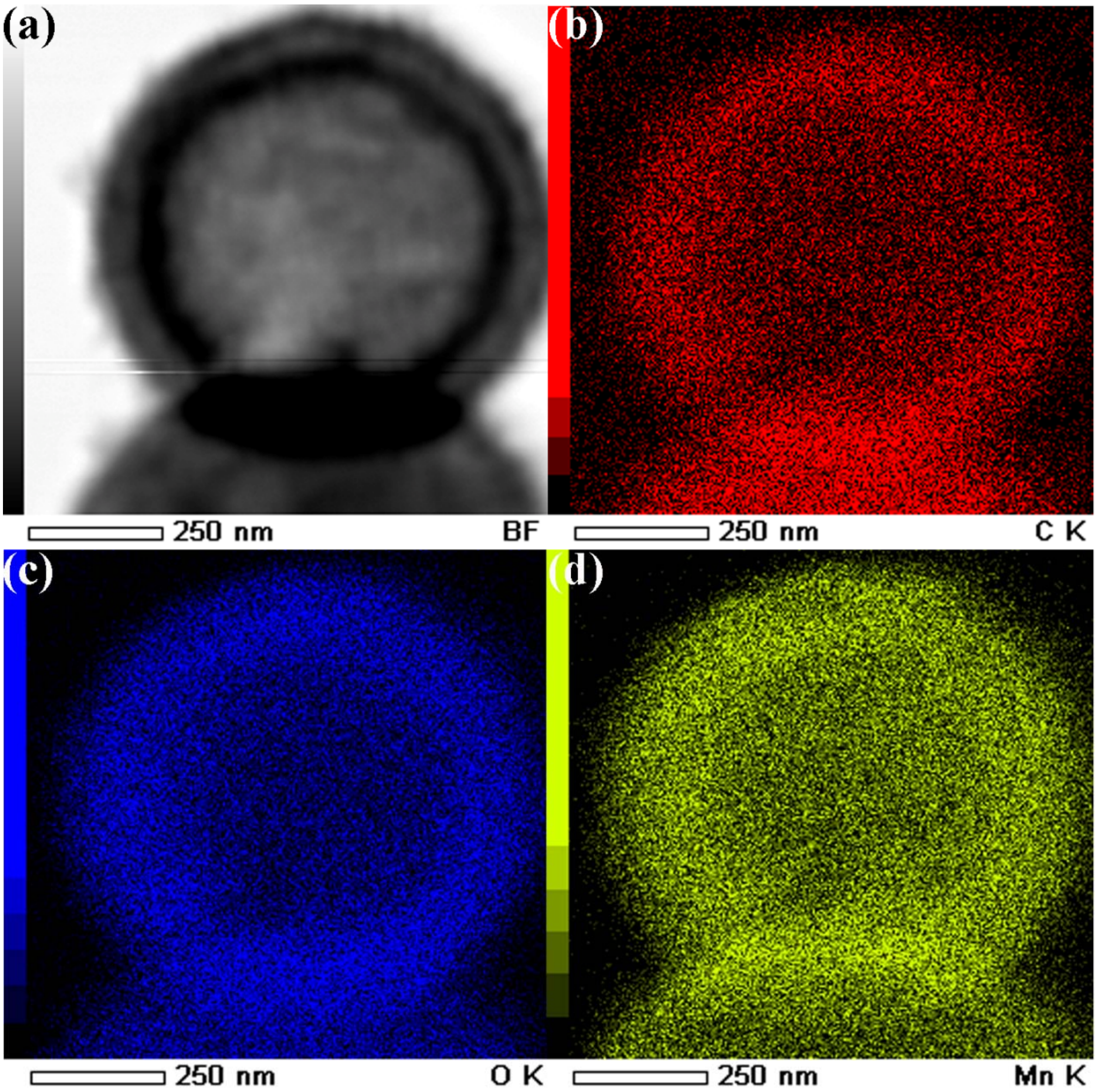

Figure 5.3 STEM-EDX element mapping result of HCSA/MnO_2-16h. The red, blue and yellow color represents C, O and Mn element, respectively.

According to the TEM image of HCSA/MnO_2-5min shown in Figure 5.1 b, nanocrystalline MnO_2 largely occurs on the external surface of HCSA, which is further indicated by the STEM-EDX element mapping of manganese (Mn; Figure 5.2 d). In contrast, for HCSA/MnO_2-16h shown in Figure 5.1 d, nanocrystallites of MnO_2 appear to occur on both the external and internal surfaces of HCSA, where there is a double layer structure for MnO_2. As further shown in Figure 5.3 d, Mn appears on both the external and internal carbon shell surfaces of HCSA/MnO_2-16h.

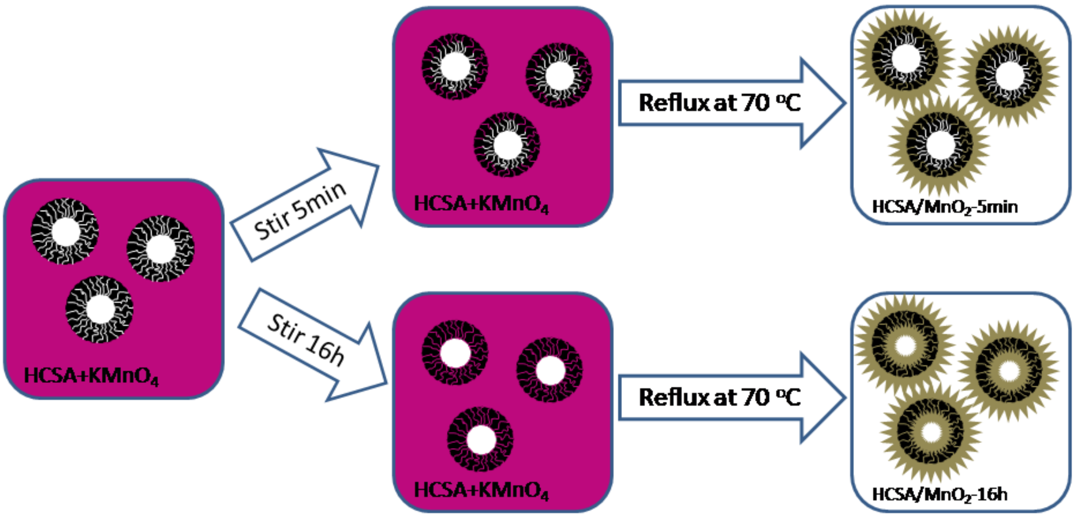

Figure 5.4 Schematic illustration for the formation of HCSA/MnO_2-5min and HCSA/MnO_2-16h.

As discussed in chapter 4, the as-prepared HCSA exhibits meso-/microporous across the carbon wall. As a result, upon the dispersion of HCSA into aqueous solution of $KMnO_4$, permanganate (MnO_4^-) can slowly diffuse into the interior of HCSA through the pores in the carbon wall of the hollow structure. As shown in Figure 5.4, when the mixed solution is stirred for 5 min, a rather limited amount of MnO_4^- is diffused into the inside of the hollow structure. Subsequent refluxing process leads to the formation MnO_2 on the external surface of hollow carbon spheres from MnO_4^- by the redox reaction. In contrast, when the mixed solution is stirred for an extended duration of 16 h, considerable amount of MnO_4^- is able to diffuse into the inside of the hollow structure. The subsequent conversion of MnO_4^- to MnO_2 by redox reaction on the internal surface of carbon wall under the refluxing process generated the double layer structure, where there are nanocrystalline MnO_2 distributed on both the external and internal surfaces of HCSA. Since the MnO_2 on the internal surfaces of HCSA is generated by the diffusion of MnO_4^- through the pores in the carbon wall, the controlling is not quite accurate, which makes some particles in Figure 5.1 b and Figure 5.1 d look similar.

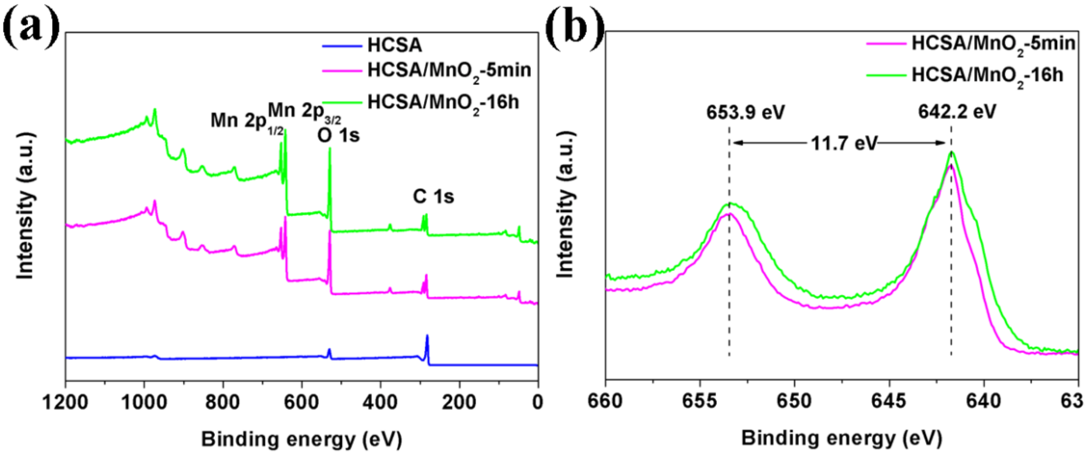

Figure 5.5 XPS survey (a) and Mn 2p (b) spectra of HCSA, HCSA/MnO_2-5min and HCSA/MnO_2-16h.

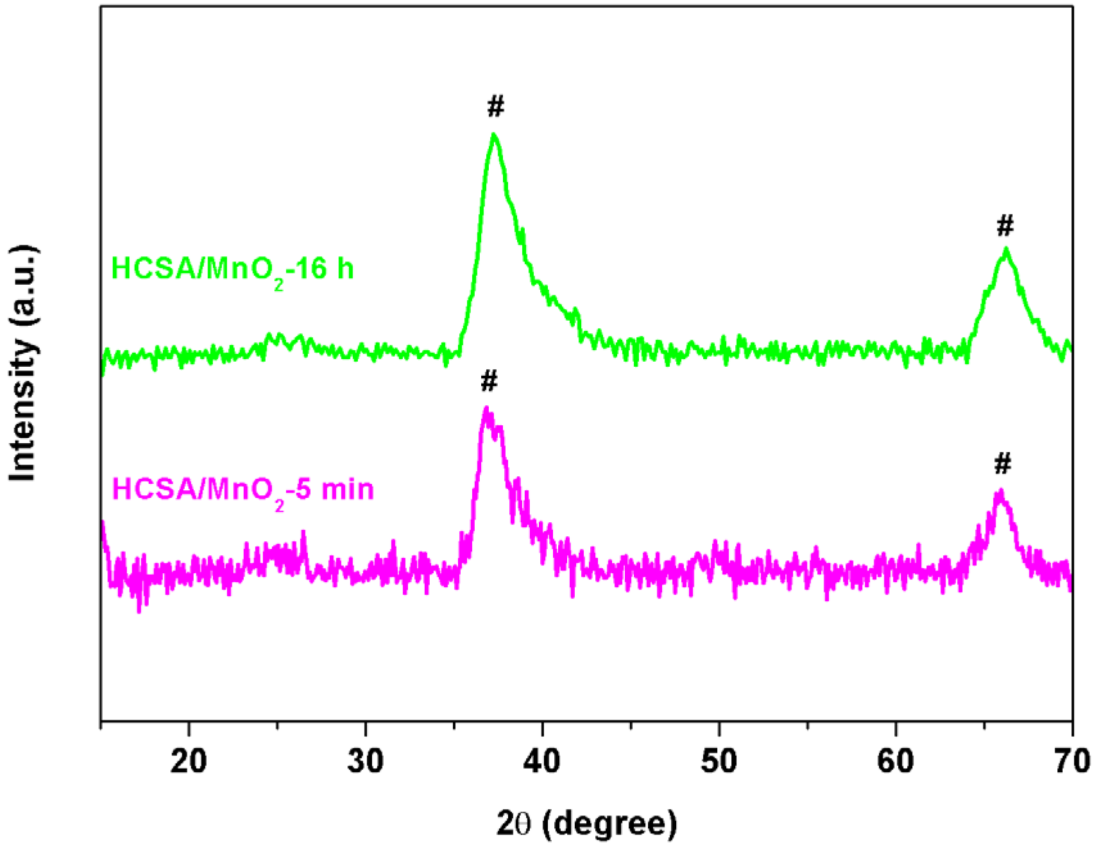

Figure 5.6 XRD traces of HCSA/MnO_2-5min and HCSA/MnO_2-16h.

ICP analysis shows that the loading of MnO_2 in HCSA is 25.50 wt. % and 27.42 wt. % for HCSA/MnO_2-5min and HCSA/MnO_2-16h, respectively. The presence of nanocrystalline MnO_2 on the surface of HCSA is also confirmed by XPS survey spectrum, which is shown in Figure 5.5. As shown in Figure 5.5 b for Mn 2p spectra, the spin-orbit peaks of MnO_2 correspond to Mn $2p_{2/3}$ and Mn $2p_{1/2}$, which occur at 653.9 and 642.2 eV, respectively [257].

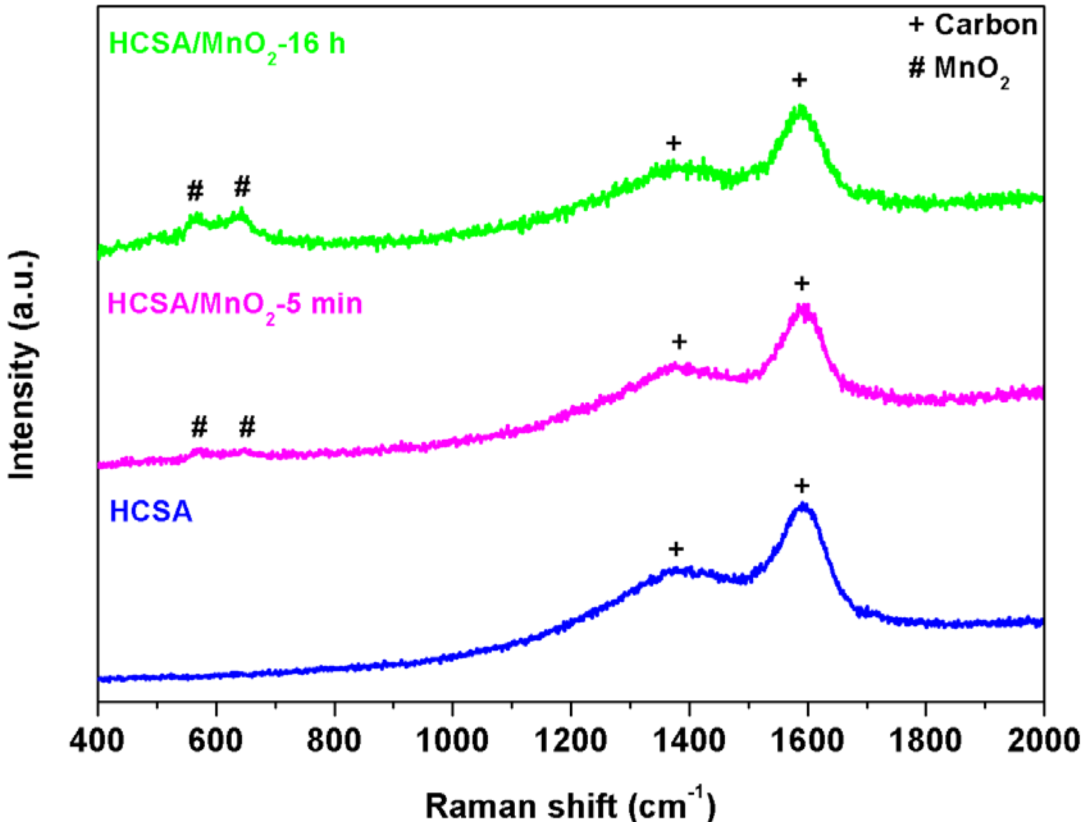

Figure 5.7 Raman spectra of HCSA/MnO_2-5min, HCSA/MnO_2-16h and HCSA.

To further confirm the nanocrystalline structure of MnO_2, XRD and Raman spectra are acquired. From the XRD spectra of HCSA/MnO_2-5min and HCSA/MnO_2-16h, which are shown in Figure 5.6, the crystalline phase of MnO_2 is identified to be α crystallographic form, as confirmed by the peaks at $2\theta = 37^o$ and 66^o, corresponding to the (211) and (002) reflections, respectively (# labeled in Figure 5.6) [258]. Moreover, the Raman spectra of HCSA/MnO_2-5min, HCSA/MnO_2-16h and HCSA in Figure 5.7, all show the typical spectra for carbon materials, exemplified by the peaks at 1346 cm^{-1} and 1556 cm^{-1} (+ labeled in Figure 5.7) [194, 224]. As shown in Figure 5.7, the broad peak at 1346 cm^{-1}, is assigned to D band, which is associated with the benzene ring-breathing vibrations [194, 224]. The peak at 1556 cm^{-1} appears to match well with the G band, which is a band related to the in-plane bond-stretching motion of the C *sp*^{2} atoms pairs [194, 224]. Furthermore, the α phase of MnO_2 is confirmed by the characteristic bands in the low Raman shift region, which peak at 573 and 640 cm^{-1}, respectively (# labeled in Figure 5.7) [180, 259]. In the MnO_6 groups, the Mn-O stretching vibration band within the basal plane is represented by 573 cm^{-1} Raman shift, while the symmetric Mn-O stretching vibration band is related to 640 cm^{-1} Raman shift [260]. Therefore both XRD and Raman spectra confirm that the nanocrystalline MnO_2 phase formed on the surface of HCSA is of α phase.

5.3.2 Supercapacitive behavior

Based on the above hollow spherical structure discussed for HCSA/MnO_2 hybrids, it would be of interest to study their performance as a working electrode in supercapacitor, where the pseudocapacitive MnO_2 is combined into porous carbon substrate [180]. Their electrochemical performances as working electrodes in supercapacitor are studied by using a three-electrode configuration, which is illustration in Figure 5.8. As shown in Figure 5.9 a and b, the CV curves of both supercapacitor working electrodes, made of HCSA/MnO_2-5min and HCSA/MnO_2-16h respectively, exhibit quasi-rectangular shapes in the potential window of 0-1.0 V at a variation of scan rates from 1 to 100 mVs^{-1}, which demonstrate the excellent reversibility of the supercapacitor working electrodes [261].

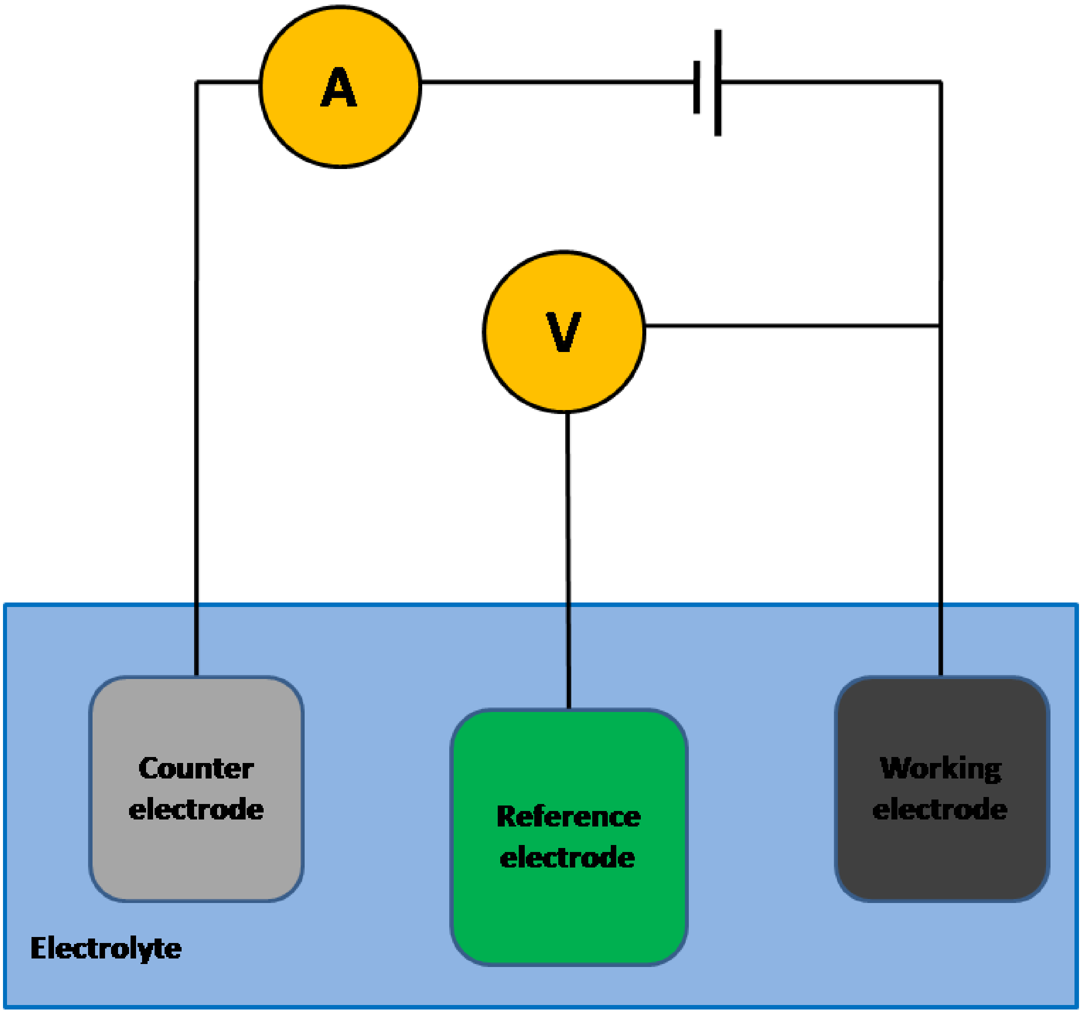

Figure 5.8 Schematic illustration of three-electrode configuration, where the working electrode is fabricated by the testing samples and applied the desired potential, the counter electrode is passed by the needed current to balance the current applied at the working electrode and the reference electrode acts in measuring and controlling the potential on working electrode with a reference value.

The MnO_2 nanocrystallites assembled on the surface of HCSA are expected to give rise to pseudocapacitive behavior. A careful comparison between Figure 5.9 a and b shows that the supercapacitor working electrode made of HCSA/MnO_2-16h exhibits a higher current density than that of HCSA/MnO_2-5min, suggesting that the former exhibits a higher specific capacitance. At a current density of 0.1 Ag^{-1}, rather linear shape and symmetric behavior are observed in the galvanostatic charge-discharge profiles, as shown in Figure 5.9 c, further demonstrating that the HCSA/MnO_2

hybrids exhibit a desired capacitive behavior and excellent electrochemical reversibility of Faradic reaction between sodium ion (Na^+) in the electrolyte and nanocrystalline MnO_2 on the carbon surface [180].

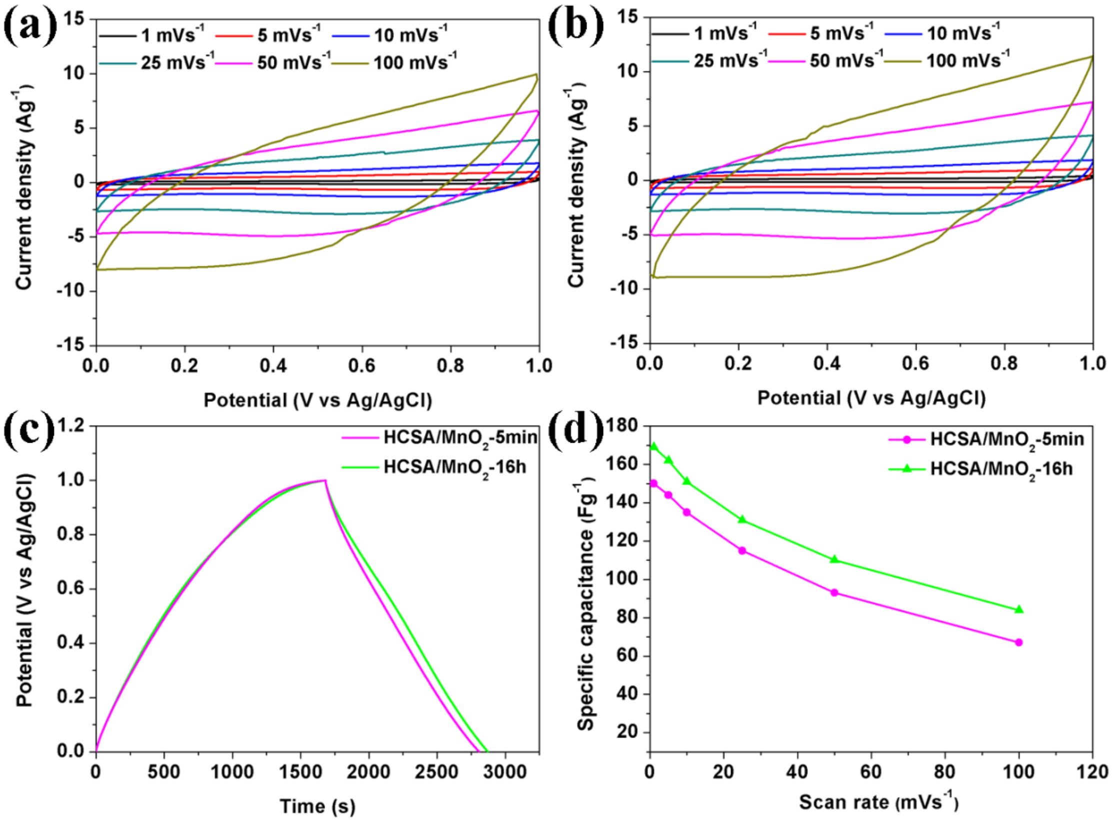

Figure 5.9 Electrochemical behavior of the supercapacitor working electrode made of HCSA/MnO_2 hybrid. (a) CV curves of the supercapacitor working electrode made of HCSA/MnO_2-5min; (b) CV curves of the supercapacitor working electrode made of HCSA/MnO_2-16h; (c) galvanostatic charge-discharge of the supercapacitor working electrodes at a current density of 0.1 Ag^{-1}; (d) variation in specific capacitance for the supercapacitor working electrodes against different scan rates.

Although there is no difference in crystalline, morphology of the MnO_2 nanocrystals between the HCSA-5min and HCSA-16h, there are MnO_2 nanocrystallites assembled on both the external and internal surfaces of carbon wall in HCSA/MnO_2-16h, while there is MnO_2 only on the external surface for HCSA/MnO_2-5min. Such difference in structure leads to the apparent change in supercapacitor performance. Their behavior in charge storage is further confirmed by the specific capacitance value calculated for various scan rates.

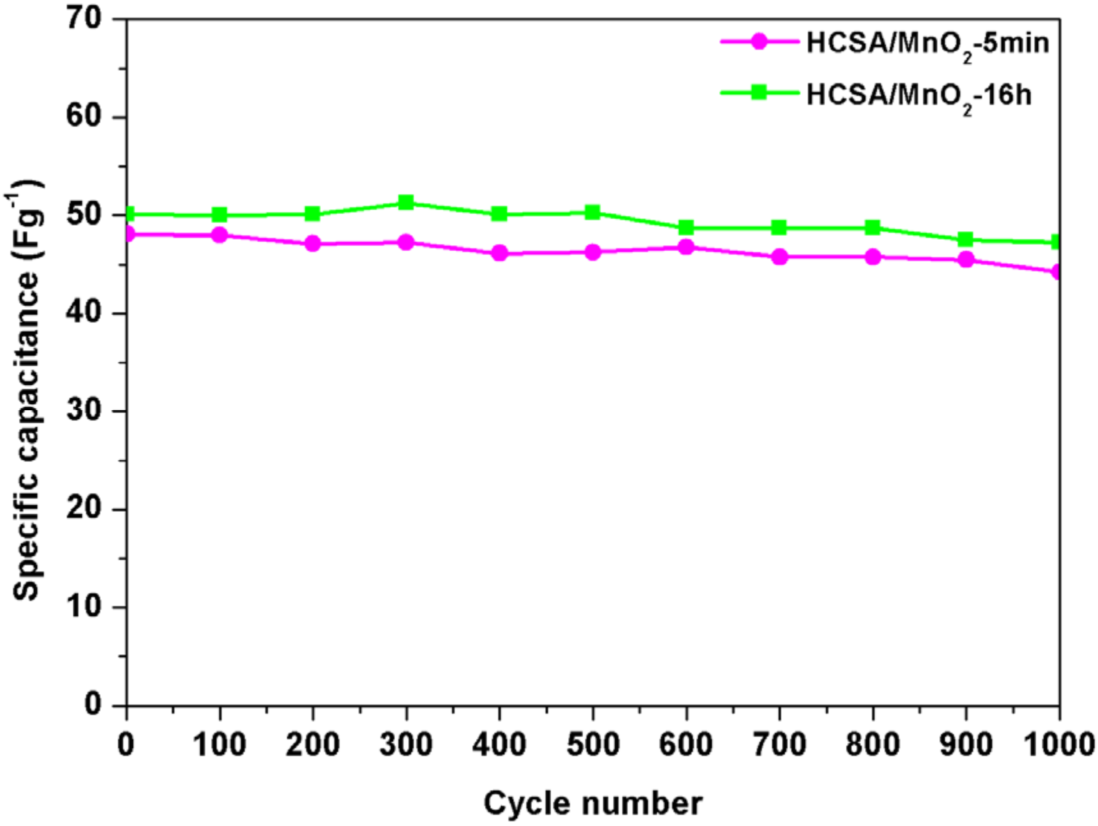

Figure 5.10 Cycle life of the working electrode made of HCSA/MnO_2-5min and HCSA/MnO_2-16h. The operation voltage is 1.0 V and the current density is 2.0 A g^{-1}.

As shown in Figure 5.9 d, the specific capacitance of HCSA/MnO_2-16h is higher than HCSA/MnO_2-5min at each scan rate, which is apparently due to the more electrochemically active surface provided by the double MnO_2 layers on the carbon shell. At low scan rates, e.g. 1 mVs^{-1}, the specific capacitances are ~150 and ~170 Fg^{-1} for HCSA/MnO_2-5min and HCSA/MnO_2-16h, respectively, which are comparable to those previously reported for MnO_2 based supercapacitor electrodes [262]. However, the lower than expected specific capacitance may well be due to the overall low electrical conductivity. The hollow carbon spheres consist of largely amorphous carbon. The MnO_2 is known to exhibit rather low electrical conductivity, which cover the carbon surface, and therefore the overall conductivity will be low for the hollow carbon spheres/MnO_2 hybrid. Another consideration is the relatively poor stability of MnO_2, which can undergo dissolution in the electrolyte. Due to the shortening in Na^+ diffusion distance into MnO_2 at high scan rates, the specific capacitance decreases with the scan rate [263, 264]. However, the possible solution for the capacitance loss of MnO_2 is further coating the hybrid surface by using graphene or conduction polymer, which will not only give rise to the protection of MnO_2, but also leads to a better conductivity property. The capacitance loss is 50.3% for the electrode made of HCSA/MnO_2-16h, while it is 55.3% for the electrode made of HCSA/MnO_2-5min. As shown in Figure 5.10, the specific capacitance for HCSA/MnO_2-5min and HCSA/MNO_2-16h could retain 91% and 94% after 1000 cycles of measurement within the operation voltage of 1.0 V under the current density of 2.0 Ag^{-1}, respectively. This again shows that the double MnO_2 layers in the hollow sphere structure leads to a slightly better rate capability.

5.4 Summary

A new synthetic strategy has been developed for synthesizing hollow carbon spheres/MnO_2 nanohybrids, where hollow carbon spheres, which exhibit a meso-/microporous carbon wall, are demonstrated to be an excellent substrate for growth of MnO_2 nanocrystallites on their surface by the redox reaction between carbon and MnO_4^-. The porous structure of carbon wall allows MnO_4^- ions to diffuse though, which offers the opportunity for developing a double layer nanohybrid structure consisting of nanocarbon and MnO_2. The electrochemical performances of the hollow carbon spheres/MnO_2 nanohybrid in supercapacitor are evaluated. By comparison, the double layer structure of nanocrystalline MnO_2 assembled on both the external and internal surfaces of hollow carbon spheres (HCSA/MnO_2-16h) shows a better performance than that of the supercapacitor working electrode made of hollow carbon with MnO_2 deposited on the external surface.

6 Cobalt monoxide (CoO)-doped graphitic porous carbon microspheres

6.1 Background

In recent years, supercapacitors have been extensively investigated for energy storage, in attempts to improve their energy density and overall performance [244, 246, 253]. To develop electrode materials with high surface specific area and controlled porosity for electric double layer supercapacitors (EDLS), carbon-based materials, such as activated carbon, carbon nanotubes, graphene, carbon film and mesoporous carbon, have been investigated [4, 265-269]. They are among the most promising materials owing to their desirable physical and chemical behavior and processing ability, including tunable morphologies, controllable porosity, relatively inert surface electrochemistry, high electrical conductivity and low manufacturing cost [4, 265-270]. Since there is no electrochemical reaction between the electrode of carbon and electrolyte, the performance of EDLS is mainly dependent on the available surface area, pore size distribution, connectivity and electrical conductivity [271]. In contrast, pseudo-supercapacitors are the other type of supercapacitors, which are on the basis of the fast and reversible faradaic reactions between electrode materials and electrolytes [272]. There is faradaic current across the supercapacitor cell during the reversal processes of charging and discharging, which not only increases the specific capacitance but also extends the operation voltage of the supercapacitor [273]. Thus, transition metal (e.g., ruthenium (Ru), manganese (Mn), vanadium (V), tin (Sn), iron (Fe), nickel (Ni) and cobalt (Co)) oxides and hydroxides with pseudo-capacitive behavior are of great interest for the application as electrode materials in pseudo-supercapacitors [274-284]. The main challenges are still the low energy density and poor overall performance, which have to be tackled in order to widen the applications of supercapacitors [244, 246, 253, 285]. In order to improve the desperately wanted energy density, an effective approach is to increase the capacitance and operation voltage, since the energy density (E) is in theory related to both parameters, $E = 0.5CV^2$, where C (in farads) and V (in volts) are the capacitance and operation voltage, respectively [253, 286]. Therefore, electrode materials with the desirable physical and electrochemical performances are the key factors in leading to high energy density for supercapacitors [287]. In particular, it would be of interest to effectively combine the double-layer capacitance and pseudo-capacitance by developing a nanohybrid type of electrode materials, where electric double-layers and faradaic capacitance can be realized concurrently to match the requirement of high energy density and better overall performance [288].

In this chapter, a novel design and facile synthetic process is presented for a carbon-based nanohybrid material, i.e., cobalt monoxide (CoO)-doped graphitic porous carbon microspheres (Co-GPCMs), which is studied as a promising electrode material in supercapacitors showing high energy density. As shown in Figure 6.1, the designed carbon microspheres contain both micropores (1-2 nm) and mesopores (5-50 nm), where the carbon wall exhibits the graphitic structure. For energy storage by

EDLS, the porous structure of carbon microspheres would provide the wanted interfaces for electrostatic charge accumulation, while the graphitic carbon wall could enhance the electric conductivity [85]. Moreover, CoO as a transitional metal oxide offers the potential of pseudo-supercapacitors [284].

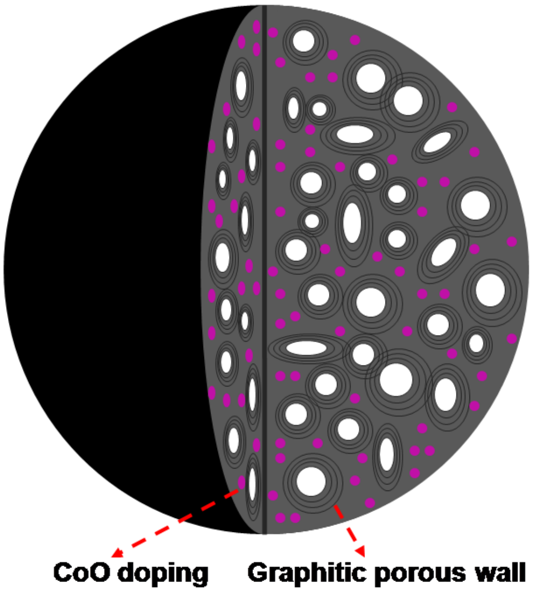

Figure 6.1 Schematic illustration of the designed structure of Co-GPCMs in this chapter.

The hybrid electrode is expected to be electrochemically active, enabling the reaction with the electrolyte by fast and reversible faradaic reactions to enhance the operation voltage [289]. This would effectively combine the EDLS of carbon and pseudo-supercapacitors of CoO, leading to an improvement in energy density. The designed Co-GPCMs are prepared by a new synthetic process, conducted under a controlled hydrothermal condition, where the mixture of cobalt gluconate (Co-gluconate), α-cyclodextrin (α-CD) and poly (ethylene oxide)$_{106}$-poly (propylene oxide)$_{70}$-poly (ethylene oxide)$_{106}$ (F127) is treated hydrothermally, followed by pyrolysis process in argon (Ar) gas. As detailed in the results and discussions below, the resultant Co-GPCMs is demonstrated promising as an electrode material in supercapacitors.

6.2 Experimental details

6.2.1 Materials

Co-gluconate and F127 are purchased from Sigma-Aldrich Company. α-CD is purchased from Tokyo Chemical Industry Company.

6.2.2 Synthetic procedure of Co-GPCMs

Co-GPCMs were synthesized via hydrothermal treatment route followed by pyrolysis. Firstly, 300 mg F127 was dissolved in 20 mL deionized (DI) water. 49 mg of Co-gluconate dissolved in 10 mL DI water was then injected into the solution of F127 under stirring at 700 rpm. After that, 600 mg of α-CD dissolved in 10 mL DI water was injected into the mixed solution of F127 and Co-gluconate under stirring at 700 rpm. The mixed solution was further stirred overnight and then transferred into a Teflon sealed autoclave tube. Upon hydrothermal treatment at 200 ^{o}C for 6 h, the clear solution turned into black in appearance. The black product was then collected by centrifugation at 9000 rpm for 30 min, and then washed by DI water three times. After washing, the black precipitates were re-dispersed in DI water and freeze dried for two days to obtain the black powder. Finally, the dried powder was further pyrolyzed in a tube furnace at 900 ^{o}C for 3 hours under Ar gas protection.

6.2.3 Characterization

The morphology and phase structure of the products were studied by using scanning electron microscopy (SEM; ZEISS SUPRA 40) and transmission electron microscopy (TEM; CM 300 FEG-Philips). To study their fracture surface, the as-synthesized Co-GPCMs powders were frozen by liquid nitrogen (N_2) and grinded to get fracture surface. Procedures for Raman, X-Ray diffraction (XRD), scanning TEM-energy dispersive X-ray spectroscopy (STEM-EDX) line analysis and elemental mapping were described in chapter 5. N_2 adsorption and desorption isotherms and surface area determination were conducted by following the same procedure in chapter 4. The amount of CoO in Co0GPCMs was determined by the same equipment and procedure in chapter 5.

6.2.4 Electrochemical performance

Electrochemical performances of the Co-GPCMs as supercapacitor working electrode were investigated using a Solartron Electrochemical System SI 1287. The working electrode was fabricated by coating the viscous slurry of Co-GPCMs (80 wt. %), carbon black (10 wt. %), and polytetrafluoroethylene (10 wt. %) in ethanol onto a Ni foam of 2.25 cm^2 in area and 1 mm in thickness. After drying in a vacuum oven at 120 ^oC for 12 h, the coated Ni foam was uniaxially pressed at a pressure of 49 MPa to enhance the adhesion between the active materials (18.7 mg) and the Ni foam. A series of electrochemical tests were made with the working electrode , including the cyclic voltammetry (CV) and galvanostatic charge-discharge by using 6 M potassium hydroxide (KOH) aqueous solution as the electrolyte, which was purged with N_2, within the operation voltage of -1.2-0, 0-0.4 and -1.2-0.4 V. In the three electrode system, platinum (Pt) foil and silver/silver chloride (Ag/AgCl) were used as the counter and reference electrode, respectively.

6.3 Results and discussion

6.3.1 Structure of Co-GPCMS

SEM and TEM images of the microspheres derived from the hydrothermal treatment of Co-gluconate and α-CD in the presence of F127 are shown in Figure 6.2 a and b, where one can see their morphologies and inner structures. The hydrothermal treatment of Co-gluconate and α-CD in the presence of F127 at 200 ^{o}C for 6 h lead to a spherical structure with average size of 1464 nm. In addition, from the TEM image shown in Figure 6.2 b, the carbon microspheres are solid without cavity inside the carbon frame. In contrast, upon pyrolysis treatment of the as-prepared carbon microspheres in Ar gas at 900 ^{o}C for 3 h, a graphitic porous carbon structure is established for Co-GPCMs, as shown in Figure 6.2 c and d. From the SEM image in Figure 6.2 c, the Co-GPCMs are spherical in morphology with an average size of ~1200 nm. Moreover, the surface of these Co-GPCMs appears rough, which is apparently due to the decomposition of F127 under pyrolysis. Indeed the decomposition of F127 by pyrolysis treatment is confirmed by the shrinkage in the average microsphere size. As a result, upon pyrolysis, there is a visible porous structure established in the carbon frame, which is further confirmed by SEM and

TEM images showing their fracture surface (inset in Figure 6.2 c and d). In addition, the TEM image shown in Figure 6.3 a confirms the presence of pores of varying sizes inside the Co-GPCMs.

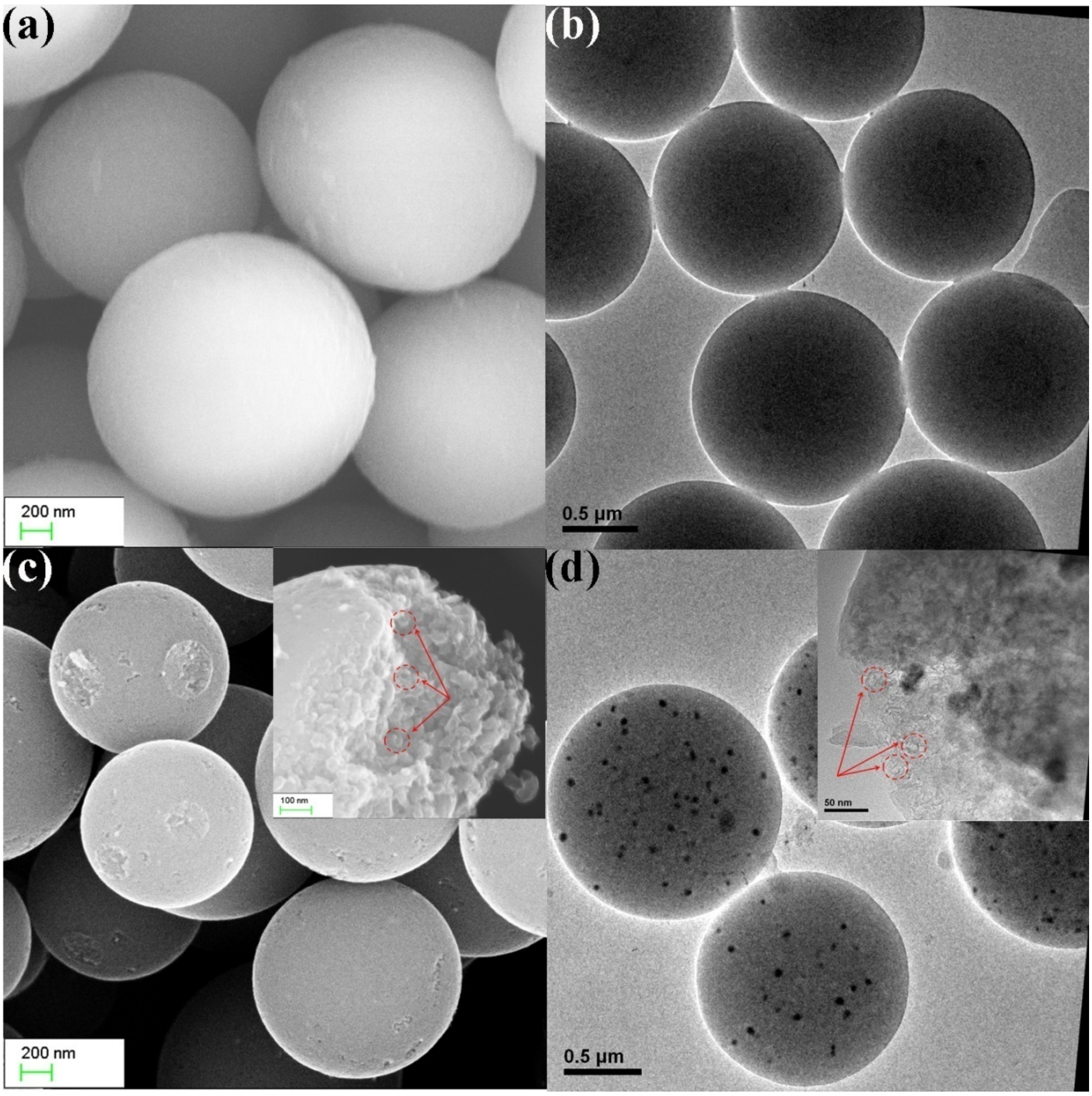

Figure 6.2 SEM (a), and TEM (b) images of the carbon microspheres synthesized by hydrothermal treatment of Co-gluconate and α-CD together in the presence of F127. SEM (c) and TEM (d) images of Co-GPCMs after pyrolysis treatment, where their fracture surfaces are shown in inset of (c) and (d).

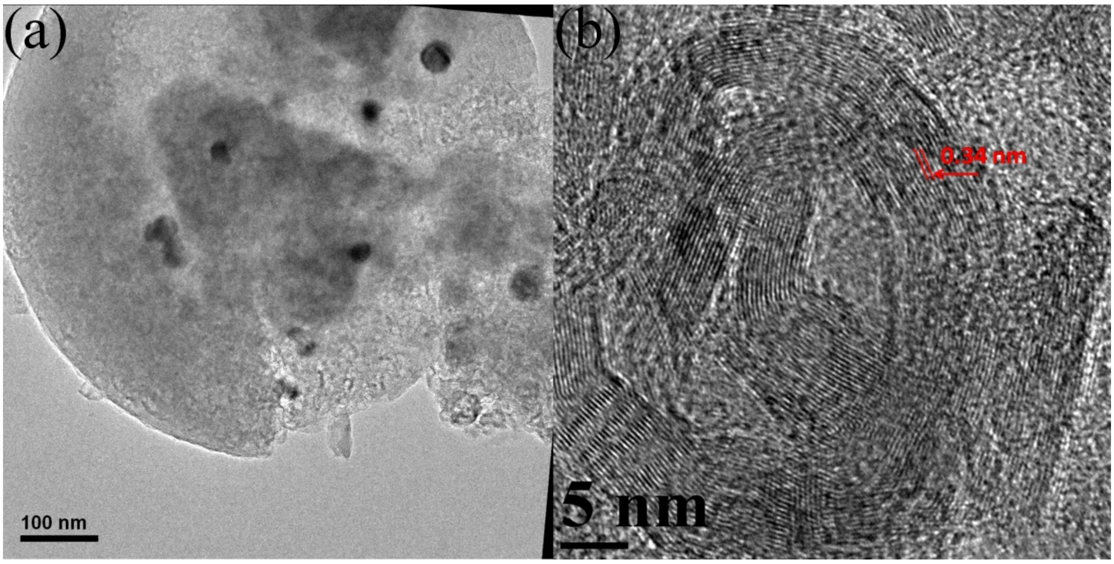

Figure 6.3 TEM image (a) and high resolution TEM image (b) of the fracture section of Co-GPCMs.

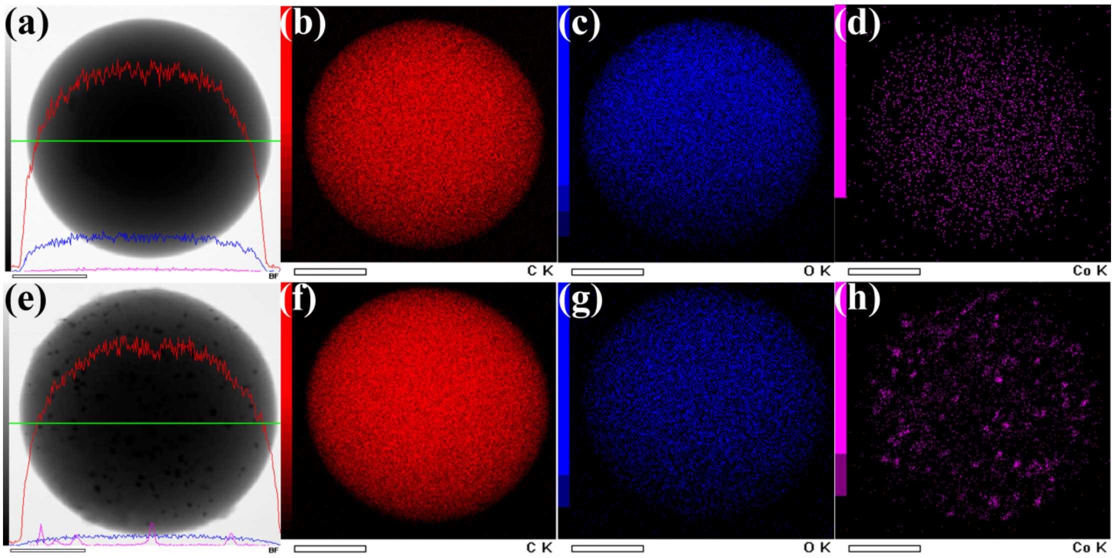

Figure 6.4 STEM-EDX line analysis of individual carbon microspheres synthesized by hydrothermal treatment of Co-gluconate and α-CD together with F127 (a), and the corresponding element mapping result (b-d). STEM-EDX line analysis of individual carbon microspheres of Co-GPCMs (e) and the corresponding element mapping result (f-h). The red, blue and purple color represents C, O and Co element, respectively. The scale bar is 500 nm.

As shown in Figure 6.3 b, which is a high resolution TEM image of the fracture section of an individual sphere of Co-GPCMs, they appear to consist of crystallized carbon, which is in close match with the (002) lattice spacing of disordered graphite [67]. In addition, as shown in Figure 6.2 d, the black dots embedded in the carbon spheres are Co in composition, which is further confirmed by STEM-EDX line analysis and element mapping result as shown in Figure 6.4.

As shown in Figure 6.4, the carbon microspheres contain rather uniformly distributed Co element, as confirmed by the STEM-EDX line analysis (Figure 6.4 a) and the corresponding Co element mapping (Figure 6.4 d). At the hydrothermal temperature of 200 ^{o}C, α-CD is converted to carbon while the dissolved Co salt is wrapped in the carbon matrix, which is assisted by the hydrogen bonding between Co-gluconate with α-CD and F127 [290]. Since Co-gluconate is an inorganic slat, which would be converted to Co-based nanodots at the high temperature pyrolysis treatment, Co is known to play a key function of acting as a catalyst for forming graphitic carbon [291]. In addition, the absence of cavity in the final carbon microspheres by Co-gluconate addition is due to destroy of the vesicle structure formed by α-CD and F127, since Co-gluconate is a kind of salt, which can destroy the hydrophobic/hydrophilic balances between PPO block in F127 and PEO/α-CD segment as described in chapter 4. The conversion of Co-gluconate to Co-based nanodots distributed in the Co-GPCMs is confirmed by the STEM-EDX line analysis (Figure 6.4 e) and the corresponding Co element mapping (Figure 6.4 h). To further understand the crystal structure and porous distribution in Co-GPCMs, XRD, Raman spectrum and BET analysis are conducted.

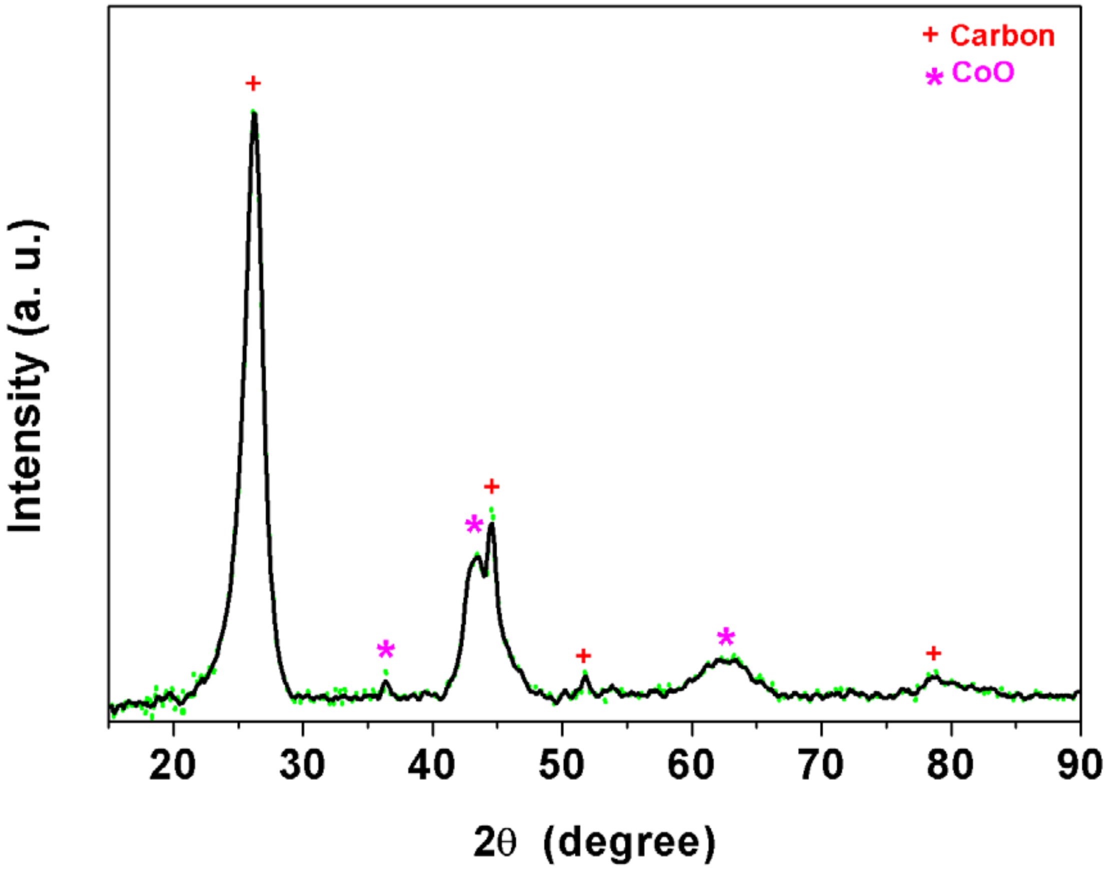

Figure 6.5 XRD trace of Co-GPCMs.

From XRD phase analysis, which is shown in Figure 6.5, crystallites of both carbon and Co-based nanodots in Co-GPCMs can be identified. Obviously, there is a typical characteristic XRD pattern of graphitic carbon (labeled by + in Figure 6.5), which exhibits peaks at 2θ of 26°, 44°, 54° and 77°. These peaks are assigned to the (002), (101), (004) and (110) planes of the graphitic carbon frame, respectively (JCPDS file number 41-1487) [292]. In addition, the presence of the sharp (002) diffraction peak indicates that the Co-GPCMs exhibits a highly ordered graphitic structure, which corresponds well to the result of TEM studies in Figure 6.3 [292]. The crystalline phase of Co-based nanodots is indentified by the XRD peaks (labeled by * in Figure 6.5) at 2θ of 37°, 42° and 62°, which represent the (111), (200) and (220) diffractions of CoO (JCPDS file number 43-1004) [293]. The amount of CoO retained in Co-GPCMs is measured to be 4.2 wt. % by ICP analysis. Since there is a rather small amount of CoO in the Co-GPCMs, the presence of CoO nanodots is not as obvious as that of the graphitic carbon frame.

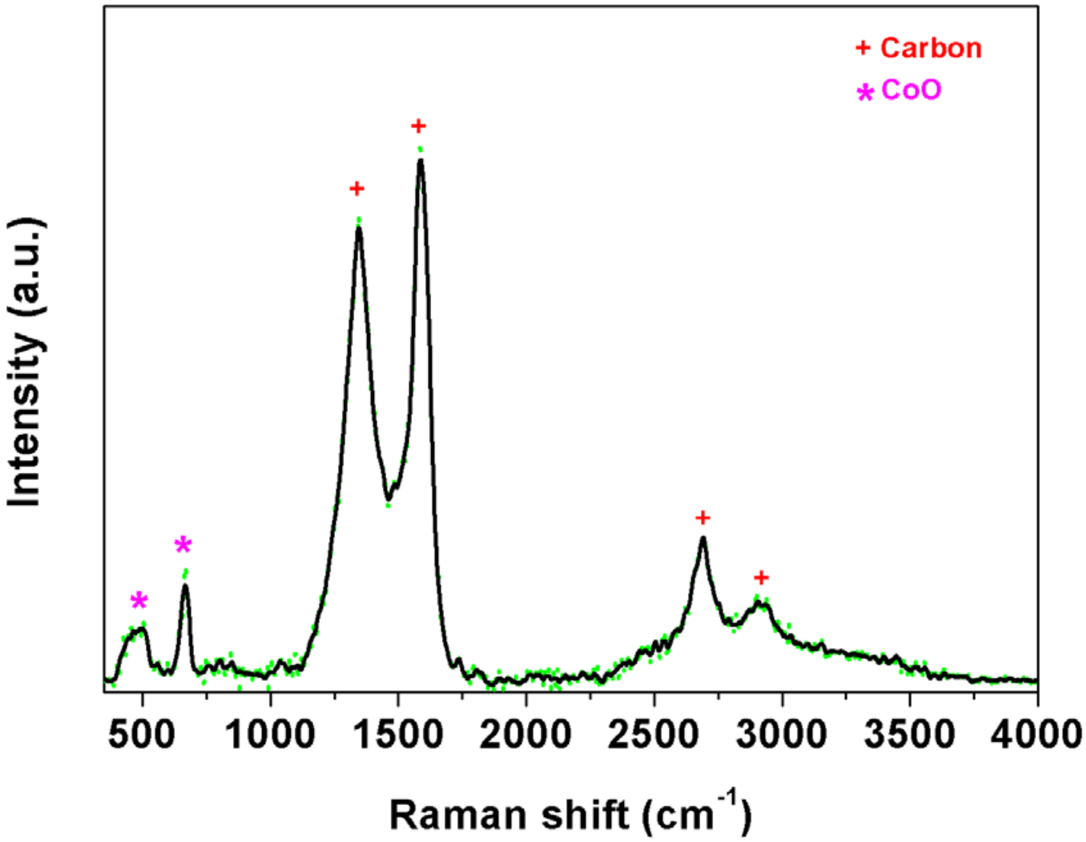

Figure 6.6 Raman spectrum of Co-GPCMs.

The phase structures of graphitic carbon and CoO nanodots embedded in the microspheres are further studied by using Raman spectrometer, the result of which is shown in Figure 6.6. As labeled by + in Figure 6.6, the peaks centered at 1338, 1593, 2694 and 2922 cm^{-1} are the representative bands of graphitic carbon [224]. Among them, the three intense peaks at 1338, 1593 and 2694 cm^{-1} are assigned to the defect, 1st order and 2nd order band of graphite, respectively [294]. Moreover, the peak centered at 2694 cm^{-1} indicates the presence of *sp*^{3} C-H and C-H_2 groups in the Co-GPCMs [295]. In addition, the presence of CoO nanodots in Co-GPCMs is further confirmed by the corresponding peak at 468 and 672 cm^{-1} (labeled by * in Figure 6.6) [296]. Thus, the result of Raman spectroscopy agrees well with the TEM and XRD studies. Since CoO is formed when the Co-based compound is annealed at 900 °C, the existence of CoO in the graphitic porous carbon frame is due to the conversion of Co-gluconate at the pyrolysis temperature as oxygen (O) is present in the α-CD and F127 [293].

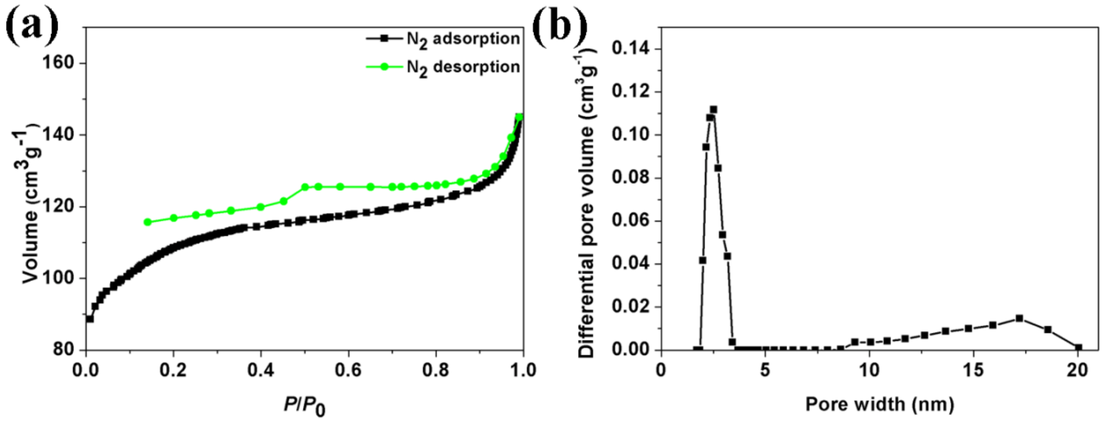

Figure 6.7 N_2 adsorption/desorption isotherm (a) and NLDFT pore size distribution (b) of Co-GPCMs

The porous structure of the carbon frame of Co-GPCMs observed by TEM is further demonstrated by the BET study using N_2, as shown in Figure 6.7. The N_2 adsorption/desorption isotherms for Co-GPCMs (Figure 6.7 a) demonstrate that both micropores and mesopores are present in the Co-GPCMs with a total BET surface area of 381 m^{2}g^{-1}. As shown in the N_2 adsorption curve, the linear increase of N_2

uptake at low pressure range, which is P/P_0=0.06-0.2, indicates a monolayer gas adsorption inside the pores [139]. When approaching the full filling of pores, the adsorption curve of N_2 shows a near plateau at P/P_0=0.2-0.9, which suggests the presence of micropores (60% in t-plot pore volume) together with some mesopores. This is further confirmed by the pore size distribution peaked at 2.5 nm (Figure 6.7 b) with a differential pore volume of 0.11 cm^3g^{-1}, which is calculated by the NLDFT method. Moreover, the sharp increase in the N_2 adsorption curve at P/P_0=0.9-1.0 corresponds to the inter-particle voids [139]. The aggregates of platy particles are responsible for non-closing hysteresis loops at P/P_0=0.4-1.0, while the ink-bottle type of pores leads to the sudden closure at P/P_0=0.4 in the N_2 desorption branch [297].

6.3.2 Supercapacitance behavior of Co-GPCMs

On the basis of the above characterizations, Co-GPCMs are shown to exhibit both micropores and mesopores inside the carbon microspheres with localized graphitic structure, which would benefit the specific surface area and electrical conductivity. The presence of CoO nanodots in the carbon matrix could give rise to pseudo-capacitance. The performance of Co-GPCMs as electrode materials in supercapacitors is evaluated by CV and galvanostatic charge-discharge measurement (Figure 6.8) in 6 M KOH aqueous electrolyte.

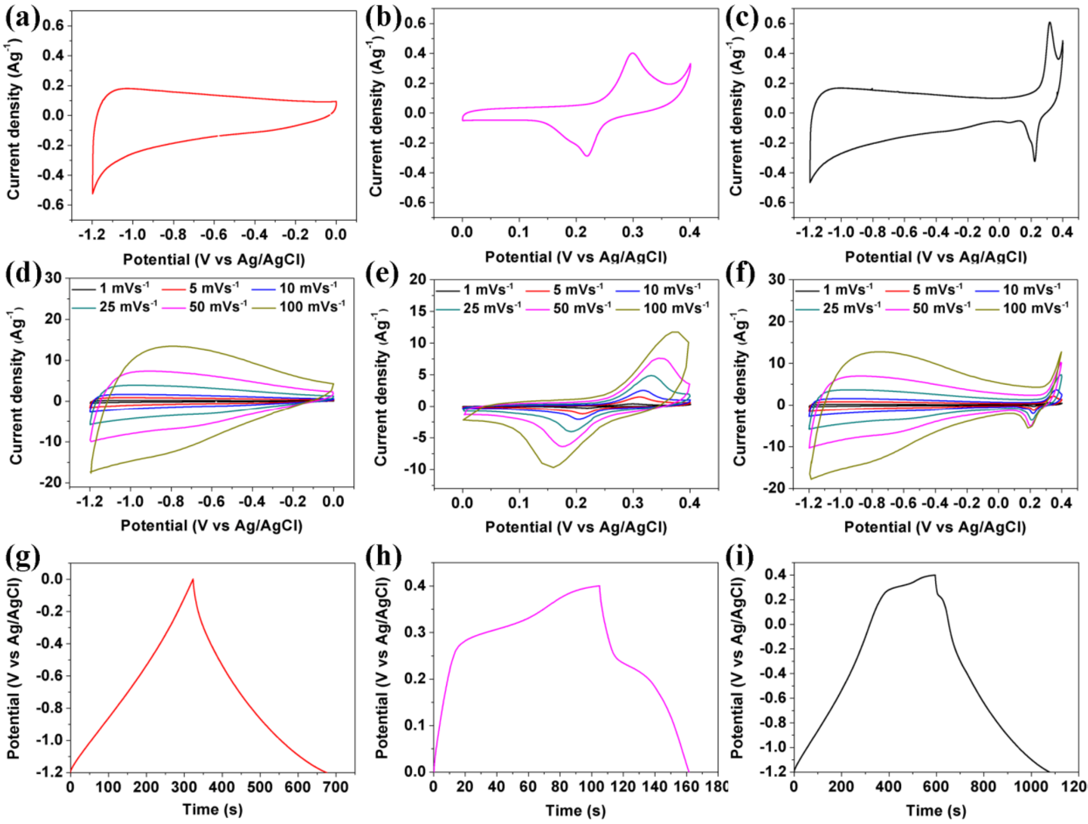

Figure 6.8 Electrochemical performance of Co-GPCMs as working electrode in the three electrode configuration: CV curve at a scan rate of 1 mVs^{-1} within the operation voltage of -1.2-0 V (a), 0-0.4 V (b) and -1.2-0.4 V (c); CV curve at different scan rates within the operation voltage of -1.2-0 V (d), 0-0.4 V (e) and -1.2-0.4 V (f) galvanostatic charge-discharge at a current density of 0.5 Ag^{-1} within the operation voltage of -1.2-0 V (g), 0-0.4 V (h) and -1.2-0.4 V (i).

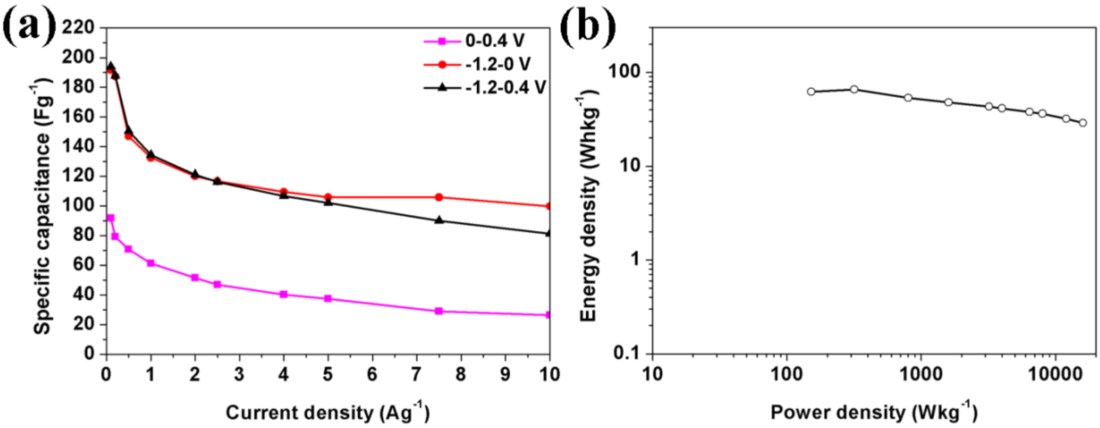

Figure 6.9 Variation of specific capacitance against different current densities within the operation voltage of -1.2-0 V, 0-0.4 V and -1.2-0.4 V (a) and the ragone plot of the supercapacitor working electrode (b) in the three electrode configuration.

As shown in Figure 6.8 a and g, the quasi-rectangular voltammogram shape and symmetric linear galvanostatic charge-discharge profile show the typical electrochemical behavior within the operation voltage of -1.2-0 V, which implies that Co-GPCMs exhibits excellent capacitive behavior and electrochemical reversibility for EDLS [292, 298]. In addition, the presence of pseudo-capacitance is demonstrated in Figure 6.8 b and h with a typical CV and galvanostatic charge-discharge shape for CoO, which indicates the faradaic reactions, $CoO + OH^- \leftrightarrow CoOOH + e^-$ and $CoOOH + OH^- \leftrightarrow CoO_2 + H_2O + e^-$, taking place within the operation voltage of 0-0.4 V [284]. Further studies with the working electrode made of Co-GPCMs within the operation voltage of -1.2-0.4 V, which is shown in Figure 6.8 c and i, show that the supercapacitor working electrode exhibits both electric double-layer capacitance and pseudo-capacitance in 6 M KOH aqueous electrolyte. Thus, the overall operation voltage of the supercapacitor working electrode made of Co-GPCMs is 1.6 V in 6 M KOH aqueous electrolyte, which is higher than the typical porous carbon and Co based materials [244-246, 253, 284]. The specific capacitance for the working electrode made from Co-GPCMs (Figure 6.9 a) is 194, 92 and 191 Fg^{-1} within the operation voltage of -1.2-0, 0-0.4 and -1.2-0.4 V, respectively, at the current density of 0.1 Ag^{-1}. These results indicate that the overall specific capacitance of Co-GPCMs is at least comparable to porous carbon materials, while doping CoO nanodots into the carbon matrix gives rise to an extension of operation voltage.

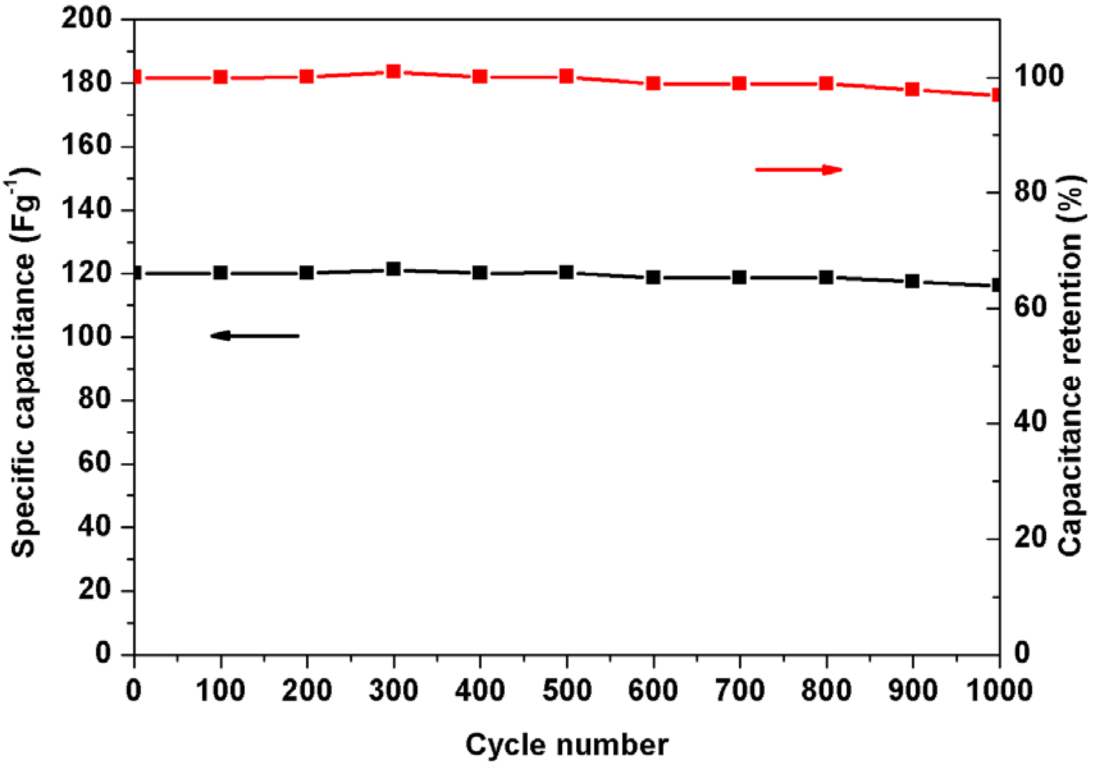

Figure 6.10 Cycle life and capacitance retention of the working electrode made of Co-GPCMs. The operation voltage is 1.6 V and the current density is 2.0 A g^{-1}.

The specific capacitance of the working electrode made of Co-GPCMs could retain 40% with the increase in current density from 0.1 to 10 Ag^{-1} (Figure 6.9 a), while the shape of CV is still maintained with the increase in scan rate from 1 to 100 mVs^{-1} (Figure 6.8 d-f). This highlights that the working electrode would be suitable for fast charge-discharge and high scan rate operations within the potential window of 1.6 V [85, 299]. The high operation voltage (1.6 V) of the working electrode made of Co-GPCMs could therefore generate an improved high energy density for supercapacitors. In order to understand the performance for energy density, the ragone plot (Figure 6.9 b) is calculated based on the CV and galvanostatic charge-discharge results, where one sees an energy density of 62 Whkg^{-1} at a power density of 152 Wkg^{-1}. It maintains 29 Whkg^{-1} at a power density of 1.6 kWkg^{-1} in the three electrode system.

These data demonstrate the excellent capacitive performance of Co-GPCMs with the aqueous electrolyte [85]. Concerning the cyclic retention, the working electrode made of Co-GPCMs could retain 97% of the specific capacitance after 1000 cycles of measurement (Figure 6.10).

6.4 Summary

A new design and synthetic process are developed for hybrid-type carbon microspheres, which exhibit a graphitic porous structure. Co-GPCMs are successfully realized by the hydrothermal treatment of Co-gluconate and α-CD in the presence of F127, followed by pyrolysis at high temperature in Ar. The Co-GPCMs consists of a porous carbon matrix with localized graphitic structure while CoO nanodots are embedded in the carbon frame. The nanohybrid structure is aimed at effectively combining the electric double-layer capacitance and pseudo-capacitance, which has been successfully demonstrated when used as the electrode material in supercapacitors. The combination of EDLS, which is generated by the porous graphitic carbon, and pseudo-supercapacitors, which is generated by CoO, leads to a high operation voltage (1.6 V), which gives rise to a high energy density.

7 Conclusions and suggestions for future work

7.1 Conclusions

In this project, new synthetic techniques based on hydrothermal treatment of carbohydrates in the presence of inorganic or organic additives and directing agents are developed for spherical carbon structures ranging from nanometers to micrometers in sizes with controlled surface characteristics, porosity and fluorescent behavior. On this basis, porous spherical carbon nanohybrids containing manganese dioxide (MnO_2) nanoparticles and cobalt monoxide (CoO) dots are developed for supercapacitance applications.

Five types of spherical carbon structures and nanohybrids are investigated in this project. Firstly, hydrothermal treatment of glucose in the presence of monopotassium phosphate (K_2HPO_4) at 200 ^{o}C generated carbon spheres of <10 nm in sizes, which are termed as carbon dots (C-dots) showing fascinating fluorescent behavior. These C-dots are almost monodispersed and have strong fluorescence emission. Their sizes can be tuned by just changing the concentration of K_2HPO_4, e.g., 1.83 nm at 1/36 glucose/K_2HPO_4 molar ratio and 3.83 nm at 1/26 molar ratio. As a result, the fluorescence emission of these carbon dots thus produced is tunable from green color (510 nm) to blue color (435 nm). The difference in emission color corresponding to the particle size is due to the size dependent quantum effect that is derived from the surface passivation. In addition, the carbon dots have excellent functional behavior, such as the pH-stability from 3 to 12 and photostability. For bioimaging application, they show no appreciable cytotoxicity for the cells cultured for 72 h in the solution of 0.625 $\mathrm{mgmL^{-1}}$ carbon dots. Although the study was not extended to other fluorescent emissions, a new perspective is shown for fluorescent C-dots with tunable emission.

Secondly, using glucosamine hydrochloride (glucosamine-HCl) as the carbon precursor, nitrogen-doped carbon nanoparticles are developed, which are shown to exhibit aromatic amine, hydroxyl and carboxyl surface groups and intrinsically fluorescent behavior. At the excitation wavelength of 430 to 470 nm, the nitrogen-doped carbon nanoparticles are demonstrated to emit green fluorescence (510 nm). This finding is significant as the nitrogen-doped carbon nanoparticles show excitation wavelength-independent emission behavior, which is different from the wavelength-dependent emission behavior that have been demonstrated for other types of fluorescent carbon nanoparticles of oxygen passivation. When glucosamine-HCl, which contains both oxygen and nitrogen atoms, is carbonized under hydrothermal condition of 140 ^{o}C, the carbon surface is passivated by the both oxygen and nitrogen, creating additional types of defect sites to trap the excitation energy to stable the fluorescent emission. Although the exact surface passivation diagram and defects is the subject of further in depth investigation, the formation of nitrogen-doped carbon nanoparticles provides a new insight for further study of nitrogen-doped carbon.

With the understanding that a supermolecular inclusion complexation can be formed between α-cyclodextrin (α-CD) and poly (ethylene oxide) (PEO), hollow carbon spheres with an inner macropore and meso-/microporous carbon wall is successfully established by hydrothermal treatment of α-CD in the presence of poly (ethylene oxide)$_{106}$-poly (propylene oxide)$_{70}$-poly (ethylene oxide)$_{106}$ (F127) as the soft template. By varying the concentration of F127 from 0.019 wt. % to 0.075 wt. %, the size and wall thickness of the hollow carbon spheres are tuned correspondingly. The observed variation in particle size and wall thickness is due to the change of vesicle structures formed by F127/α-CD complexes within different concentrations in aqueous solution. F127 is preserved during the hydrothermal carbonization of α-CD, which leads to the excellent hydrophilic behavior for hollow carbon spheres. Alternatively, it can be removed by pyrolysis treatment at 900 ^{o}C under argon (Ar) gas protection to yield meso-/microporous external carbon wall without collapsing the hollow structure. The hollow carbon spheres exhibits excellent charge capacity when used as anode materials in lithium (Li) ion batteries. Nevertheless, the specific surface area and Li storage value can be further modified.

Hollow nanocarbon spheres-nanocrystalline MnO_2 hybrids are successfully developed by assembling the nanocrystallites of α phase MnO_2 through the redox reaction between permanganate (MnO_4^-) and carbon surface. In particular, a double layer structure of MnO_2 is demonstrated by properly controlling the diffusion time (16 h) of MnO_4^- into the hollow core. This gives rise to improvement in the specific capacitance when the nanohybrid is employed as the supercapacitor electrode. The increase in specific capacitance is due to the creation of electrochemically active surface. Nevertheless, the overall capacitance is controlled by the low electrical conductivity and the likely dissolution of MnO_2 nanocrystallites in the electrolyte.

The new approach demonstrated in this project provides an alternative strategy for fabricating hollow carbon-transitional metal oxide for supercapacitors.

A new spherical carbon hybrid structure, denoted as cobalt monoxide (CoO)-doped graphitic porous carbon microspheres (Co-GPCMs), is developed by hydrothermal treatment of α-CD together with cobalt gluconate (Co-gluconate) in the presence of F127 and then pyrolysis treatment. Arising from Co-gluconate, CoO is uniformly distributed within the carbon microspheres upon hydrothermal treatment, where there is hydrogen bond between F127 and α-CD. The subsequent pyrolysis treatment of the carbon microspheres together with Co-gluconate leads to the porous spherical carbon structure with onion-shaped graphitic pore and CoO nanodots, where F127 acts as the pore generation agent and cobalt (Co) element acts the catalyst for graphitization. This unique spherical carbon hybrid structure helps increase the energy density when used as the supercapacitor working electrode in aqueous electrolyte, since the overall operation voltage (1.6 V) is higher than those of carbon-based materials. This structure enables the combination of electric double-layer supercapacitor from carbon and pseudo-supercapacitor from CoO. In addition, the onion-shaped graphitic porous carbon structure leads to a high surface area and electrical conductivity.

7.2 Suggestions for future work

In spite of the fact that the new synthetic strategies have been developed to produce spherical carbon structures and hybrids via hydrothermal carbonization routes, there is considerable scope for further study.

While the hydrothermal synthetic strategies have been developed for producing intrinsically fluorescent C-dots and nitrogen-doped carbon nanoparticles, there is a need for in-depth study in order to understand the exact physical mechanism and origins for fluorescence generated by surface passivation. The surface structure of spherical carbon structures derived from hydrothermal carbonization is rather complicated. In addition to experimental work, computational investigation will be an interesting area for future research to clarify the surface energy diagram and fluorescent behavior. Given that fluorescent C-dots could be synthesized by hydrothermal treatment of glucose in the presence of K_2HPO_4, while glucosamine could produce nitrogen-doped carbon nanoparticles, it would be of interest to develop nitrogen-doped C-dots. While the fluorescence emission is so far limited to blue and green as shown in this study, fluorescence carbon nanoparticles with multi-colors could be an interesting research topic in future work.

In developing the porous spherical carbon structures and nanohybrids, F127 is shown to play an important role as the soft template. Since there are a number of other block co-polymers, it would be interesting to use different block co-polymers, which may well lead to different structures for the carbon-based materials. In addition, since nitrogen-doped carbon nanoparticles could be synthesized from glucosamine as the carbon precursor, future research can attempt to develop nitrogen-doped hollow carbon spheres or graphitic porous carbon spheres. Indeed, nitrogen-doped carbon materials have been demonstrated with some interesting performance in catalysis, gas sequestration, environmental protection and energy storage.

8 Bibliography

[1] A.H. Lu, G.P. Hao, Q. Sun, X.Q. Zhang, W.C. Li, Macromol. Chem. Phys., 213 (2012) 1107-1131.

[2] S. Stankovich, D.A. Dikin, G.H.B. Dommett, K.M. Kohlhaas, E.J. Zimney, E.A. Stach, R.D. Piner, S.T. Nguyen, R.S. Ruoff, Nature, 442 (2006) 282-286.

[3] A.A. Balandin, S. Ghosh, W.Z. Bao, I. Calizo, D. Teweldebrhan, F. Miao, C.N. Lau, Nano Lett., 8 (2008) 902-907.

[4] J. Lee, J. Kim, T. Hyeon, Adv. Mater., 18 (2006) 2073-2094.

[5] H. Kaper, A. Grandjean, C. Weidenthaler, F. Schuth, F. Goettmann, Chemistry-a European Journal, 18 (2012) 4099-4106.

[6] C. Liu, H.M. Cheng, Journal of Physics D-Applied Physics, 38 (2005) R231-R252.

[7] T. Fukutsuka, T. Yamaguchi, S.I. Miyano, Y. Matsuo, Y. Sugie, Z. Ogumi, J. Power Sources, 174 (2007) 199-205.

[8] E. Frackowiak, Phys. Chem. Chem. Phys., 9 (2007) 1774-1785.

[9] H.W. Kroto, J.R. Heath, S.C. Obrien, R.F. Curl, R.E. Smalley, Nature, 318 (1985) 162-163.

[10] A.M. Schrand, S.A.C. Hens, O.A. Shenderova, Crit. Rev. Solid State Mat. Sci., 34 (2009) 18-74.

[11] X.M. Sun, Y.D. Li, Angew. Chem.-Int. Edit., 43 (2004) 597-601.

[12] T. Luo, L.S. Gao, J.W. Liu, L.Y. Chen, J.M. Shen, L.C. Wang, Y.T. Qian, J. Phys. Chem. B, 109 (2005) 15272-15277.

[13] D. Banerjee, D. Sen, K.K. Chattopadhyay, Microporous Mesoporous Mat., 171 (2013) 201-207.

[14] Y.D. Xia, R. Mokaya, Adv. Mater., 16 (2004) 886-891.

[15] S. Iijima, Nature, 354 (1991) 56-58.

[16] S.G. Rao, L. Huang, W. Setyawan, S.H. Hong, Nature, 425 (2003) 36-37.

[17] P.W. Manders, Nature, 271 (1978) 142-143.

[18] M.H. Al-Saleh, U. Sundararaj, Carbon, 47 (2009) 2-22.

[19] B.Z. Tian, S.N. Che, Z. Liu, X.Y. Liu, W.B. Fan, T. Tatsumi, O. Terasaki, D.Y. Zhao, Chem. Commun., (2003) 2726-2727.

[20] A.K. Geim, K.S. Novoselov, Nat. Mater., 6 (2007) 183-191.

[21] W.S. Hummers, R.E. Offeman, J. Am. Chem. Soc., 80 (1958) 1339-1339.

[22] K.S. Novoselov, A.K. Geim, S.V. Morozov, D. Jiang, Y. Zhang, S.V. Dubonos, I.V. Grigorieva, A.A. Firsov, Science, 306 (2004) 666-669.

[23] G.L. Che, B.B. Lakshmi, E.R. Fisher, C.R. Martin, Nature, 393 (1998) 346-349.

[24] K.T. Lee, J.C. Lytle, N.S. Ergang, S.M. Oh, A. Stein, Adv. Funct. Mater., 15 (2005) 547-556.

[25] J. Lee, K. Sohn, T. Hyeon, J. Am. Chem. Soc., 123 (2001) 5146-5147.

[26] L. Cao, X. Wang, M.J. Meziani, F.S. Lu, H.F. Wang, P.J.G. Luo, Y. Lin, B.A. Harruff, L.M. Veca, D. Murray, S.Y. Xie, Y.P. Sun, J. Am. Chem. Soc., 129 (2007) 11318-11319.

[27] B. You, J. Yang, Y.Q. Sun, Q.D. Su, Chem. Commun., 47 (2011) 12364-12366.

[28] L.R. Kong, X.F. Lu, X.J. Bian, W.J. Zhang, C. Wang, Langmuir, 26 (2010) 5985-5990.

[29] L.M. Guo, L.X. Zhang, J.M. Zhang, J. Zhou, Q.J. He, S.Z. Zeng, X.Z. Cui, J.L. Shi, Chem. Commun., (2009) 6071-6073.

[30] G.S. Chai, I.S. Shin, J.S. Yu, Adv. Mater., 16 (2004) 2057-2061.

[31] B.R. Selvi, D. Jagadeesan, B.S. Suma, G. Nagashankar, M. Arif, K. Balasubramanyam, M. Eswaramoorthy, T.K. Kundu, Nano Lett., 8 (2008) 3182-3188.

[32] S. Ikeda, K. Tachi, Y.H. Ng, Y. Ikoma, T. Sakata, H. Mori, T. Harada, M. Matsumura, Chem. Mat., 19 (2007) 4335-4340.

[33] S.N. Baker, G.A. Baker, Angew. Chem.-Int. Edit., 49 (2010) 6726-6744.

[34] Y.P. Sun, B. Zhou, Y. Lin, W. Wang, K.A.S. Fernando, P. Pathak, M.J. Meziani, B.A. Harruff, X. Wang, H.F. Wang, P.J.G. Luo, H. Yang, M.E. Kose, B.L. Chen, L.M. Veca, S.Y. Xie, J. Am. Chem. Soc., 128 (2006) 7756-7757.

[35] W. Kwon, S. Do, D.C. Won, S.W. Rhee, ACS Appl. Mater. Interfaces, 5 (2013) 822-827.

[36] Y. Xu, M. Wu, Y. Liu, X.Z. Feng, X.B. Yin, X.W. He, Y.K. Zhang, Chemistry-a European Journal, 19 (2013) 2276-2283.

[37] J.E. Riggs, Z.X. Guo, D.L. Carroll, Y.P. Sun, J. Am. Chem. Soc., 122 (2000) 5879-5880.

[38] A. Gruber, A. Drabenstedt, C. Tietz, L. Fleury, J. Wrachtrup, C. vonBorczyskowski, Science, 276 (1997) 2012-2014.

[39] Vlasov, II, O. Shenderova, S. Turner, O.I. Lebedev, A.A. Basov, I. Sildos, M. Rahn, A.A. Shiryaev, G. Van Tendeloo, Small, 6 (2010) 687-694.

[40] Y.M. Guo, Z. Wang, H.W. Shao, X.Y. Jiang, Carbon, 52 (2013) 583-589.

[41] S.K. Bhunia, A. Saha, A.R. Maity, S.C. Ray, N.R. Jana, Sci Rep, 3 (2013).

[42] A. Khanam, S.K. Tripathi, D. Roy, M. Nasim, Colloid Surf. B-Biointerfaces, 102 (2013) 63-69.

[43] B.S. Chen, F.M. Li, S.X. Li, W. Weng, H.X. Guo, T. Guo, X.Y. Zhang, Y.B. Chen, T.T. Huang, X.L. Hong, S.Y. You, Y.M. Lin, K.H. Zeng, S. Chen, Nanoscale, 5 (2013) 1967-1971.

[44] S.L. Hu, K.Y. Niu, J. Sun, J. Yang, N.Q. Zhao, X.W. Du, Journal of Materials Chemistry, 19 (2009) 484-488.

[45] H.P. Liu, T. Ye, C.D. Mao, Angew. Chem.-Int. Edit., 46 (2007) 6473-6475.

[46] S.L. Hu, Y. Guo, Y.G. Dong, J.L. Yang, J. Liu, S.R. Cao, Journal of Materials Chemistry, 22 (2012) 12053-12057.

[47] H.T. Li, Z.H. Kang, Y. Liu, S.T. Lee, Journal of Materials Chemistry, 22 (2012) 24230-24253.

[48] P.C. Hsu, H.T. Chang, Chem. Commun., 48 (2012) 3984-3986.

[49] Y.C. Song, W. Shi, W. Chen, X.H. Li, H.M. Ma, Journal of Materials Chemistry, 22 (2012) 12568-12573.

[50] S.J. Zhu, Q.N. Meng, L. Wang, J.H. Zhang, Y.B. Song, H. Jin, K. Zhang, H.C. Sun, H.Y. Wang, B. Yang, Angew. Chem.-Int. Edit., 52 (2013) 3953-3957.

[51] X.Y. Xu, R. Ray, Y.L. Gu, H.J. Ploehn, L. Gearheart, K. Raker, W.A. Scrivens, J. Am. Chem. Soc., 126 (2004) 12736-12737.

[52] Y.P. Sun, X. Wang, F.S. Lu, L. Cao, M.J. Meziani, P.J.G. Luo, L.R. Gu, L.M. Veca, J. Phys. Chem. C, 112 (2008) 18295-18298.

[53] X. Wang, L. Cao, F.S. Lu, M.J. Meziani, H. Li, G. Qi, B. Zhou, B.A. Harruff, F. Kermarrec, Y.P. Sun, Chem. Commun., (2009) 3774-3776.

[54] S.T. Yang, L. Cao, P.G.J. Luo, F.S. Lu, X. Wang, H.F. Wang, M.J. Meziani, Y.F. Liu, G. Qi, Y.P. Sun, J. Am. Chem. Soc., 131 (2009) 11308-11309.

[55] S.T. Yang, X. Wang, H.F. Wang, F.S. Lu, P.J.G. Luo, L. Cao, M.J. Meziani, J.H. Liu, Y.F. Liu, M. Chen, Y.P. Huang, Y.P. Sun, J. Phys. Chem. C, 113 (2009) 18110-18114.

[56] S.L. Hu, J. Liu, J.L. Yang, Y.Z. Wang, S.R. Cao, J. Nanopart. Res., 13 (2011) 7247-7252.

[57] S.L. Hu, Y.G. Dong, J.L. Yang, J. Liu, S.R. Cao, Journal of Materials Chemistry, 22 (2012) 1957-1961.

[58] Q.L. Zhao, Z.L. Zhang, B.H. Huang, J. Peng, M. Zhang, D.W. Pang, Chem. Commun., (2008) 5116-5118.

[59] L.Y. Zheng, Y.W. Chi, Y.Q. Dong, J.P. Lin, B.B. Wang, J. Am. Chem. Soc., 131 (2009) 4564-4565.

[60] J.G. Zhou, C. Booker, R.Y. Li, X.T. Zhou, T.K. Sham, X.L. Sun, Z.F. Ding, J. Am. Chem. Soc., 129 (2007) 744-745.

[61] L. Bao, Z.L. Zhang, Z.Q. Tian, L. Zhang, C. Liu, Y. Lin, B.P. Qi, D.W. Pang, Adv. Mater., 23 (2011) 5801-5806.

[62] J. Lu, J.X. Yang, J.Z. Wang, A.L. Lim, S. Wang, K.P. Loh, ACS Nano, 3 (2009) 2367-2375.

[63] S.C. Ray, A. Saha, N.R. Jana, R. Sarkar, J. Phys. Chem. C, 113 (2009) 18546-18551.

[64] L. Tian, D. Ghosh, W. Chen, S. Pradhan, X.J. Chang, S.W. Chen, Chem. Mat., 21 (2009) 2803-2809.

[65] P. Kumar, H.B. Bohidar, J. Nanopart. Res., 14 (2012).

[66] R.L. Liu, D.Q. Wu, S.H. Liu, K. Koynov, W. Knoll, Q. Li, Angew. Chem.-Int. Edit., 48 (2009) 4598-4601.

[67] A.B. Bourlinos, A. Stassinopoulos, D. Anglos, R. Zboril, V. Georgakilas, E.P. Giannelis, Chem. Mat., 20 (2008) 4539-4541.

[68] A.B. Bourlinos, A. Stassinopoulos, D. Anglos, R. Zboril, M. Karakassides, E.P. Giannelis, Small, 4 (2008) 455-458.

[69] H. Zhu, X.L. Wang, Y.L. Li, Z.J. Wang, F. Yang, X.R. Yang, Chem. Commun., (2009) 5118-5120.

[70] H. Peng, J. Travas-Sejdic, Chem. Mat., 21 (2009) 5563-5565.

[71] C.D. Liang, Z.J. Li, S. Dai, Angew. Chem.-Int. Edit., 47 (2008) 3696-3717.

[72] L. Sun, C.G. Tian, L. Wang, J.L. Zou, G. Mu, H.G. Fu, Journal of Materials Chemistry, 21 (2011) 7232-7239.

[73] Z.Y. Wang, F. Li, N.S. Ergang, A. Stein, Chem. Mat., 18 (2006) 5543-5553.

[74] L. Eliad, G. Salitra, A. Soffer, D. Aurbach, J. Phys. Chem. B, 105 (2001) 6880-6887.

[75] R.I. Baxter, R.D. Rawlings, N. Iwashita, Y. Sawada, Carbon, 38 (2000) 441-449.

[76] K.T. Lee, Y.S. Jung, S.M. Oh, J. Am. Chem. Soc., 125 (2003) 5652-5653.

[77] Z.R. Guan, L. Liu, L.L. He, S. Yang, J. Hazard. Mater., 196 (2011) 270-277.

[78] A.B. Fuertes, P. Tartaj, Chem. Mat., 18 (2006) 1675-1679.

[79] Z.B. Lei, Y. Xiao, L.Q. Dang, S.Y. Bai, L.Z. An, Microporous Mesoporous Mat., 109 (2008) 109-117.

[80] T. Nakamura, Y. Yamada, K. Yano, Microporous Mesoporous Mat., 117 (2009) 478-485.

[81] M. Il Kim, C.H. Yun, Y.J. Kim, C.R. Park, M. Inagaki, Carbon, 40 (2002) 2003-2012.

[82] C. Scherdel, T. Scherb, G. Reichenauer, Carbon, 47 (2009) 2244-2252.

[83] C.O. Ania, V. Khomenko, E. Raymundo-Pinero, J.B. Parra, F. Beguin, Adv. Funct. Mater., 17 (2007) 1828-1836.

[84] W.R. Li, D.H. Chen, Z. Li, Y.F. Shi, Y. Wan, G. Wang, Z.Y. Jiang, D.Y. Zhao, Carbon, 45 (2007) 1757-1763.

[85] D.W. Wang, F. Li, M. Liu, G.Q. Lu, H.M. Cheng, Angew. Chem.-Int. Edit., 47 (2008) 373-376.

[86] F.D. Han, Y.J. Bai, R. Liu, B. Yao, Y.X. Qi, N. Lun, J.X. Zhang, Adv. Energy Mater., 1 (2011) 798-801.

[87] S.B. Yang, X.L. Feng, L.J. Zhi, Q.A. Cao, J. Maier, K. Mullen, Adv. Mater., 22 (2010) 838-842.

[88] Y.S. Hu, P. Adelhelm, B.M. Smarsly, S. Hore, M. Antonietti, J. Maier, Adv. Funct. Mater., 17 (2007) 1873-1878.

[89] G.S. Chai, S.B. Yoon, J.H. Kim, J.S. Yu, Chem. Commun., (2004) 2766-2767.

[90] S.J. Han, Y.K. Yun, K.W. Park, Y.E. Sung, T. Hyeon, Adv. Mater., 15 (2003) 1922-1925.

[91] B.Z. Fang, M. Kim, J.H. Kim, J.S. Yu, Langmuir, 24 (2008) 12068-12072.

[92] Y.D. Xia, R. Mokaya, D.M. Grant, G.S. Walker, Carbon, 49 (2011) 844-853.

[93] X.C. Chen, K. Kierzek, Z.W. Jiang, H.M. Chen, T. Tang, M. Wojtoniszak, R.J. Kalenczuk, P.K. Chu, E. Borowiak-Palen, J. Phys. Chem. C, 115 (2011) 17717-17724.

[94] A.H. Lu, T. Sun, W.C. Li, Q. Sun, F. Han, D.H. Liu, Y. Guo, Angew. Chem.-Int. Edit., 50 (2011) 11765-11768.

[95] G.X. Ma, R.R. Jia, J.H. Zhao, Z.J. Wang, C. Song, S.P. Jia, Z.P. Zhu, J. Phys. Chem. C, 115 (2011) 25148-25154.

[96] S. Kubo, R. Demir-Cakan, L. Zhao, R.J. White, M.M. Titirici, ChemSusChem, 3 (2010) 188-194.

[97] R. Ryoo, S.H. Joo, S. Jun, J. Phys. Chem. B, 103 (1999) 7743-7746.

[98] S. Jun, S.H. Joo, R. Ryoo, M. Kruk, M. Jaroniec, Z. Liu, T. Ohsuna, O. Terasaki, J. Am. Chem. Soc., 122 (2000) 10712-10713.

[99] J. Lee, S. Yoon, T. Hyeon, S.M. Oh, K.B. Kim, Chem. Commun., (1999) 2177-2178.

[100] M. Kruk, B. Dufour, E.B. Celer, T. Kowalewski, M. Jaroniec, K. Matyjaszewski, J. Phys. Chem. B, 109 (2005) 9216-9225.

[101] A.H. Lu, A. Kiefer, W. Schmidt, F. Schuth, Chem. Mat., 16 (2004) 100-103.

[102] S. Alvarez, A.B. Fuertes, Carbon, 42 (2004) 433-436.

[103] S.S. Kim, T.J. Pinnavaia, Chem. Commun., (2001) 2418-2419.

[104] J. Lee, S. Yoon, S.M. Oh, C.H. Shin, T. Hyeon, Adv. Mater., 12 (2000) 359-362.

[105] M.T. Zheng, Y.L. Liu, S.A. Zhao, W.Q. He, Y. Xiao, D.S. Yuan, Inorg. Chem., 49 (2010) 8674-8683.

[106] J.B. Joo, P. Kim, W. Kim, J. Kim, N.D. Kim, J. Yi, Curr. Appl. Phys., 8 (2008) 814-817.

[107] C.F. Zhang, H.B. Wu, C.Z. Yuan, Z.P. Guo, X.W. Lou, Angew. Chem.-Int. Edit., 51 (2012) 9592-9595.

[108] T. Kyotani, T. Nagai, S. Inoue, A. Tomita, Chem. Mat., 9 (1997) 609-615.

[109] J.H. Knox, B. Kaur, G.R. Millward, Journal of Chromatography, 352 (1986) 3-25.

[110] F.L. Wang, L.L. Pang, Y.Y. Jiang, B. Chen, D. Lin, N. Lun, H.L. Zhu, R. Liu, X.L. Meng, Y. Wang, Y.J. Bai, L.W. Yin, Mater. Lett., 63 (2009) 2564-2566.

[111] Y. Oda, K. Fukuyama, K. Nishikawa, S. Namba, H. Yoshitake, T. Tatsumi, Chem. Mat., 16 (2004) 3860-3866.

[112] M. Yang, J. Ma, S.J. Ding, Z.K. Meng, J.G. Liu, T. Zhao, L.Q. Mao, Y. Shi, X.G. Jin, Y.F. Lu, Z.Z. Yang, Macromol. Chem. Phys., 207 (2006) 1633-1639.

[113] Y.S. Li, Y.Q. Yang, J.L. Shi, M.L. Ruan, Microporous Mesoporous Mat., 112 (2008) 597-602.

[114] F.B. Su, X.S. Zhao, Y. Wang, L.K. Wang, J.Y. Lee, Journal of Materials Chemistry, 16 (2006) 4413-4419.

[115] J.S. Yu, S.B. Yoon, Y.J. Lee, K.B. Yoon, J. Phys. Chem. B, 109 (2005) 7040-7045.

[116] C. Almeida, A.J.G. Zarbin, Carbon, 44 (2006) 2869-2876.

[117] A.B. Fuertes, P. Valle-Vigon, M. Sevilla, Chem. Commun., 48 (2012) 6124-6126.

[118] C.H. Xiao, X.C. Chu, Y. Yang, X. Li, X.H. Zhang, J.H. Chen, Biosens. Bioelectron., 26 (2011) 2934-2939.

[119] S.B. Yoon, K. Sohn, J.Y. Kim, C.H. Shin, J.S. Yu, T. Hyeon, Adv. Mater., 14 (2002) 19-21.

[120] L. Zhi, J.J. Wang, G.L. Cui, M. Kastler, B. Schmaltz, U. Kolb, U. Jonas, K. Mullen, Adv. Mater., 19 (2007) 1849-1853.

[121] L. Chuenchom, R. Kraehnert, B.M. Smarsly, Soft Matter, 8 (2012) 10801-10812.

[122] Y. Meng, D. Gu, F.Q. Zhang, Y.F. Shi, L. Cheng, D. Feng, Z.X. Wu, Z.X. Chen, Y. Wan, A. Stein, D.Y. Zhao, Chem. Mat., 18 (2006) 4447-4464.

[123] C.D. Liang, K.L. Hong, G.A. Guiochon, J.W. Mays, S. Dai, Angew. Chem.-Int. Edit., 43 (2004) 5785-5789.

[124] D. Tashima, E. Yamamoto, N. Kai, D. Fujikawa, G. Sakai, M. Otsubo, T. Kijima, Carbon, 49 (2011) 4848-4857.

[125] H. Kosonen, S. Valkama, A. Nykanen, M. Toivanen, G. ten Brinke, J. Ruokolainen, O. Ikkala, Adv. Mater., 18 (2006) 201-205.

[126] Y.H. Deng, T. Yu, Y. Wan, Y.F. Shi, Y. Meng, D. Gu, L.J. Zhang, Y. Huang, C. Liu, X.J. Wu, D.Y. Zhao, J. Am. Chem. Soc., 129 (2007) 1690-1697.

[127] C.D. Liang, S. Dai, J. Am. Chem. Soc., 128 (2006) 5316-5317.

[128] F.Q. Zhang, Y. Meng, D. Gu, Y. Yan, C.Z. Yu, B. Tu, D.Y. Zhao, J. Am. Chem. Soc., 127 (2005) 13508-13509.

[129] J.Y. Zhang, Y.H. Deng, J. Wei, Z.K. Sun, D. Gu, H. Bongard, C. Liu, H.H. Wu, B. Tu, F. Schuth, D.Y. Zhao, Chem. Mat., 21 (2009) 3996-4005.

[130] Y.H. Deng, J. Liu, C. Liu, D. Gu, Z.K. Sun, J. Wei, J.Y. Zhang, L.J. Zhang, B. Tu, D.Y. Zhao, Chem. Mat., 20 (2008) 7281-7286.

[131] G.J.D. Soler-illia, C. Sanchez, B. Lebeau, J. Patarin, Chem. Rev., 102 (2002) 4093-4138.

[132] Y. Wan, D.Y. Zhao, Chem. Rev., 107 (2007) 2821-2860.

[133] M. Yang, G. Wang, Colloid Surf. A-Physicochem. Eng. Asp., 345 (2009) 121-126.

[134] R.J. White, K. Tauer, M. Antonietti, M.M. Titirici, J. Am. Chem. Soc., 132 (2010) 17360-17363.

[135] S. Valkama, A. Nykanen, H. Kosonen, R. Ramani, F. Tuomisto, P. Engelhardt, G. ten Brinke, O. Ikkala, J. Ruokolainen, Adv. Funct. Mater., 17 (2007) 183-190.

[136] S. Tanaka, N. Nishiyama, Y. Egashira, K. Ueyama, Chem. Commun., (2005) 2125-2127.

[137] D.H. Long, W.M. Qiao, L. Zhan, X.Y. Liang, L.C. Ling, Microporous Mesoporous Mat., 121 (2009) 58-66.

[138] U.B. Suryavanshi, T. Ijima, A. Hayashi, Y. Hayashi, M. Tanemura, Chem. Commun., 47 (2011) 10758-10760.

[139] S. Kubo, R.J. White, N. Yoshizawa, M. Antonietti, M.M. Titirici, Chem. Mat., 23 (2011) 4882-4885.

[140] K.P. Gierszal, S.B. Yoon, J.S. Yu, M. Jaroniec, Journal of Materials Chemistry, 16 (2006) 2819-2823.

[141] Y. Meng, D. Gu, F.Q. Zhang, Y.F. Shi, H.F. Yang, Z. Li, C.Z. Yu, B. Tu, D.Y. Zhao, Angew. Chem.-Int. Edit., 44 (2005) 7053-7059.

[142] X.Q. Wang, C.D. Liang, S. Dai, Langmuir, 24 (2008) 7500-7505.

[143] L.F. Lai, G.M. Huang, X.F. Wang, J. Weng, Carbon, 48 (2010) 3145-3156.

[144] R. Saliger, U. Fischer, C. Herta, J. Fricke, J. Non-Cryst. Solids, 225 (1998) 81-85.

[145] D.R. Rolison, J.W. Long, J.C. Lytle, A.E. Fischer, C.P. Rhodes, T.M. McEvoy, M.E. Bourga, A.M. Lubers, Chem. Soc. Rev., 38 (2009) 226-252.

[146] X.H. Zeng, D.C. Wu, R.W. Fu, H.J. Lai, Mater. Chem. Phys., 112 (2008) 1074-1077.

[147] G.R. Li, Z.P. Feng, Y.N. Ou, D.C. Wu, R.W. Fu, Y.X. Tong, Langmuir, 26 (2010) 2209-2213.

[148] R.W. Pekala, J. Mater. Sci., 24 (1989) 3221-3227.

[149] R.W. Pekala, J.C. Farmer, C.T. Alviso, T.D. Tran, S.T. Mayer, J.M. Miller, B. Dunn, J. Non-Cryst. Solids, 225 (1998) 74-80.

[150] R.W. Pekala, R.W. Hopper, J. Mater. Sci., 22 (1987) 1840-1844.

[151] J.C. Lytle, J.M. Wallace, M.B. Sassin, A.J. Barrow, J.W. Long, J.L. Dysart, C.H. Renninger, M.P. Saunders, N.L. Brandell, D.R. Rolison, Energy Environ. Sci., 4 (2011) 1913-1925.

[152] W.S. Baker, J.W. Long, R.M. Stroud, D.R. Rolison, J. Non-Cryst. Solids, 350 (2004) 80-87.

[153] A.E. Fischer, M.P. Saunders, J.C.R. Lytle, D. R., J.W. Long, ECS Transactions, 6 (2008) 159-164.

[154] J.W. Long, D.R. Rolison, Accounts Chem. Res., 40 (2007) 854-862.

[155] A.B. Fuertes, M. Sevilla, T. Valdes-Solis, P. Tartaj, Chem. Mat., 19 (2007) 5418-5423.

[156] R. Liu, S.M. Mahurin, C. Li, R.R. Unocic, J.C. Idrobo, H.J. Gao, S.J. Pennycook, S. Dai, Angew. Chem.-Int. Edit., 50 (2011) 6799-6802.

[157] C. Galeano, R. Guttel, M. Paul, P. Arnal, A.H. Lu, F. Schuth, Chemistry-a European Journal, 17 (2011) 8434-8439.

[158] G.B. Yu, B. Sun, Y. Pei, S.H. Xie, S.R. Yan, M.H. Qiao, K.N. Fan, X.X. Zhang, B.N. Zong, J. Am. Chem. Soc., 132 (2010) 935-937.

[159] X.W. Lou, D. Deng, J.Y. Lee, L.A. Archer, Chem. Mat., 20 (2008) 6562-6566.

[160] X.W. Lou, C.M. Li, L.A. Archer, Adv. Mater., 21 (2009) 2536-2539.

[161] W.M. Zhang, X.L. Wu, J.S. Hu, Y.G. Guo, L.J. Wan, Adv. Funct. Mater., 18 (2008) 3941-3946.

[162] L.H. Kao, Y.C. Chang, P.W. Hung, H.T. Lee, P.H. Chi, Colloid Surf. A-Physicochem. Eng. Asp., 410 (2012) 170-177.

[163] A.B. Fuertes, T. Valdes-Solis, M. Sevilla, P. Tartaj, J. Phys. Chem. C, 112 (2008) 3648-3654.

[164] M. Sevilla, T. Valdes-Solis, P. Tartaj, A.B. Fuertes, J. Colloid Interface Sci., 340 (2009) 230-236.

[165] J.C. Zhang, W.Q. Shen, Z.W. Zhang, D.Y. Pan, M.H. Wu, Mater. Lett., 64 (2010) 817-819.

[166] Y.F. Deng, Q.M. Zhang, S.D. Tang, L.T. Zhang, S.N. Deng, Z.C. Shi, G.H. Chen, Chem. Commun., 47 (2011) 6828-6830.

[167] F. Caruso, Colloid Chemistry Ii, 227 (2003) 145-168.

[168] F. Caruso, Adv. Mater., 13 (2001) 11-22.

[169] A. Dokoutchaev, J.T. James, S.C. Koene, S. Pathak, G.K.S. Prakash, M.E. Thompson, Chem. Mat., 11 (1999) 2389-2399.

[170] L.M. Liz-Marzan, M. Giersig, P. Mulvaney, Langmuir, 12 (1996) 4329-4335.

[171] C. Graf, A. van Blaaderen, Langmuir, 18 (2002) 524-534.

[172] J. Zhou, Y. Zhou, S.L. Ng, H.X. Zhang, W.X. Que, Y.L. Lam, Y.C. Chan, C.H. Kam, Appl. Phys. Lett., 76 (2000) 3337-3339.

[173] S. Phadtare, A. Kumar, V.P. Vinod, C. Dash, D.V. Palaskar, M. Rao, P.G. Shukla, S. Sivaram, M. Sastry, Chem. Mat., 15 (2003) 1944-1949.

[174] C.W. Chen, T. Serizawa, M. Akashi, Chem. Mat., 14 (2002) 2232-2239.

[175] H. Li, Q. Wang, L.H. Shi, L.Q. Chen, X.J. Huang, Chem. Mat., 14 (2002) 103-108.

[176] X.C. Chen, K. Kierzek, K. Wilgosz, J. Machnikowski, J. Gong, J.D. Feng, T. Tang, R.J. Kalenczuk, H.M. Chen, P.K. Chu, E. Mijowska, J. Power Sources, 216 (2012) 475-481.

[177] P. Makowski, R.D. Cakan, M. Antonietti, F. Goettmann, M.M. Titirici, Chem. Commun., (2008) 999-1001.

[178] Q. An, P. Zhang, J.M. Li, W.F. Ma, J. Guo, J. Hu, C.C. Wang, Nanoscale, 4 (2012) 5210-5216.

[179] J.H. Kim, B. Fang, S.B. Yoon, J.S. Yu, Appl. Catal. B-Environ., 88 (2009) 368-375.

[180] Z.B. Lei, J.T. Zhang, X.S. Zhao, Journal of Materials Chemistry, 22 (2012) 153-160.

[181] B. Hu, K. Wang, L.H. Wu, S.H. Yu, M. Antonietti, M.M. Titirici, Adv. Mater., 22 (2010) 813-828.

[182] A. Rabenau, Angew. Chem.-Int. Edit. Engl., 24 (1985) 1026-1040.

[183] J.D. Corbett, Chem. Rev., 85 (1985) 383-397.

[184] H. Schafer, Annu. Rev. Mater. Sci., 15 (1985) 1-41.

[185] M.M. Titirici, M. Antonietti, N. Baccile, Green Chem., 10 (2008) 1204-1212.

[186] N. Baccile, G. Laurent, F. Babonneau, F. Fayon, M.M. Titirici, M. Antonietti, J. Phys. Chem. C, 113 (2009) 9644-9654.

[187] Y. Shin, L.Q. Wang, I.T. Bae, B.W. Arey, G.J. Exarhos, J. Phys. Chem. C, 112 (2008) 14236-14240.

[188] C. Yao, Y. Shin, L.Q. Wang, C.F. Windisch, W.D. Samuels, B.W. Arey, C. Wang, W.M. Risen, G.J. Exarhos, J. Phys. Chem. C, 111 (2007) 15141-15145.

[189] M. Sevilla, G. Lota, A.B. Fuertes, J. Power Sources, 171 (2007) 546-551.

[190] M. Sevilla, A.B. Fuertes, Carbon, 47 (2009) 2281-2289.

[191] M.M. Titirici, M. Antonietti, Chem. Soc. Rev., 39 (2010) 103-116.

[192] Q. Wang, H. Li, L.Q. Chen, X.J. Huang, Carbon, 39 (2001) 2211-2214.

[193] S.H. Yu, X.J. Cui, L.L. Li, K. Li, B. Yu, M. Antonietti, H. Colfen, Adv. Mater., 16 (2004) 1636-1640.

[194] M. Sevilla, A.B. Fuertes, Chemistry-a European Journal, 15 (2009) 4195-4203.

[195] B.M. Kabyemela, T. Adschiri, R.M. Malaluan, K. Arai, Ind. Eng. Chem. Res., 38 (1999) 2888-2895.

[196] G.C.A. Luijkx, F. Vanrantwijk, H. Vanbekkum, M.J. Antal, Carbohydr. Res., 272 (1995) 191-202.

[197] T.M. Aida, Y. Sato, M. Watanabe, K. Tajima, T. Nonaka, H. Hattori, K. Arai, J. Supercrit. Fluids, 40 (2007) 381-388.

[198] F.S. Asghari, H. Yoshida, Ind. Eng. Chem. Res., 45 (2006) 2163-2173.

[199] V.K.L. Mer, Industrial & Engineering Chemistry, 44 (1952) 1270-1277.

[200] Y.N. Xia, B. Gates, Y.D. Yin, Y. Lu, Adv. Mater., 12 (2000) 693-713.

[201] M.M. Titirici, A. Thomas, M. Antonietti, Journal of Materials Chemistry, 17 (2007) 3412-3418.

[202] J.K. Jaiswal, H. Mattoussi, J.M. Mauro, S.M. Simon, Nat. Biotechnol., 21 (2003) 47-51.

[203] G.F. Jie, H.P. Huang, X.L. Sun, J.J. Zhu, Biosens. Bioelectron., 23 (2008) 1896-1899.

[204] A.P. Alivisatos, W.W. Gu, C. Larabell, Quantum dots as cellular probes, in: Annual Review of Biomedical Engineering, Annual Reviews, Palo Alto, 2005, pp. 55-76.

[205] J.H. Gao, B. Xu, Nano Today, 4 (2009) 37-51.

[206] X. Wang, L. Cao, S.T. Yang, F.S. Lu, M.J. Meziani, L.L. Tian, K.W. Sun, M.A. Bloodgood, Y.P. Sun, Angew. Chem.-Int. Edit., 49 (2010) 5310-5314.

[207] H.T. Li, X.D. He, Z.H. Kang, H. Huang, Y. Liu, J.L. Liu, S.Y. Lian, C.H.A. Tsang, X.B. Yang, S.T. Lee, Angew. Chem.-Int. Edit., 49 (2010) 4430-4434.

[208] R. Demir-Cakan, N. Baccile, M. Antonietti, M.M. Titirici, Chem. Mat., 21 (2009) 484-490.

[209] R.E. Bailey, S.M. Nie, J. Am. Chem. Soc., 125 (2003) 7100-7106.

[210] J.J. Max, C. Chapados, J. Phys. Chem. A, 111 (2007) 2679-2689.

[211] S. Chandra, P. Das, S. Bag, D. Laha, P. Pramanik, Nanoscale, 3 (2011) 1533-1540.

[212] X.H. Wang, K.G. Qu, B.L. Xu, J.S. Ren, X.G. Qu, Journal of Materials Chemistry, 21 (2011) 2445-2450.

[213] Y.Q. Dong, N.N. Zhou, X.M. Lin, J.P. Lin, Y.W. Chi, G.N. Chen, Chem. Mat., 22 (2010) 5895-5899.

[214] S. Liu, J. Tian, L. Wang, Y. Luo, J. Zhai, X. Sun, Journal of Materials Chemistry, 21 (2011) 11726-11729.

[215] Z. Ma, H. Ming, H. Huang, Y. Liu, Z. Kang, New Journal of Chemistry, 36 (2012) 861-864.

[216] Y.-Q. Zhang, D.-K. Ma, Y. Zhuang, X. Zhang, W. Chen, L.-L. Hong, Q.-X. Yan, K. Yu, S.-M. Huang, Journal of Materials Chemistry, 22 (2012) 16714-16718.

[217] Z.L. Wu, P. Zhang, M.X. Gao, C.F. Liu, W. Wang, F. Leng, C.Z. Huang, Journal of Materials Chemistry B, 1 (2013) 2868-2873.

[218] Y.R. Chang, H.Y. Lee, K. Chen, C.C. Chang, D.S. Tsai, C.C. Fu, T.S. Lim, Y.K. Tzeng, C.Y. Fang, C.C. Han, H.C. Chang, W. Fann, Nat. Nanotechnol., 3 (2008) 284-288.

[219] C.C. Fu, H.Y. Lee, K. Chen, T.S. Lim, H.Y. Wu, P.K. Lin, P.K. Wei, P.H. Tsao, H.C. Chang, W. Fann, Proceedings of the National Academy of Sciences of the United States of America, 104 (2007) 727-732.

[220] S.J. Yu, M.W. Kang, H.C. Chang, K.M. Chen, Y.C. Yu, J. Am. Chem. Soc., 127 (2005) 17604-17605.

[221] S. Munier, I. Messai, T. Delair, B. Verrier, Y. Ataman-Onal, Colloid Surf. B-Biointerfaces, 43 (2005) 163-173.

[222] S. Roseman, Journal of Biological Chemistry, 276 (2001) 41527-41542.

[223] W. Gao, L.B. Alemany, L.J. Ci, P.M. Ajayan, Nat. Chem., 1 (2009) 403-408.

[224] M. Perraki, A. Proyer, E. Mposkos, R. Kaindl, G. Hoinkes, Earth Planet. Sci. Lett., 241 (2006) 672-685.

[225] J. Stiegler, A. Bergmaier, J. Michler, S. Laufer, G. Dollinger, E. Blank, Thin Solid Films, 352 (1999) 29-40.

[226] K. Iakoubovskii, G.J. Adriaenssens, Phys. Rev. B, 61 (2000) 10174-10182.

[227] M.K. Fung, W.C. Chan, Z.Q. Gao, I. Bello, C.S. Lee, S.T. Lee, Diam. Relat. Mat., 8 (1999) 472-476.

[228] A. Chowdhury, D.C. Cameron, M.S.J. Hashmi, Thin Solid Films, 332 (1998) 62-68.

[229] A. Pawlak, A. Mucha, Thermochim. Acta, 396 (2003) 153-166.

[230] X.F. Li, J. Zhang, L.H. Shen, Y.M. Ma, W.W. Lei, Q.L. Cui, G.T. Zou, Appl. Phys. A-Mater. Sci. Process., 94 (2009) 387-392.

[231] A. Barth, Prog. Biophys. Mol. Biol., 74 (2000) 141-173.

[232] C.D. Wanger, W.M. Riggs, L.E. Davis, J.F. Moulder, G.E. Muilenberg, Handbook of X-ray Photoelectron Spectroscopy, Perkin-Elmer Corp., Physical Electronics Division, Eden Prairie, Minnesota, USA, 1979.

[233] M. Jun, Y. Shao, C.T. Ho, U. Koetter, S. Lech, J. Agric. Food Chem., 51 (2003) 6340-6346.

[234] J. Li, X. Li, Z.H. Zhou, X.P. Ni, K.W. Leong, Macromolecules, 34 (2001) 7236-7237.

[235] J. Li, X.P. Ni, K. Leong, Angew. Chem.-Int. Edit., 42 (2003) 69-72.

[236] P. Ulanski, W. Pawlowska, S. Kadlubowski, A. Henke, R. Gottlieb, K.F. Arndt, L. Bromberg, T.A. Hatton, J.M. Rosiak, Polym. Adv. Technol., 17 (2006) 804-813.

[237] Y.L. Su, H.Z. Liu, J. Wang, J.Y. Chen, Langmuir, 18 (2002) 865-871.

[238] A. Harada, J. Li, M. Kamachi, Macromolecules, 26 (1993) 5698-5703.

[239] R.K. McMullan, W. Saenger, J. Fayos, D. Mootz, Carbohydr. Res., 31 (1973) 37-46.

[240] R.K. Prudhomme, G.W. Wu, D.K. Schneider, Langmuir, 12 (1996) 4651-4659.

[241] X.Y. Xiong, K.C. Tam, L.H. Gan, Macromolecules, 36 (2003) 9979-9985.

[242] J. Hu, H. Li, X.J. Huang, Solid State Ion., 176 (2005) 1151-1159.

[243] W.B. Xing, J.S. Xue, T. Zheng, A. Gibaud, J.R. Dahn, J. Electrochem. Soc., 143 (1996) 3482-3491.

[244] G.P. Wang, L. Zhang, J.J. Zhang, Chem. Soc. Rev., 41 (2012) 797-828.

[245] J.R. Miller, P. Simon, Science, 321 (2008) 651-652.

[246] P. Simon, Y. Gogotsi, Nat. Mater., 7 (2008) 845-854.

[247] B.E. Conway, J. Electrochem. Soc., 138 (1991) 1539-1548.

[248] X.Y. Lang, A. Hirata, T. Fujita, M.W. Chen, Nat. Nanotechnol., 6 (2011) 232-236.

[249] C.N. Chervin, J.W. Long, N.L. Brandell, J.M. Wallace, N.W. Kucko, D.R. Rolison, J. Power Sources, 207 (2012) 191-198.

[250] W.D. Zhang, J. Chen, Pure Appl. Chem., 81 (2009) 2317-2325.

[251] A.L.M. Reddy, M.M. Shaijumon, S.R. Gowda, P.M. Ajayan, J. Phys. Chem. C, 114 (2010) 658-663.

[252] Y.W. Zhu, S. Murali, M.D. Stoller, K.J. Ganesh, W.W. Cai, P.J. Ferreira, A. Pirkle, R.M. Wallace, K.A. Cychosz, M. Thommes, D. Su, E.A. Stach, R.S. Ruoff, Science, 332 (2011) 1537-1541.

[253] L.L. Zhang, X.S. Zhao, Chem. Soc. Rev., 38 (2009) 2520-2531.

[254] N.L. Wu, S.L. Kuo, M.H. Lee, J. Power Sources, 104 (2002) 62-65.

[255] J.W. Long, M.B. Sassin, A.E. Fischer, D.R. Rolison, A.N. Mansour, V.S. Johnson, P.E. Stallworth, S.G. Greenbaum, J. Phys. Chem. C, 113 (2009) 17595-17598.

[256] S.W. Lee, J. Kim, S. Chen, P.T. Hammond, Y. Shao-Horn, ACS Nano, 4 (2010) 3889-3896.

[257] Z.S. Wu, W.C. Ren, D.W. Wang, F. Li, B.L. Liu, H.M. Cheng, ACS Nano, 4 (2010) 5835-5842.

[258] S. Devaraj, N. Munichandraiah, J. Phys. Chem. C, 112 (2008) 4406-4417.

[259] L. Mao, K. Zhang, H.S.O. Chan, J.S. Wu, Journal of Materials Chemistry, 22 (2012) 1845-1851.

[260] S. Ching, D.J. Petrovay, M.L. Jorgensen, S.L. Suib, Inorg. Chem., 36 (1997) 883-890.

[261] J.G. Wang, Y. Yang, Z.H. Huang, F.Y. Kang, J. Power Sources, 204 (2012) 236-243.

[262] W.F. Wei, X.W. Cui, W.X. Chen, D.G. Ivey, Chem. Soc. Rev., 40 (2011) 1697-1721.

[263] Q. Li, J.M. Anderson, Y.Q. Chen, L. Zhai, Electrochim. Acta, 59 (2012) 548-557.

[264] G.H. Yu, L.B. Hu, M. Vosgueritchian, H.L. Wang, X. Xie, J.R. McDonough, X. Cui, Y. Cui, Z.N. Bao, Nano Lett., 11 (2011) 2905-2911.

[265] E. Raymundo-Pinero, F. Leroux, F. Beguin, Adv. Mater., 18 (2006) 1877-1882.

[266] D.N. Futaba, K. Hata, T. Yamada, T. Hiraoka, Y. Hayamizu, Y. Kakudate, O. Tanaike, H. Hatori, M. Yumura, S. Iijima, Nat. Mater., 5 (2006) 987-994.

[267] K.X. Sheng, Y.Q. Sun, C. Li, W.J. Yuan, G.Q. Shi, Sci Rep, 2 (2012).

[268] L. Zhang, F. Zhang, X. Yang, G.K. Long, Y.P. Wu, T.F. Zhang, K. Leng, Y. Huang, Y.F. Ma, A. Yu, Y.S. Chen, Sci Rep, 3 (2013).

[269] H.Y. Jung, M.B. Karimi, M.G. Hahm, P.M. Ajayan, Y.J. Jung, Sci Rep, 2 (2012).

[270] Q.Y. Li, Z.S. Li, L. Lin, X.Y. Wang, Y.F. Wang, C.H. Zhang, H.Q. Wang, Chem. Eng. J., 156 (2010) 500-504.

[271] A. Ghosh, Y.H. Lee, ChemSusChem, 5 (2012) 480-499.

[272] C. Liu, F. Li, L.P. Ma, H.M. Cheng, Adv. Mater., 22 (2010) E28-E62.

[273] B.E. Conway, V. Birss, J. Wojtowicz, J. Power Sources, 66 (1997) 1-14.

[274] I.H. Kim, K.B. Kim, J. Electrochem. Soc., 153 (2006) A383-A389.

[275] Z.L. Wang, R. Guo, L.X. Ding, Y.X. Tong, G.R. Li, Sci Rep, 3 (2013).

[276] H.Y. Lee, J.B. Goodenough, J. Solid State Chem., 148 (1999) 81-84.

[277] S.W. Hwang, S.H. Hyun, J. Power Sources, 172 (2007) 451-459.

[278] X. Zhao, C. Johnston, P.S. Grant, Journal of Materials Chemistry, 19 (2009) 8755-8760.

[279] J. Chen, K.L. Huang, S.Q. Liu, Electrochim. Acta, 55 (2009) 1-5.

[280] K.C. Liu, M.A. Anderson, J. Electrochem. Soc., 143 (1996) 124-130.

[281] J.W. Lang, L.B. Kong, W.J. Wu, M. Liu, Y.C. Luo, L. Kang, J. Solid State Electrochem., 13 (2009) 333-340.

[282] T.Y. Wei, C.H. Chen, K.H. Chang, S.Y. Lu, C.C. Hu, Chem. Mat., 21 (2009) 3228-3233.

[283] L. Cao, F. Xu, Y.Y. Liang, H.L. Li, Adv. Mater., 16 (2004) 1853-1857.

[284] C. Guan, J.P. Liu, C.W. Cheng, H.X. Li, X.L. Li, W.W. Zhou, H. Zhang, H.J. Fan, Energy Environ. Sci., 4 (2011) 4496-4499.

[285] P. Thounthong, V. Chunkag, P. Sethakul, B. Davat, M. Hinaje, Vehicular Technology, IEEE Transactions on, 58 (2009) 3892-3904.

[286] H. Pan, J.Y. Li, Y.P. Feng, Nanoscale Res. Lett., 5 (2010) 654-668.

[287] A.S. Arico, P. Bruce, B. Scrosati, J.M. Tarascon, W. Van Schalkwijk, Nat. Mater., 4 (2005) 366-377.

[288] H. Jiang, J. Ma, C.Z. Li, Adv. Mater., 24 (2012) 4197-4202.

[289] H.W. Wang, Z.A. Hu, Y.Q. Chang, Y.L. Chen, Z.Y. Zhang, Y.Y. Yang, H.Y. Wu, Mater. Chem. Phys., 130 (2011) 672-679.

[290] M.Z. Dai, L.Y. Song, J.T. LaBelle, B.D. Vogt, Chem. Mat., 23 (2011) 2869-2878.

[291] M. Sevilla, C.S. Martinez-de Lecea, T. Valdes-Solis, E. Morallon, A.B. Fuertes, Phys. Chem. Chem. Phys., 10 (2008) 1433-1442.

[292] Z.L. Wang, X.B. Zhang, X.J. Liu, M.F. Lv, K.Y. Yang, J.A. Meng, Carbon, 49 (2011) 161-169.

[293] R.M. Al-Tuwirqi, A.A. Al-Ghamdi, F. Al-Hazmi, F. Alnowaiser, N.A. Aal, F. El-Tantawy, Superlattices Microstruct., 50 (2011) 437-448.

[294] A.C. Ferrari, J.C. Meyer, V. Scardaci, C. Casiraghi, M. Lazzeri, F. Mauri, S. Piscanec, D. Jiang, K.S. Novoselov, S. Roth, A.K. Geim, Phys. Rev. Lett., 97 (2006).

[295] A.C. Ferrari, J. Robertson, Phys. Rev. B, 64 (2001).

[296] H.C. Choi, Y.M. Jung, I. Noda, S.B. Kim, J. Phys. Chem. B, 107 (2003) 5806-5811.

[297] N.A. Katcho, E. Urones-Garrote, D. Avila-Brande, A. Gomez-Herrero, S. Urbonaite, S. Csillag, E. Lomba, F. Agullo-Rueda, A.R. Landa-Canovas, L.C. Otero-Diaz, Chem. Mat., 19 (2007) 2304-2309.

[298] H. Pan, C.K. Poh, Y.P. Feng, J.Y. Lin, Chem. Mat., 19 (2007) 6120-6125.

[299] K.S. Xia, Q.M. Gao, J.H. Jiang, J. Hu, Carbon, 46 (2008) 1718-1726.

Appendices

1. **Z. Yang**, M. Wang, A. M. Yong, S. Y. Wong, X. Zhang, H. Tan, A. Y. Chang, X. Li, J. Wang, "Intrinsically fluorescent carbon dots with tunable emission derived from hydrothermal treatment of glucose in the presence of monopotassium phosphate", *Chem. Commun.* **2011**, *47*, 11615-11617.
2. **Z. Yang**, X. Li, J. Wang, "Intrinsically fluorescent nitrogen-containing carbon nanoparticles synthesized by a hydrothermal process", *Carbon* **2011**, *49*, 5207-5212.
3. **Z. Yang**, Y. Zhang, J. Kong, S. Y. Wong, X. Li, J. Wang, "Hollow carbon nanoparticles of tunable size and wall thickness by hydrothermal treatment of α-cyclodextrin templated by F127 block copolymers", *Chem. Mater.* **2013**, *25*, 704-710.
4. **Z. Yang**, C. Tang, H. Gong, X. Li, J. Wang, "Hollow spheres of nanocarbon and their manganese dioxide hybrids derived from soft template for supercapacitor application", *J. Power Sources* **2013**, *240*, 713-720.
5. **Z. Yang**, C. Tang, Y. Zhang, H. Gong, X. Li, J. Wang, "Cobalt monoxide-doped porous graphitic carbon microspheres for supercapacitor application", *Sci. Rep.* **2013**, *3*, 2925.